

Rapid Disaster Response

Building Damage Detection Using Google Earth Engine

J. C. van Heyningen

Using Sentinel-1 GRD imagery in the Google Earth Engine to detect Building Damage in Rapid Disaster Response Situations



Rapid Disaster Response

Building Damage Detection Using the
Google Earth Engine

by

J. C. van Heyningen

to obtain the degree of Master of Science
at the Delft University of Technology,
to be defended publicly on Friday November 16, 2018 at 9:30 AM.

Student number: 4421051
Project duration: February 1, 2017 – November 16, 2018
Thesis committee: Prof. Dr. Ir. R. F. Hanssen, TU Delft, supervisor
Dr. Ir. F. Lopez Dekker, TU Delft
Dr. Ir. K. C. Terwel, TU Delft

An electronic version of this thesis is available at <http://repository.tudelft.nl/>.

Contents

Preface	v
Abstract	vii
Nomenclature	ix
1 Introduction	1
1.1 Research Motivation	2
1.2 Aim of the Research	3
1.3 Methodology	4
1.4 Thesis Lay-out	6
2 Background Information	9
2.1 Humanitarian Crises related to Building Damage	9
2.2 Current Search and Rescue Practices	11
2.3 Literature Review: Remote Sensing in Rapid Disaster Response.	14
2.3.1 UAVs	14
2.3.2 Airborne	16
2.3.3 Spaceborne	16
2.4 The Sentinel-1 Mission	29
3 Methodology	31
3.1 Google Earth Engine	31
3.2 Sentinel-1 Data	33
3.2.1 ESA Processing.	33
3.2.2 EE processing	34
3.3 Optical Data	37
3.4 Damage Detection System	38
3.4.1 Data Selection	38
3.4.2 Change Detection Algorithm.	45
3.5 Application of Damage Detection System into Practice	52
4 Results	55
4.1 Earthquake: Amatrice, Italy (2016)	57
4.2 Earthquake: Mexico City, Mexico (2017).	62
4.3 Military Strikes: East-Ghouta, Syria (2018)	66
5 Discussion and Conclusions	71
5.1 Discussion	71
5.2 Conclusion	73
5.3 Recommendations	74
5.4 Outlook	74
Bibliography	75
A Damage Detection Maps	81
B User Manual	87
C JavaScript Code	91
C.1 Damage_General	91
C.2 Damage_Function	91

Preface

This master thesis project has been carried out at the department of Geoscience and Remote Sensing of the faculty of Civil Engineering and Geosciences, Delft University of Technology. The goal of this project was to use the Google Earth Engine for rapidly locating damaged buildings in disaster response situations for areas suffering from humanitarian disasters related to building damage.

This subject is perfectly in line with the course of my academic period. I began my track to bachelor of science in the field of Earth sciences at the University of Utrecht with the special interest for natural disasters and finding solutions to reduce the impact they have on societies around the world. During my bachelors I learned about the various processes and physics behind these disasters, which fueled my interest even more. However, the practical approach was still missing. This is where remote sensing came into play and through Roger Haagmans, father of Gaston Haagmans with whom I studied Earth sciences, I came to know of the master's track Geoscience and Remote Sensing at Delft University of Technology. After doing my bachelor's thesis in this field of study by analyzing gravimetry data for monitoring surface deformation due to geothermal power plants and subsurface magma fluctuations in Iceland, I was convinced that the master Geoscience and Remote Sensing would suit me well. This feeling was confirmed in my first year at Delft when I followed the course Geodesy and Natural Hazards, given by Prof. Dr. Ir. Ramon Hanssen. Because of this course, I contacted Prof. Hanssen when searching for an internship, preferably abroad. He came up with a few interesting options, but the perfect opportunity came along when I mentioned a paper on damage detection using radar satellite data which my father forwarded me the night prior to the meeting with Prof. Hanssen. Surprisingly, Prof. Hanssen knew the author of the paper, Dr. Yun, from his time at Stanford.

After months of preparation I moved to Pasadena, California, U.S., for a six month internship at the Jet Propulsion Laboratory to work at the Advanced Rapid Imaging and Analysis (ARIA) group. This group performs research in rapidly processing remote sensing data for rapid disaster response purposes. I enjoyed this time very much and still value this period for the impact it had on my personal development. Besides the continuous experiences of living abroad, especially in California, and working at a NASA facility, the experiences regarding academic research in the field of applying remote sensing data to support rescue operations made me enjoy my time there the most. That is why I also wanted to continue my master's thesis research in this field. Moments of working late and in weekends together with moments of frustration did not way up to the joyful moments when you get the algorithm to do what you intended it to do. But the most joyful moment occurred when I pitched the approach to the Urban Search And Rescue team of the Netherlands and noticed that a tool like the one presented here had their interest. During the pitch I was allowed to perform a live demonstration of the approach for their mission to Saint Martin after hurricane Irma in 2018. At this time I had not looked at this event and naturally I was glad when the algorithm performed well in general, but the relief really came when the pixels indicated as changed over the airport were exactly matched by the team as a collapsed part of the airport terminal and a damaged beach club, meaning that the damage detection algorithm generated reliable results. All of the above mentioned experiences have added to the positive view I have on my academic period in general and my master's thesis in particular.

First, I would like to thank my family and girlfriend for their continuous support and help throughout my entire academical period. Furthermore a big thanks to my friends in Utrecht, Nootdorp and Delft for the great experienced together of which I hope (and think) many more will come. And last but not least, I would like to thank my graduation comity for their advice, time and attention throughout the development of my thesis up until the very final version presented here.

*J. C. van Heyningen
Delft, January 2013*

The image on the cover shows the severity of building damage in Amatrice after the M6.2 2016 Central-Italy earthquake. It has been obtained from <https://disasters.nasa.gov/amatrice-italy-earthquake-2016>, the original photographer is unknown.

Abstract

Humanitarian crises related to building and infrastructure damage, i.e. natural hazards and collateral damage during warfare, result in many hundreds of thousands of casualties on a yearly base. Earthquakes, for example, are responsible for taking around 50.000 lives on a yearly base due to falling debris and collapsing buildings, making them one of the most deadly natural disasters known to mankind. These casualties are caused by both direct effects (falling debris) as well as indirect effects (being trapped by debris without access to air/water/food). In the first hours after an earthquake hit an area, a clear overview of the situation is hard to obtain due to inaccessible roads and damaged communication systems, which in its turn hampers setting up rapid disaster response operations. In order to assist the search and rescue teams in wide-area situation awareness, remote sensing techniques can be used to acquire and create damage detection maps which could be used to prioritize their tasks and help save more lives.

Spaceborne Synthetic Aperture Radar (SAR) is one of the most promising techniques in rapid disaster response as it is an active sensor which remains unaffected by the weather, smoke, cloud cover and/or daylight. The Sentinel-1 mission is a relatively new SAR mission that acquires data over the entire Earth's surface every 3 days in any viewing geometry. More importantly, this mission has an open-data policy and hence provides the opportunity to easily perform multi-temporal data analysis instead of the bi- and tri-temporal change detection approaches proposed in previous studies. The development of a fully automatic change detection algorithm has been done in the Google Earth Engine: an online, open-source processing tool that allows users to run algorithms on geo-referenced Earth observation imagery stored on Google's infrastructure, with one of these datasets being the global Sentinel-1 GRD dataset. The time reduction that results from bringing the algorithm to the data instead of vice versa as well as the possibility to easily combine various geo-referenced datasets both benefited the rapid disaster response operations.

The processing of the data is performed completely automatically based on the date and location of the disaster as input, making it easy to use for non-remote sensing specialists. Using these two parameters, the Sentinel-1 images overlapping the area of interest are selected after which a change detection algorithm is applied to the timeseries. The resulting damage detection maps has been validated in terms of operability and accuracy for wide-area situation awareness in search and rescue operations for three case studies: the 2016 M6.2 Central Italy earthquake, the 2017 M7.1 Central Mexico earthquake and the 2018 Syria military strikes. Overall, the algorithm performs well in terms of damage detection, with a low amount of false positives and an even lower amount of false negatives, for both damage due to natural hazards and intentional or collateral damage during warfare. The algorithm experienced difficulties when identifying individual collapsed buildings in a dense urban environment as around 50% of the collapsed buildings were detected as such. However, the accuracy of the damage detection is much better when looking at clusters of damaged buildings in urban areas or at individual buildings, which are equal to or larger than the size of a SAR resolution cell, in less dense urban environments.

The complete approach and final damage detection maps have been presented to the Urban Search And Rescue team of The Netherlands, whom are the potential end-users of these maps. They saw great potential in this approach in general to help prioritize their search and rescue operations, with the only bottleneck being the data latency. We showed that once a new image has been acquired after the disaster, the total data latency by ESA and the GEE is at most 72h. This is also the maximal time the USAR team has in order to move from their home base to any country in the world in case of a disaster. The data latency time frame is a maximum, so actual averages are lower and the final damage detection map will be completed and ready to use once needed by the USAR team. This illustrates that the approach proposed in this research can be used on an operational base to assist in rapid disaster response situations.

Nomenclature

Below you will find a list of acronyms used in this report:

ALOS	<i>Advanced Land Observing Satellite</i>
AOI	<i>Area Of Interest</i>
API	<i>Application Programming Interface</i>
ARIA	<i>Advanced Rapid Imaging and Analysis</i>
ASTER	<i>Advanced Spaceborne Thermal Emission and Reflection Radiometer</i>
ASR	<i>Assessment, Search and Rescue level</i>
CEST	<i>Central European Summer Time</i>
CDT	<i>Central Daylight Time</i>
CFMASK	<i>C Function of Mask algorithm</i>
CHIRPS	<i>Climate Hazards Group InfraRed Precipitation with Station Data</i>
COSMO-SkyMed	<i>Constellation of small Satellites for the Mediterranean basin Observation</i>
COP	<i>Common Operational Picture</i>
CPU	<i>Central Processing Unit</i>
DEM	<i>Digital Elevation Model</i>
DPM	<i>Damage Proxy Map</i>
DN	<i>Digital Numbers</i>
EC	<i>European Commission</i>
EE	<i>Earth Engine</i>
EEST	<i>Eastern European Summer Time</i>
EMS-98	<i>European Macroseismic Scale</i>
ENL	<i>Equivalent Number of Looks</i>
ENVISAT	<i>Environmental Satellite</i>
EROS	<i>Earth Resources Observation and Science</i>
ERS	<i>European Remote Sensing Satellite</i>
ESA	<i>European Space Agency</i>
EUCPM	<i>European Union Civil Protection Mechanism</i>
EW	<i>Extra Wide Swath</i>
GCPs	<i>Ground Control Points</i>
GDACS	<i>Global Disaster Alerting Coordination System</i>
GEE	<i>Google Earth Engine</i>
GIS	<i>Geographic Information System</i>
GMES-EMS	<i>Global Monitoring for Environment and Security - Emergency Management Service</i>
GRD	<i>Ground Range Detected</i>
HH	<i>Horizontally Transmitted, Horizontally received</i>
HV	<i>Horizontally Transmitted, Vertically received</i>
IDE	<i>Integrated Development Environment</i>
InSAR	<i>Interferometric Synthetic Aperture Radar</i>

INSARAG	<i>International Search and Rescue Advisory Group</i>
IW	<i>Interferometric Wide Swath</i>
JAXA	<i>Japanese Aerospace Exploration Agency</i>
JPL	<i>Jet Propulsion Laboratory</i>
KML	<i>Keyhole Markup Language</i>
LaSRC	<i>Landsat 8 Surface Reflectance Code</i>
LEMA	<i>Local Emergency Management Authority</i>
LIDAR	<i>Llght Detection And Ranging of Laser Imaging Detection And Ranging</i>
LUTs	<i>Look-Up Tables</i>
MODIS	<i>Moderate-Resolution Imaging Spectroradiometer</i>
NAIP	<i>National Agriculture Imagery Program</i>
NASA	<i>National Aeronautics and Space Administration</i>
NDVI	<i>Normalized Difference Vegetation Index</i>
NESZ	<i>Noise Equivalent Sigma Zero</i>
NIR	<i>Near-Infrared</i>
OCHA	<i>United Nations Office for the Coordination of Humanitarian Affairs</i>
OLI	<i>Operational Land Imager</i>
OSOCC	<i>On-Site Operational Coordination Centre</i>
PALSAR	<i>Phased Array type L-band Synthetic Aperture Radar</i>
QA	<i>Quality Assessment</i>
RADAR	<i>Radio Detecting And Ranging</i>
SA	<i>Sentinel Asia</i>
SAA	<i>Syrian Arab Army</i>
SAR	<i>Synthetic Aperture Radar</i>
SciHub	<i>Scientific Data Hub</i>
SLC	<i>Single Look Complex</i>
SM	<i>Strip Map Mode</i>
SNAP	<i>Sentinel Application Platform</i>
SR	<i>Surface Reflectance</i>
SRTM	<i>Shuttle Radar Topography Mission</i>
SWIR	<i>Short Wave Infrared</i>
TIR	<i>Thermal Infrared</i>
TIRS	<i>Thermal Infrared Sensor</i>
TOA	<i>Top of Atmosphere</i>
TOPSAR	<i>Terrain Observation with Progressive Scans SAR</i>
UAV	<i>Unmanned Aerial Vehicle</i>
UNDAC	<i>United Nations Disaster Assessment and Coordination</i>
UN-SPIDER	<i>United Nations Platform for Space-based Information for Disaster Management and Emergency Response</i>
USAR	<i>Urban Search And Rescue</i>
USGS	<i>United States Geological Survey</i>
UTC	<i>Coordinated Universal Time</i>
VNIR	<i>Visible and Near-Infrared</i>
VH	<i>Vertically Transmitted, Horizontally received</i>
VV	<i>Vertically Transmitted, Vertically received</i>
WGS84	<i>World Geodetic System 1984</i>
WV	<i>Wave Mode</i>

Below you will find a list of symbols used in this report:

I	<i>Backscattering Intensity</i>
$u_{\mathbf{IP}}$	<i>In-phase Channel Signal</i>
$u_{\mathbf{Q}}$	<i>Quadrature Channel Signal</i>
ϕ	<i>Phase</i>
P_r	<i>Receiving Power</i>
P_t	<i>Transmitting Power</i>
G_a	<i>Antenna Gain</i>
λ	<i>Wavelength</i>
$\sigma_{\mathbf{rcs}}$	<i>Radar Cross Section</i>
R	<i>Range</i>
γ	<i>Coherence</i>
z	<i>Complex Signal</i>
σ	<i>Standard Deviation</i>
ρ	<i>Coherence Change Index</i>
r	<i>Correlation Coefficient</i>
Z_{Rp}	<i>Discriminant Score</i>
d	<i>Intensity Difference</i>
V	<i>Radiometric Calibrated Value</i>
γ_0	<i>Gamma nought</i>
β_0	<i>Beta nought</i>
σ_0	<i>Sigma nought</i>
A	<i>Calibration Scaling Factor</i>
n	<i>Calibrated Noise</i>
η	<i>Noise Scaling Factor</i>
D_A	<i>Normalized Amplitude Dispersion</i>
μ	<i>Average</i>
F	<i>Sigma Nought Ratio Factor</i>
y	<i>Complex Circular Gaussian Variable</i>
a	<i>Amplitude</i>
$\Delta\sigma_0$	<i>Change in Sigma nought</i>
C	$\Delta\sigma_0$ <i>timeseries</i>
O	σ_0 <i>timeseries</i>
$S_{\Delta\sigma_0}$	$\Delta\sigma_0$ <i>Ratio</i>



Introduction

Humanitarian crises related to building damage, caused by either natural hazards or collateral damage during warfare, demand many lives every year. Among natural hazards, this large amount of casualties is illustrated by the fact that earthquakes are one of the deadliest natural disasters on Earth known to mankind (Bartels and VanRooyen [2012], Roser and Ritchie [2018]). Natural hazards and collateral damage cause buildings and other large structures to collapse, which in turn results in direct casualties from falling rubble and indirect casualties from trapping humans in the piles of rubble without access to food, water or air. On average, a healthy person is able to survive for about 72 hours in piles of rubble without any resources (Castro [2011]). Naturally, factors such as access to water and food or the type of building materials used influence the estimation of this survival rate. Therefore, the first hours to days after a disaster occurred is the most crucial time frame for rescue teams in order to find and rescue trapped individuals. However, the bottleneck for efficient rescue operations during this period is the lack of a clear overview of the situation due to the severity of the event, inaccessible roads and damaged communication systems (Statheropoulos et al. [2015], American Red Cross [2015]).

An example of the effect of insufficient information regarding a disaster and its consequences, on search and rescue operations was clearly illustrated by the rescue operation of the Urban Search And Rescue (USAR) team of the Netherlands during the aftermath of the Kathmandu earthquake in Nepal, 2015. The USAR team is a crew consisting of policemen, firemen and nurses that have been trained to assist in search and rescue operations in The Netherlands and abroad. The USAR team is able to be on location in The Netherlands within six hours and able to travel anywhere in the world within 24 hours in order to support rescue operations. Their help was requested by the Nepalese government regarding the humanitarian crisis due to the M7.8 2015 Nepal earthquake. Upon arrival in Nepal there was little to no information available regarding where help was needed. The rescue team decided to go to Kathmandu, the capital of Nepal, based on the high number of inhabitants and the closeness to the epicentre of the earthquake. However, after setting up the base camp and exploring the area of Kathmandu manually they concluded that their help was not needed here and could be used elsewhere. Next, they travelled to the north of Nepal in order to assist in rescue operations there as the result of landslides. The time period from arriving in Nepal to arriving at a location where they were able to actually save lives took three days in total. If they would have known the locations of the areas with severest destruction beforehand, they would most likely have been able to plan their rescue operation more efficiently and hence been able to save more lives (USAR [2015]). This clearly illustrates the significance of proper preliminary information on damage maps for rescue workers.

1.1. Research Motivation

In order to manage civil protection interventions, it is of great importance that a clear understanding of the situation is obtained as quickly as possible after a disaster occurred. With this information, rescue teams will be able to plan their rescue mission more efficiently which in its turn results in more time for saving victims resulting from the disaster. As ground-based observations are generally too time consuming due to inaccessible roads and damaged communication systems, remote sensing techniques are the most favoured solution to this challenge (Stramondo et al. [2006]). The challenge in using remote sensing data for rapid disaster response is to quickly create reliable damage detection maps of the area, which are usable for rescue teams, based on the first post-disaster acquisition available. Besides the maps are preferably generated completely automatic as this gives the most consistent results and does not require manual interaction.

Drone-, air- or space-based remote sensing data could be used to create an overview of the area that has been struck and indicate locations of possible building damage. Available instruments that are suitable for this kind of application are optical, radar or LIDAR systems. Each of these sources, as well as the platform on which the instruments are mounted, has its own pros and cons regarding the application of the data on rapid disaster response situations. For example, drone-based and air-based remote sensing systems can be deployed right after the disaster whereas with space-based systems one has to wait for the next revisit of the satellite, which may take hours to days. Naturally, drone- and air-based systems can only be deployed when the material is available. On the other hand, space-based systems observe a larger area on a consistent base while for drone- and air-based systems this observable area is smaller and there is not always pre-disaster data available, especially not in undeveloped countries. However, as any kind of preliminary information on the disaster struck area is useful it really depends on the situation which type of data can be used.

One of the most promising forms of spaceborne remote sensing data in rapid disaster response situations is Synthetic Aperture Radar (SAR) data as it is an active satellite-based sensor, operating unaffectedly by weather, smoke, clouds or daylight. SAR has shown to be a valuable data source for the detection of changes related to multiple disasters, whereas in the case of an earthquake the changes in the radar signal are related to structures that have been damaged by the earthquake (Ajadi et al. [2016]). As man-made structures (i.e. buildings and infrastructure) usually result in a consistent scattering of the radar signal over a long period of time, a damaged or collapsed building will most likely result in a different backscattered signal in the post-disaster image and hence be detected as a change when comparing it to the pre-disaster reflection values of the same building. These detected changes may then be visualized on a map that shows indications of possible damaged buildings and used by search and rescue groups for saving trapped individuals in piles of rubble.

Although such damage detection maps are already being generated and distributed on an operational base by the collective International Charter Space and Disasters, the Copernicus Emergency Management Service (EMS) or the Advanced Rapid Imaging and Analysis (ARIA) group of the Jet Propulsion Laboratory (JPL), none of these groups fully exploit the possibilities of timeseries analysis. The International Charter is an organization that coordinates and distributes damage detection maps that have been generated by other parties (i.e. DLR ZKI, UNOSAT), but for every earthquake where maps have been distributed only two contained damage detection maps based on SAR data whereas the rest has been obtained from optical data. Moreover, the Copernicus EMS only focuses on generating damage detection maps from optical data. The ARIA team has developed an algorithm to semi-automatically produce damage proxy maps (showing indications of possible damaged buildings), but these have been based on tri-temporal SAR acquisitions and thus not benefiting from longer timeseries.

In order to detect changes in the backscattering signal and hence create a reliable damage detection map in case of a disaster, it is favorable to be able to analyze timeseries of the radar signal for any area in the world, something the recently launched Sentinel-1 mission can offer (figure 1.1). The Sentinel-1 mission is a relatively new SAR constellation consisting of two satellites in 180 degrees orbital phasing that acquires data over the entire Earth's surface every 3 days in any viewing geometry. More importantly, this mission has an open-data policy and hence provides the opportunity to easily perform multi-temporal data analysis over any location on Earth. Compared to other satellites, the medium spatial resolution (20m) of the Sentinel-1 data will complicate the process of creating accurate building-damage maps on the individual building level. This will hopefully be outweighed by the higher temporal resolution. The latter will provide a higher probability of obtaining data close to the moment of the disaster, resulting in faster damage map processing and the post-seismic image signal to be primarily dominated by the effects of the earthquake. Because of its high temporal resolution and the open-data policy, the Sentinel-1 SAR imagery is a promising remote sensing dataset in terms of rapid disaster response.



Figure 1.1: The radar vision of the Sentinel-1 satellite over a part of the Earth, penetrating the clouds and hence, in normal conditions, always able to observe the surface of the Earth ESA/ATG [2014].

1.2. Aim of the Research

The aim of this research is to develop an algorithm that performs a statistical analysis on radar reflection timeseries obtained by the Sentinel-1 mission in order to generate damage detection maps as output, which can directly be put to use to support humanitarian relief efforts at times of crisis. This algorithm can then be incorporated in a system that, based on input parameters such as location and time, can fully automatically generate damage detection maps that are interpretable and usable for rescue workers in their search and rescue operations. Throughout the design of the system, the focus should be on usability through simplicity so that non-remote sensing specialist such as rescue workers themselves are able to operate the system and generate and interpret the damage detection maps. The goal of the research is therefore to answer the following research question:

"How can the entire Sentinel-1 SAR archive be used operationally for rapid disaster response situations?"

This main question can be divided into several sub-questions:

1. *Is the Sentinel-1 archive usable for detecting building damage?*

An essential part of this research is to exploit the Sentinel-1 imagery and determine whether it can be used to detect building damage caused by an earthquake or military strike during warfare. Next, a processing algorithm will be developed to cancel out noise sources unrelated to the disaster from the radar timeseries and get the best results in terms of building damage detection accuracy.

2. *How does this damage detection algorithm perform in a rapid disaster response situation after earthquakes and intentional damage in conflict areas?*

The developed algorithm will be run and processed as if it were a rapid disaster response situation where time and accuracy are crucial. This will be done for multiple case studies where earthquakes and military strikes took place.

3. *Are the resulting building damage maps sufficiently informative and useful for rescue operation teams in their planning and rescue work?*

The ultimate goal of developing this algorithm and creating the damage detection maps is to assist rescue teams in organizing and planning their rescue operation. Therefore it is of great importance that the usability of the maps are evaluated in terms of applicability, additional information and the data format of the maps.

1.3. Methodology

Time is the most crucial factor in rapid disaster response situations as victims need to be located and rescued as quickly as possible. That is why gathering data and the generation of the damage detection map should take a minimal amount of time. Especially gathering the data could potentially take a lot of time when the damage detection maps are aimed to be generated by exploiting timeseries for any area on Earth. Here, the options are either to rapidly download tens to hundreds of SAR images once a disaster happens or to maintain a data archive of SAR imagery for the entire Earth which will probably have a size of petabytes.

Google Earth Engine Coincidentally, such an archive has recently been launched on a platform hosted by Google: The Google Earth Engine (GEE). GEE is an online, open-source processing tool that allows users to run algorithms on multiple geo-referenced earth observation imagery and vectors stored on Google's infrastructure, with one of these datasets being Sentinel-1 SAR Ground Range Detected (GRD) data. It provides opportunities in various remote sensing applications, such as the monitoring of deforestation, surface water and glaciers. Moreover, the speed and accessibility of GEE, together with the type of datasets it provides, make it interesting if it also can be used in rapid disaster response. By developing an algorithm for the SAR imagery and combining it with other remote sensing techniques available in GEE, an approach can be developed that is simple and performs automatically, making it directly of use for rescue operations.

Damage Detection Algorithm The damage-detection algorithm should generate building-damage maps which show locations of significant change in the returned radar signal. The average signal of a certain number of pre-disaster images may be considered as background noise, being slight deviations in the backscattered signal that can occur without a major incident taking place and hence are unrelated to the earthquake. Comparing this background noise with a post-disaster image will, through applying algorithms, result in the building-damage maps where the changes will indicate buildings that collapsed as a result of the disaster. The resulting damage map is aimed to have an outlay such as pictured in figure 1.4. Furthermore, the platform hosted by Google might allow for including contextual information to the damage detection maps such as the type of building that collapsed. This would improve the interpretability of the maps when, for example, an earthquake hits at night and causes buildings to collapse. Once a new post-disaster acquisition is available, the generated damage detection map might indicate a building as damaged that, by applying contextual information, can be identified as a school and as the earthquake struck at night the user can assume that no one was present in the building at the time of the disaster. This would save time for rescue operations at other locations as this damaged building is not a priority any more.

Damage Detection Maps Preferably, the resulting damage detection maps are generated instantly once the disaster happens so that the maps can be used during decision-making and planning of the rescue operations by i.e. the USAR team. This gives the generation of the damage detection maps a time period of 24 hours after the disaster happened for them to be used in decision-making, as the USAR team are supposed to be able to leave The Netherlands in case of an emergency and travel to any destination in the world within 24 hours (USAR [2015]). However, the satellite imagery might not be available right after the disaster and can take up to three days to be acquired. In order to show the added value of a damage detection map in case it would become available somewhere in the three different phases the USAR team goes through during a rapid disaster response, a schematic graph has been made and is depicted in figure 1.2. Here, three phases have been depicted: monitoring, mobilizing and deployment. During monitoring, the head of the USAR team tries to find information on the event and determines whether or not they should offer their help. If the answer is yes and their help is needed, they move onto the next phase and the value of the map for the monitoring phase drops. However, it can still be of use for determining whether or not to go until they departed and thus the map is still valuable. Next, they start mobilizing to plan for a landing site, organize their team and gather the right material. Once departed, the map is not of use anymore for determining whether or not to go or to help them planning for a landing site. Note that besides the usefulness of the maps during decision-making, the maps can also be useful during the actual deployment of a search and rescue teams as it indicates damaged buildings which can then be visited by the teams in order to search for possible victims and perform rescue operations. The map is therefore most valuable in the beginning and drops as it is less likely to find and rescue survivors. The time period the generated maps can still be of use after the disaster hit, can be up to several days as long as the survival rate of human beings in debris is still significant, meaning that victims can be rescued in that period.

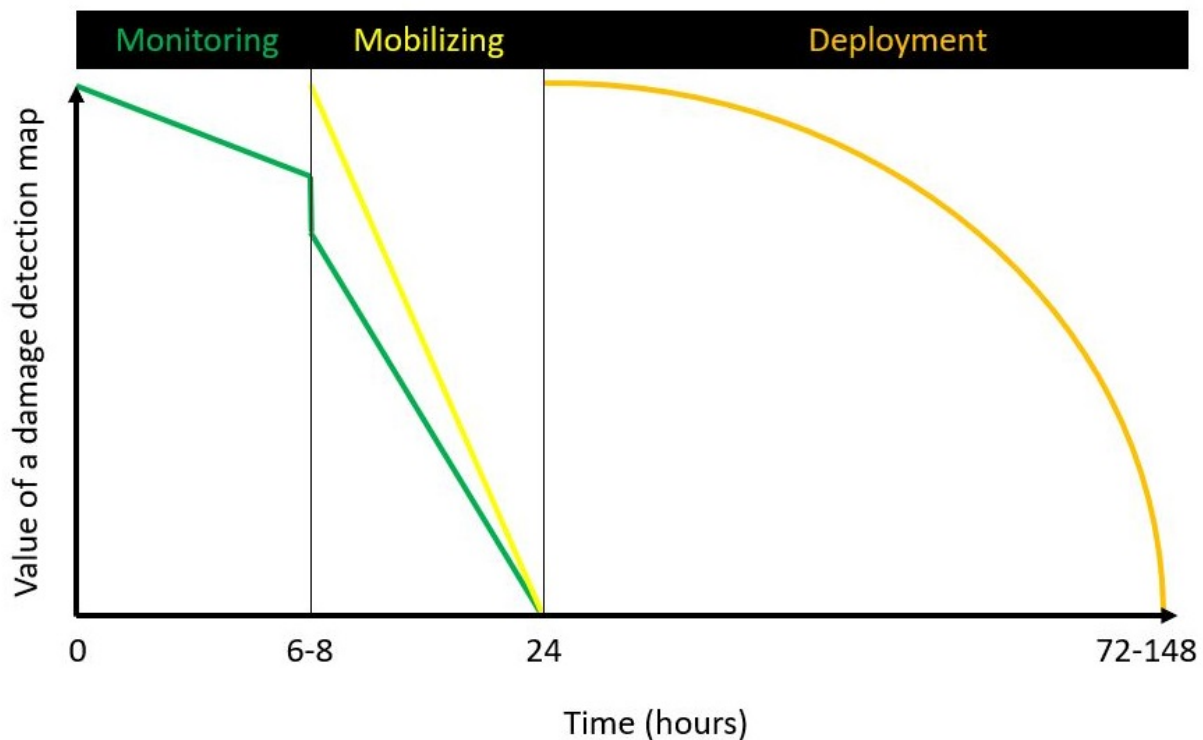


Figure 1.2: Schematic value of a damage detection map at the point in time and USAR phase when it becomes available. For monitoring this value is high as it can help determine whether or not to go and start mobilizing. If they decided to mobilize, the value drops but still can help them decide up until they depart. During mobilizing the map can help them determine where to land and organize the team they need to bring, also allowing a damage detection map to be useful up until the USAR team departs. During deployment, the map can help the team prioritize locations of where most help may be needed until all areas have been scanned and no living victims may be found anymore.

As an example, the time period of significant survival rates of human beings in debris has been encountered by search and rescue operations of the Kobe City Fire Department after the 1995 M7.2 earthquake in Kobe, Japan as depicted in figure 1.3 and during other disasters as described by Coburn et al. [1992]. The decrease in significant survival rate is correlated to the type of building material used in the impacted area. The trend in survival rate in Kobe is therefore comparable to that of weak stone masonry houses that can be found in China or Italy, while reinforced-concrete buildings in Mexico City indicated significant survival rates of up to 6 days. The difference can be explained by the severity of the events and the loss of survival space in debris, related to the building material (Murakami [1996]).

Final System The goal of the algorithm as a whole is for it to be simple and easy to access so that the user, for example a search and rescue worker, can use the system to generate these damage detection maps without being a remote sensing specialist. This can be accomplished by allowing the algorithm to run by using a minimal amount of parameters as input from the user and complete the damage detection maps from there on automatically, thus being a disaster-response based system. Note that this approach might be slightly adjusted for it to be effective in rapid disaster response situations due to intentional damage during warfare. Although rescue operations in these situations might be more complicated, or even impossible, during warfare depending on the situation of that area in terms of continuous military strikes and the political situations, maps indicating possible sites of damage can still be of use in order to monitor the amount and locations of damage. This continuous monitoring of an area of interest can be accomplished through a monitoring system where every new acquisition is used for damage detection and, in the case of a bombardment, the resulting signal is monitored.

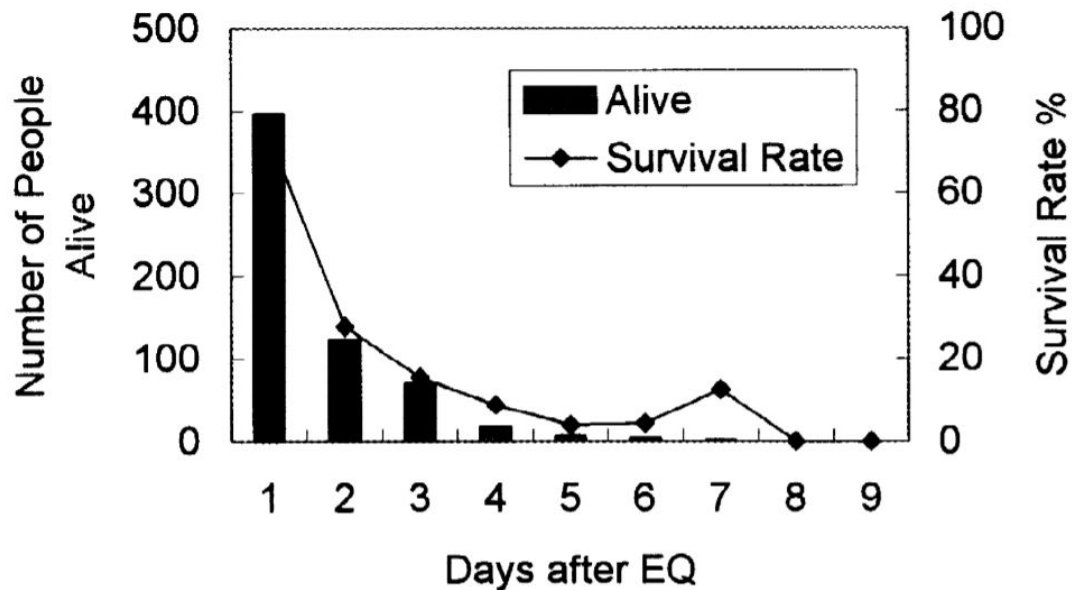


Figure 1.3: Survival rate of victims trapped under debris along days after the M7.2 Kobe, Japan earthquake in 1995, as encountered by the Kobe City Fire Department during search and rescue operations. It can be seen that the survival rate of victims trapped under debris becomes insignificant after three days, which is comparable to similar types of building material in Italy and China (Murakami [1996]).

1.4. Thesis Lay-out

In chapter two, background information will be discussed regarding current practices in search and rescue operations, especially the Urban Search And Rescue team of The Netherlands, and regarding the use of remote sensing sources operated in rapid disaster response situations. Furthermore, it will be discussed why SAR systems, and in particular the Sentinel-1 satellite mission, are valuable for the search and rescue application. The usability of the Google Earth Engine in terms of accessibility and how it operates is discussed in chapter three. The algorithm development will also be explained in this chapter on a step-by-step basis including the assumptions that have been made. The focus of chapter four lies on demonstrating the applicability of the algorithm on various test cases in order to assess the algorithm in actual rapid response situations. This goes together with the usability and accuracy of the damage detection maps. Finally, chapter five will present the main topics of discussion that concern implications on the presented results and points of improvement as well as brief answers to all of the research questions.

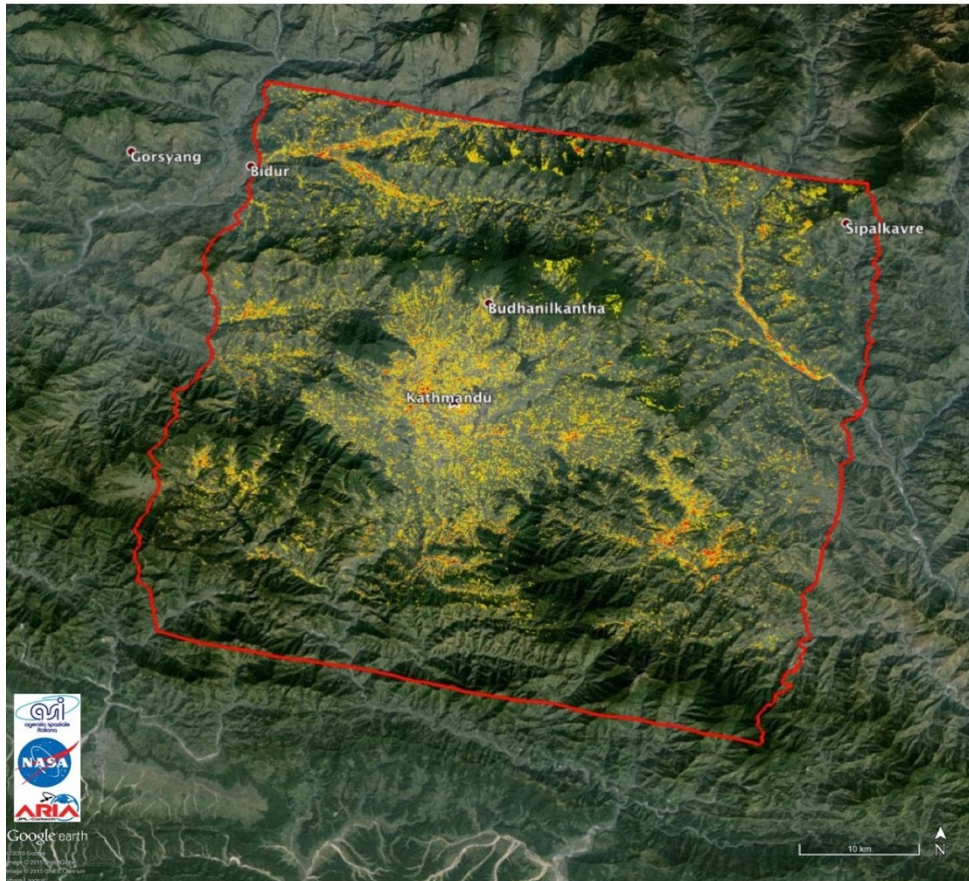


Figure 1.4: Damage Proxy Map derived from COSMO-SKYMed SAR data and draped on Google Earth for the area of Kathmandu after the M7.8 2015 Nepal earthquake. It indicates locations of possibly damage buildings based on a tri-temporal change detection approach (Yun et al. [2015]).

2

Background Information

This chapter will discuss the general challenges encountered within rapid disaster response during humanitarian crises related to building damage, such as natural disasters and intentional damage during warfare. Following, the various remote sensing techniques that are currently applied in rapid disaster response situations and the advantages and disadvantages of these techniques will be discussed. Summarizing these aspects will show why the Sentinel-1 mission can provide interesting results in terms of rapid disaster response and thus why this satellite mission can be useful.

2.1. Humanitarian Crises related to Building Damage

Natural disasters such as earthquakes, floods, volcanic eruptions and forest fires are responsible for hundreds of thousands of casualties every year, as seen in figure 2.1. Depending on the unpredictability and severity of these natural disasters, many people in the vicinity of the area where the natural disaster strikes may be caught by surprise and thus limited in their time to evacuate. In contrary to earthquakes, some other natural disasters such as floods, volcanic eruptions and forest fires can be predicted up to some extent on a daily basis by monitoring precipitation (Doswell III et al. [1996]), ground deformation and seismicity (Chouet [1996]), or moisture content of vegetation and temperature (Stocks et al. [1989]), respectively. Additionally, for these events early warning systems can be used as the destructing force (rising water level, lava or fire) has to travel a certain distance from its source to reach the surrounding population. Comparing the travel velocity of one of the former mentioned natural disasters to the travel velocity of the surface waves caused by an earthquake (~ 3 km/s for Rayleigh waves and even higher for Love waves (Fowler [1990]) makes it valid to state that earthquakes have a much more instantaneous impact. The unpredictability and instantaneous effect of earthquakes, accompanied with the extent and high investment costs to minimize negative impact are all aspects that have caused earthquakes to account for nearly 60% of all disaster-related mortality in the period 2001-2011, making earthquake the deadliest natural disaster on Earth (Bartels and VanRooyen [2012], Roser and Ritchie [2018]).

Potential casualties from building damage can be classified by three causes of death: direct, trapping and medical effects (Boulogne [2018]). The direct effects are related to the falling of debris and collapsing of infrastructure which kill victims on impact, meaning that the moment of death is almost instantaneous. Trapping effects relate to individuals being trapped beneath collapsed structures and debris, hence causing the individual to lack access to air, clean drink water and/or food. A human would need all of these facets to survive until he/she is localized and rescued. Naturally, the lack of one of the three facets have different impacts on the time period one would be able to survive, with air being the most important facet. The last cause of death, medical effects, is related to the lack of medical equipment and/or attention. After an individual has survived the primary shaking due to the earthquake or has been rescued from burial under debris, he or she might suffer from severe injuries that need medical attention but this cannot be given in time due to the chaos resulting from the humanitarian crises.

The severity of the direct effects could be reduced by taking precautions, such as: using building materials (reinforced concrete) and structures (base isolators) that are able to withstand the shaking force caused by the shock wave and reinforcing potentially dangerous slopes to prevent any debris from falling. The amount of casualties related to medical effects can be reduced by faster supply of medical equipment and better training and supplyment of personnel in the vicinity of disaster prone areas. However, regarding the trapping effects the only possibility to reduce the amount of casualties is locating and saving trapped individuals as quickly as possible. This response time from the moment the earthquake occurs to the actual saving of people is influenced by the remoteness of the area, the ability to communicate with and within the area and how fast trapped individuals can be located. Especially the latter can be greatly improved by providing preliminary information on locations of possible damage buildings. This research focuses on the middle class of potential casualties due to disasters: reducing the time it takes to localize possible trapped individuals, i.e. the response time.

The importance of reducing the response time also holds for disaster situations related to intentional damage during warfare that is located in civilian living areas. Once a military strike with sufficient explosion power to damage buildings is aimed at a civilian area, casualties may arise instantaneously due to the explosion itself or due to indirect effects when becoming trapped in debris without access to air, water and/or food for a significant period of time (minutes to hours). In order to minimize the amount of casualties related to becoming trapped, again the only solution is to decrease the response time by locating the individuals as quickly as possible. Naturally, the ability to locate individuals is different for each situation when rescue teams, for example, are further away from the actual bombings to host refugees in predetermined camps and not perform the actual rescue operations when these are too dangerous. Although the approach of disaster management during warfare may be different compared to rapid response situations due to natural disasters, there is still a need to quickly gather preliminary information on the situation that support locating trapped individuals.

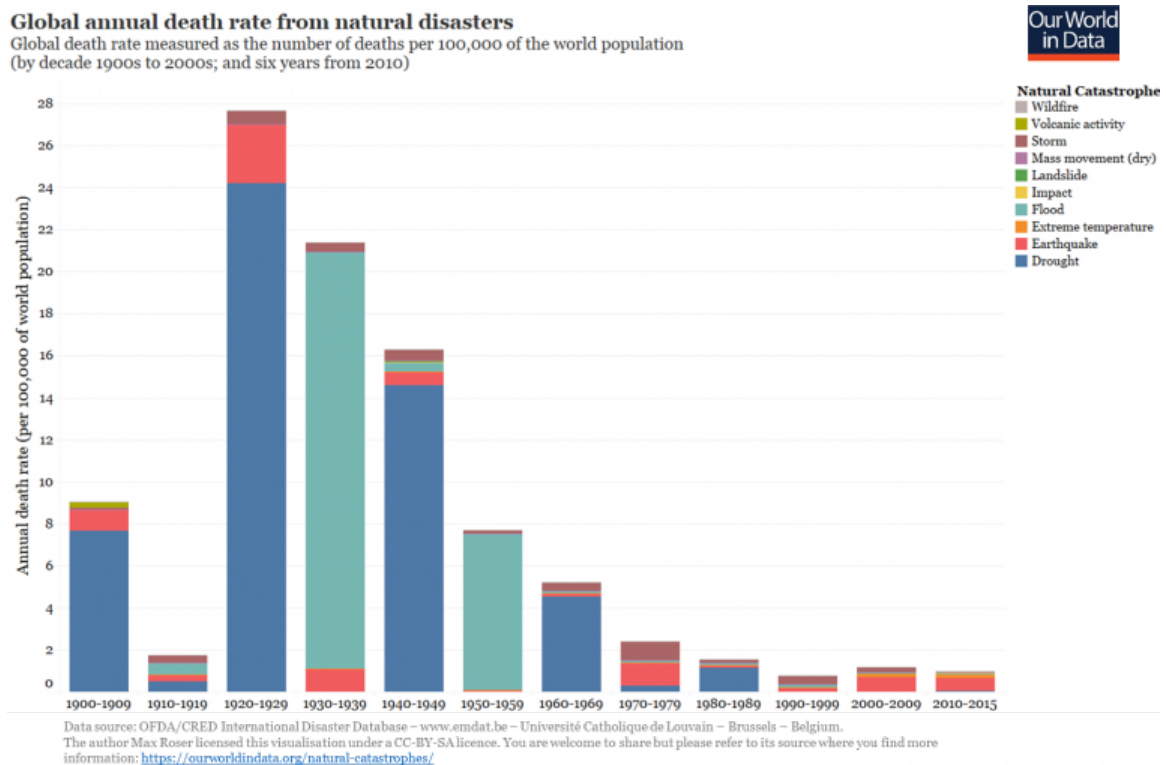


Figure 2.1: Absolute number of annual global deaths from natural disasters. Data source: OFDA/CRED International Disaster Database. (Roser and Ritchie [2018]).

2.2. Current Search and Rescue Practices

There are a lot of different approaches in order to reduce the response time and thus speeding up the localization of trapped individuals. There are two distinctions that can be made: the ground teams that do the actual rescuing and localization of individuals with various instruments, and remote sensing techniques that mainly operate on locating damaged buildings or even trapped individuals through drones.

Once a humanitarian emergency strikes in a country, the first step that is taken in order to coordinate rescue operations is to initialize the Local Emergency Management Authority (LEMA). This team can be an organized set of native members, but if such a team is not predefined (for example in developing countries) the help of the United Nations Disaster Assessment and Coordination (UNDAC) institute or the European Union Civil Protection Mechanism (EUCPM) may be requested, whom take over the tasks of assessing the first phase of sudden-onset emergency and coordinate the incoming international relief. The LEMA will set up an On-Site Operations Coordination Center (OSOCC) where the disaster relief will be coordinated. Optionally, the LEMA may put out a request for international help by global USAR teams through the Global Disaster Alerting Coordination System (GDACS) concerning a situation description and the kind of help that is needed.

In case a disaster resulting in building damage occurs, the head of the Dutch USAR team evaluates the situation on various aspects, such as the severity of the disaster (i.e. magnitude of an earthquake or windspeed of a hurricane), the developed status of a country and the specialties of his team that may be useful for that particular disaster, in order to determine whether or not to alert the team. This phase is also known as the first step in USAR deployment: monitoring. Once a request for international help has been sent by the LEMA and the head of the Dutch USAR team decided that their help is useful, he asks the ministries of Internal Affairs, External Affairs and Defense for permission. That decision group decides on whether the Dutch USAR team will offer its services. Once the steering group gave its permission, the USAR team that will travel to the specific country, consisting of 62 policemen, firemen, medics and structural engineers, gathers and prepare themselves by checking the kind of equipment that is needed. This phase is called: mobilizing. They can be ready to depart within 6-8 hours and on site within 24 hours anywhere on Earth, depending on the timeliness of decision making and availability of air transport. Due to these two factors, the practical indication of their arrival time is 24 to 72 hours after the disaster. If everything is set and the USAR team is on its way to the location of the disaster, the last USAR phase is entered: deployment.

Meanwhile, the LEMA will follow predefined guidelines, determined by the International Search And Rescue Advisory Group (INSARAG), an institution part of the United Nations Office for the Coordination of Humanitarian Affairs (OCHA), in order to coordinate rescue operations (INSARAG [2015]). These Assessment, Search and Rescue levels are as follows:

- **ASR1: Wide Area Assessment**
The first step in the USAR planning process is to estimate the size of the disaster in terms of severity and scale. Here, it is of importance to divide the area in sectors to maintain overview, identify possible hazards and prioritize tasks for a plan of action.
- **ASR2: Sector Assessment**
When sectors have been divided and rescue teams assigned to these sectors, a quick and dirty scan of each sector is made in order to prioritize tasks within an entire sector and act on it. Naturally, the goal is to rescue as many lives within the least amount of time, so rescue missions are rated on level of difficulty. Note that the main objective in this stage is not to perform actual rescue operations but if a clear opportunity to save a victim presents itself it is allowed while not getting stuck at that location for longer than an hour.
- **ASR3: Primary Search and Rescue**
During or after ASR2, USAR teams are ordered to perform search and rescue operations with simple equipment such as search dogs and listening equipment. Here, the easier rescue operations are performed which should take no longer than a couple of hours. In this way the lifesaving opportunities are maximized.
- **ASR4: Secondary Search and Rescue**
When persons have been trapped in thick layers of debris, medium and heavy teams are summoned. These teams use heavy measures where digging and stabilizing the remaining structures might be necessary. These kind of operations may take multiple hours and by the end of this level all survivable voids have been searched.

- ASR5: Full Coverage Search and Rescue

The final Assessment, Search and Rescue level is used to inspect all structures within a sector and clear up the debris so that all life and deceased victims have been recovered.

The sequence of activities for both the Assessment, Search and Rescue levels by the search and rescue teams at the location and the various phases that are being followed by the Dutch USAR team is depicted in figure 2.2. It shows that preceding the humanitarian disaster resulting from building damage, remote sensing data is collected. This is done on a regular or irregular base, depending on the type of platform and the amount of resources available for such measurement campaigns which will be explained more into depth in section 2.3. Then, once the disaster occurs, the local authority goes through the different ASR levels in order to manage the search and rescue operations in a coordinated way. Meanwhile, the Dutch USAR team enters the monitoring phase in which they will decide whether they will or will not be available for support. If the answer is yes and their help is requested by the local authority they start mobilizing and planning their departure. Once all is set and they are ready to depart they fly to the country of the disaster and start offering help. It takes roughly 24-48 hours from the moment of the disaster to the moment of arrival in the country. Where the USAR team will be able to assist the local authority the most depends on how quickly the search and rescue operations in the area of the disaster are managed and thus how fast the ASR levels are completed.

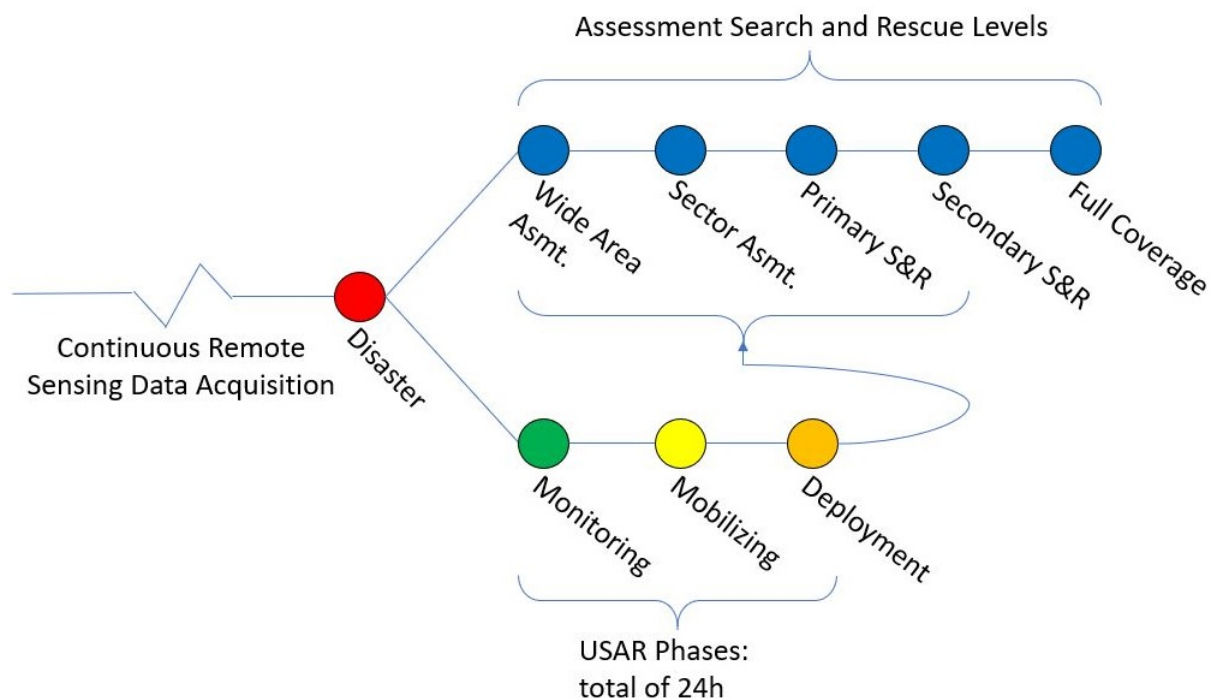


Figure 2.2: Flowchart showing the sequence of activities prior and after the disaster for both the local authority managing the ASR levels and the Dutch USAR team. The ASR Level where the USAR team can assist the most upon arrival depends on the arrival time of the USAR team itself and the speed of which the rapid disaster response in the country of the disaster is being managed.

Damage Assessment (ASR1 and ASR2) Currently, the determination of sectors and prioritizing actions in levels ASR1 and ASR2 is done by using any kind of external information sources the USAR team can find. In practice this means that quick and dirty internet searches on various platforms such as: Maps, OpenStreetMap and Google Earth are performed as well as using travel guides and paper maps. If one or multiple of these information sources are available, they are consulted in order to scan the area and locate large infrastructures and urban areas with potentially higher populations. Additionally, the Dutch USAR team occasionally consults the damage maps generated by GMES EMS if they are available. These maps show indications of damaged buildings within an urban area containing possible trapped individuals and have been generated by using the most recent high resolution optical data that is available and manually look for damaged structures.

Also the help of MapAction can be requested and consulted, which is a group of volunteers consisting of a field team (24-48 hours of a disaster striking) that will observe and manually map the state of collapsed structures and a select few that provide specific technical capacity and remote support. MapAction quickly gathers data concerning population density and height profiles of the country/region, status of roads, railways and communication networks and need of medical supplies and conveys this information in the form of maps. As the situation on the ground evolves, the volunteers help national authorities, aid agencies and emergency teams understand the fast-changing needs of affected communities. The relations between all the organizations and teams that have been discussed in this section are depicted in figure 2.3 for clarity.

Emerging techniques in the field of emergency response are text mining and the use of remote sensing data. Text mining is a technique where large quantities of textual data can be scanned and analysed, where for example messages from twitter (tweets) are scanned on location and possible images or mentioning of damaged structures (Huang and Xiao [2015]). Additionally, with ever improving remote sensing technologies there is an increasing amount of means available to generate an overview of damaged buildings and indicate where rescue teams should look. Several platforms can be considered for this, being: drones, airborne and spaceborne which will be discussed further in subsection 2.3.

Search and Rescue (ASR3 through ASR5) The actual localization of trapped individuals in Assessment, Search and Rescue levels 3 and 4 is done with the help of search dogs, listening equipment, infrared sensors and search cams. The search cams are equipped with red lighting to improve distinction of depth. Additionally, the help of locals may be used as they might know whether people were present inside a building during the moment of collapse. Most of these approaches are especially of use in ASR3 as they can only be used in Rapid Search and Rescue operations of primary, shallow victims. For example, thermal radiation from humans does not penetrate concrete or other building materials and thus prevents infrared sensors from detecting any signals from humans covered by debris. Once persons that have been trapped in thick layers of debris (ASR4) need to be localized, more technically advanced equipment is required. Once these search and rescue levels have been completed the rescue teams start with the full coverage of the damaged areas.

New technologies to assist with the rescue operations are improved listening sensors which interact through wireless communication and are therefore easier to set up and can be left to measure without supervision in the case victims start making noise at a later time. Furthermore, drones are being developed that can perform quick laser scanning operations in order to detect openings for rescue workers to pass through and swarms of drones that can actually enter the debris and scan for tunnels and possible victims. The European Union also initiated the INACHUS project which aims at achieving time reduction for USAR teams by providing wide-area situation awareness and improved survivor localization. Time reduction through wide-area situation awareness is achieved by using Common Operational Picture (COP), a software tool to visualize the real-time response progress and incorporate additional desired data from Unmanned Aerial Vehicles (UAVs) and 3D models, and the Emergency Support System (ESS) which allows for digital completion of INSARAG forms and data sharing. Improved survivor localization is acquired by using a robot equipped with optical, infrared and radar sensors, a gas detector alerting on gases consistent with living human beings, cameras, microphones and speakers, ground-radars that can penetrate deeper than infrared sensors and detect motion and last seismic sensors that detect vibrations. All of these innovative techniques are being tested in practice and may be operated in rescue operations in the near-future.

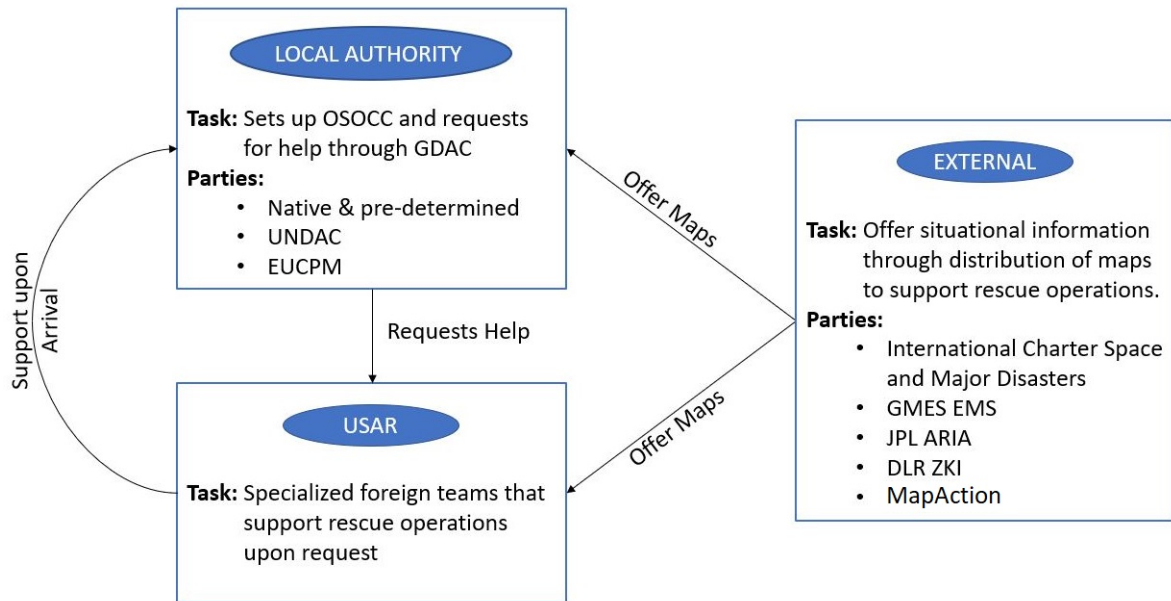


Figure 2.3: Flowchart showing the relations between the organizations discussed in this section. Once a disaster occurs, the local authority (consisting of a native group or a team set up by either the UNDAC or EUCPM) organizes the entire rapid disaster response. If help is needed for the search and rescue operations, help can be requested by the USAR teams. Meanwhile, there are various parties that offer maps that aim to improve the situational awareness and assist the local authority and USAR teams in their rescue operations.

2.3. Literature Review: Remote Sensing in Rapid Disaster Response

Traditionally, the prioritization of rescue areas is determined by the LEMA, which use external information sources such as: Maps, OpenStreetMap, Google Earth for decision making. However, with ever improving remote sensing technologies there are other means available to generate a preliminary overview of damaged buildings and rescue priorities. Remote sensing is currently used for some natural disaster monitoring programs such as flooding, landslides and wildfire, though there are also difficulties associated with the rapid acquisition of data and provision of a robust product to emergency services as an end-user (Joyce et al. [2009]). The need for a robust system providing damage detection maps in search and rescue activities was confirmed by Boulogne [2018], stating that preliminary overviews of where buildings are damaged and priorities are located are limited and depend on the developed status of a country. Although the Copernicus GMES EMS team only processes optical imagery and hence are weather dependent, causing an insecurity of when maps will become available, they provide the most often used remote sensing data. Rapidly generated building damage maps could potentially save time during Assessment, Search and Rescue levels 1 and 2, leaving more time for saving victims. Several remote sensing platforms can be considered (UAVs, airborne and spaceborne), each having their advantages and disadvantages.

2.3.1. UAVs

UAVs can assist in wide-situational awareness by scanning which structures have been affected by the event as well as the extent of the damage to these structures (Erdelj et al. [2017]). Additionally, UAVs can act as early warning systems through structural and environmental monitoring, support other applications with data fusion, track the movement of affected people and deployed rescue teams, act as standalone ad hoc communication system and can search for and rescue people lost, injured, or trapped by debris (i.e. the swarms of drones mentioned in the previous subsection) (Câmara [2014], Erdelj and Natalizio [2016]). The advantage of drones over the other remote sensing platforms are their multi-purpose possibilities. For example, the usage of drones in search and rescue operations can be expressed by using them as damage detection platforms as well as a communication system that scans possible text messages or pictures send from trapped individuals which in turn can be used to locate that specific individual (Câmara [2014]). Due to all of these potential applications of UAVs, the American Red Cross advocated for UAVs as one of the most promising UAVs powerful new technologies in rapid disaster response situations (American Red Cross [2015]).

Focusing on the effectiveness of UAVs in wide-situational awareness, UAVs can be equipped with sensors to either **detect damaged buildings** which possibly host trapped individuals (Electro-Optical, LIDAR or Radar) or to **detect individuals** inside damaged structures (Electro-Optical, Infrared, penetrating radar or tracking radio signals of mobile phones). The type of sensors that can be used depends on the availability of certain UAVs that can carry various payloads. The American Red Cross has identified five groups of UAVs, each with distinctive flying altitudes, payloads and flight endurance:

- Group 1: Hand-launched, lightweight, low payload drones
Drones weighing up to 10 kg. and flying at a maximal altitude of 300 m. Most commercial aircraft are battery powered and have a short endurance (20 minutes to 2 hours) but some fuel-cell powered drones can be hand-launched and have an endurance of 8 hours.
- Group 2: Long endurance reconnaissance and surveillance
These aircraft weigh up to 23 kg. and have a maximum altitude of 1000 m. They operate on a gas or diesel propulsion system and can fly for 24 hours straight. These relative small sized aircraft can be equipped with high quality electro-optical camera and infrared cameras.
- Group 3: Long endurance, large payload drones
These aircraft are again larger, weighing up to 600 kg. and fly up to 5500 m. The larger engines compared to group 2 give these aircraft the possibility to carry heavier payloads despite their shorter endurance (8-10 hours). From this group onward the UAVs need a significant runway to take off.
- Group 4: Heavy lift
Group 4 UAVs are special in the sense that they are adapted manned aircraft to unmanned and can be optionally piloted. The weight of these aircraft exceeds 600 kg. and can take off vertically (helicopters).
- Group 5: Long endurance, high altitude reconnaissance and surveillance
These aircraft have been specifically built as unmanned vehicles and again weigh 600 kg. or more. Some types of UAVs within this group can fly up to a week.

Detecting Building Damage With search and rescue operations, remote sensing systems mounted on UAVs can provide high spatial resolution imagery with a high level of temporal readiness as the systems can be put to use right after the disaster struck. Naturally this only holds if the right type of material is available. More specifically, UAV groups 2 to 5 (with the exception of group 4) can be operated for large scale building damage detection through electro-optical, LIDAR or radar sensors as these fixed-wing UAVs can span large areas and have the capacity to carry these payloads. Group 4 aircraft are only used to transport people to/from disaster locations or resupply and distribute gear to remote locations. Building damage detection through LIDAR and electro-optical scanning, however, is generally completed by mounting it on rotary-wing UAVs due to their improved manoeuvrability and ability to hover compared to fixed-wing UAVs. In order to perform damage detection by using any of the mentioned sensors, preferably for all of these techniques a recent pre-disaster map or scan is needed to compare the post-disaster imagery with (American Red Cross [2015]). Unfortunately, this pre-disaster imagery is not always available for disaster-prone areas. Gathering the data for such a large area (over 100 km² in case of an earthquake) is very cost and time intensive, something not every country can afford and resulting in a low temporal-resolution of the dataset. Without this up-to-date pre-disaster imagery automatic building damage detection is difficult. Alternatively, electro-optical and LIDAR can be performed in order to detect damaged buildings using only post-disaster imagery but this should then be checked manually and thus in its turn is time intensive, time search and rescue teams can better spend otherwise (Câmara [2014]).

Detecting Individuals The detection of individuals through UAVs is easier to use on an operational basis compared to detecting building damage. These type of sensors need to be deployed on low altitudes for which UAVs from group 1 bear sufficient power for the payload. An additional advantage here over aircraft from groups 2 to 5 is that no runway or expensive equipment is needed. Erdelj et al. [2017] also recommended that commercially available UAVs should be used for disaster management due to their availability, affordability, and ease of use. The search for individuals would really emphasize the manoeuvrable character of the lightweight UAVs. The disadvantage, however, of lightweight UAVs is there is still a need for a UAV station where the drones can be managed from and possibly recharge. The operation of the UAVs, as well as setting

up such an installation, would still require manual interaction, which is costly. Concepts for automation of the operation of the UAVs are available but they are not operational yet (Câmara [2014]). This automation or some sort of regulation would also reduce the chance of UAVs operated by different teams colliding with one another due to miscommunication between those different parties, a reasonable scenario according to Boulogne [2018]. Furthermore, the application of UAVs in detecting individuals is time intensive and therefore not applicable on a large scale. This would definitely assist in ASR 3 and 4 but not in levels 1 and 2, which we are currently focusing on.

2.3.2. Airborne

The operability of airborne systems in search and rescue missions is comparable to that of UAV groups 2, 3 and 5. By flying, and hence not being affected by damaged infrastructures, airplanes are quicker to reach the affected area and start taking measurements compared to group 1 drones. However, this means that an airplane with such equipment, a decent runway and the right personnel should always be in the vicinity in order to be effective. Airborne systems can be equipped with electro-optical, near-infrared (NIR), thermal infrared, synthetic aperture radar or LIDAR systems with high spatial resolutions and are able to scan large areas, thus having a high spatial extent. The instruments are used to detect building damage and hence create an overview of the affected structures. Localization of individuals is possible in open fields by using high resolution electro-optical or infrared cameras, but trapped individuals cannot be localized as the electro-optical nor the infrared signal is able to penetrate debris. Similar to the long endurance UAVs, different sensors can be mounted on the aircraft and a comparison of the operability of these sensors in building damage detection has been completed by Dong and Shan [2013]. They also noted that using pre- and post-disaster imagery instead of only using post-disaster imagery clearly improves the accuracy of the results.

Again, however, the limitation of relying on pre- and post-disaster imagery for building damage detection is that it is not always available, especially in developing countries (Li et al. [2011]). And even when pre-event data is available this might not always be usable due to colour and spectral differences between both datasets (Taskin Kaya et al. [2011]). For electro-optical and LIDAR sensors it is possible to detect building damage based on only post-disaster imagery but this again is time intensive. Note that these activities can also be performed by the UAVs described above. The advantage of using UAVs over manned aircraft is that they can fly at lower altitudes and hence create higher resolution maps. Besides, by letting UAVs perform so-called dull, dangerous or dirty tasks, responders can be allowed to perform more important matters and crew fatigue can be avoided, which would decrease their effectiveness in searching and increase the likelihood of pilot error. Although UAV systems can require significant investment and maintenance costs, manned missions are also expensive regarding purchase and operational costs (American Red Cross [2015]). All in all, manned damage detection missions are definitely useful but with improving UAV technology the latter might be a more beneficial alternative.

2.3.3. Spaceborne

The main disadvantage of the usage of either airborne or UAV systems as a remote sensing platform in rapid disaster response is that the usability of those platforms depends on the availability of the right equipment at location and the availability of pre-disaster imagery, something that is not always the case during a humanitarian crisis and even less likely in undeveloped countries. The developed status of a country generally correlates to the amount of resources available to prepare for a humanitarian crisis. Specifically for remote sensing techniques, once not enough budget is available to collect up-to-date pre-disaster imagery, damage detection through remote sensing techniques rely on using only post-disaster imagery which needs manual interaction in order to detect collapsed structures, and thus takes time.

Spaceborne systems, however, offer qualities that comply to the disadvantages of drone and airborne systems and can therefore be a perfect addition in rapid disaster response situations. Spaceborne systems in rapid disaster response situations rely on either **optical** or **radar** systems and have a fixed temporal resolution to acquire imagery on a regular basis. Previous imagery can therefore be used as a reference for (automatic) damage detection methods. Additionally, the extent of data acquisition is larger for spaceborne systems compared to UAV or airborne systems and hence the possibility to generate damage detection maps for a larger area. The only disadvantage of the fixed revisit time of satellites is that the data might not be available right after the earthquake but depends on the orbital flight path of the satellite and cannot be influenced by human interaction. It might therefore be that UAV and airborne systems are ready for use sooner than the next data acquisition by the satellite, but the up-to-date pre-disaster imagery acquired by the satellite can result in damage detection maps still being available sooner than UAV or airborne data based damage detection

maps. The applicability of spaceborne remote sensing techniques in rapid disaster response can thus be evaluated using four key parameters: timeliness of data provision, time frame for data processing to damage map, geometric resolution and spatial extent.

In the first stages of rapid disaster response usually a trade-off is made between the response time and depth of analysis or mapping accuracy. As time progresses since the time of the event, more teams provide various maps whereas the more accurate results also take more time to generate and validate. A pre-validated automated method could decrease the response time significantly as no human involvement would be needed. However, until now only a few approaches with radar and optical data have been targeted for automation as will be discussed later on. This is partly caused by the first rapid assessment preferring visual qualitative approaches over automatic and quantitative ones due to the higher level of interpretability and reliability of the former approach for rescue workers (Voigt et al. [2011]). Here, quantitative classification focuses on the ratio of collapsed versus non-collapsed buildings in a certain area, whereas qualitative classification focuses on the severity of the damage according to a damage classification scheme. One of these damage schemes is the well-established European Macroseismic Scale (EMS-98) classification scheme, which denotes the degree of damage to a building caused by a destructing humanitarian crisis, as shown in figure 2.4.

Masonry buildings	Reinforced buildings	Classification of damages
		Grade 1: Negligible to slight damage (no structural damage, slight non-structural damage)
		Grade 2: Moderate damage (slight structural damage, moderate non-structural damage)
		Grade 3: Substantial to heavy damage (moderate structural damage, heavy non-structural damage)
		Grade 4: Very heavy damage (heavy structural damage, very heavy non-structural damage)
		Grade 5: Destruction (very heavy structural damage)

Figure 2.4: An overview of the classification of Damage to Masonry and Reinforced Buildings according to the EMS-98 damage classification scheme showing the different grades of destruction Grunthal et al. [1998].

Various parties, both nationally and globally, operate during rapid disaster response situations whom all produce their own damage maps, leading to confusion and misinterpretation. During the Haiti earthquake (2010) an overflow of maps (i.e. reference, damage assessment, situation, overview and further specialized maps at different scales) became available on ReliefWeb (Voigt et al. [2011]). As in these situations no crucial time can be lost, the International Charter Space and Major Disasters center has developed a uniform format. The charter is a worldwide collaboration that, upon request of an authorized user, gathers, processes and distributes Earth observation assets from different space agencies for rapid response to major disaster situations. Following a successful activation of the Charter, disaster relief organizations may receive satellite data of affected areas within a matter of hours or days; depending on the type of disaster and available satellite resources. All parties should adapt their products to a uniform format in order to create an ideal information management system for the rescue teams to use, whereas these products could possibly also include reference information regarding infrastructure and amount of buildings in a certain area. During a certain disaster the Charter shares information on the event, depicts the generated products and links to co-operating disaster monitoring organizations such as Copernicus GMES EMS, DLR ZKI and the JPL ARIA team. An example of a damage grading map of the M6.9 Lombok earthquake on 06-08-2018 generated by the UNITAR/UNOSAT team and distributed by the Charter is depicted in figure 2.5.

All but two of the damage grading maps that have been distributed by the Charter for activations related to earthquakes are based on optical data whereas the use of SAR data might be complementary. The damage detection approach that is proposed in this research should therefore be seen as an addition to the existing maps. Furthermore, the resulting damage map should be interpretable and the algorithm reliable in order to make rescue workers comfortable working with this type of data. In order to get a clear overview of the possible damage detection applications that can be generated by using either optical or radar data from spaceborne platforms, the next two subsections will discuss various studies regarding these approaches.

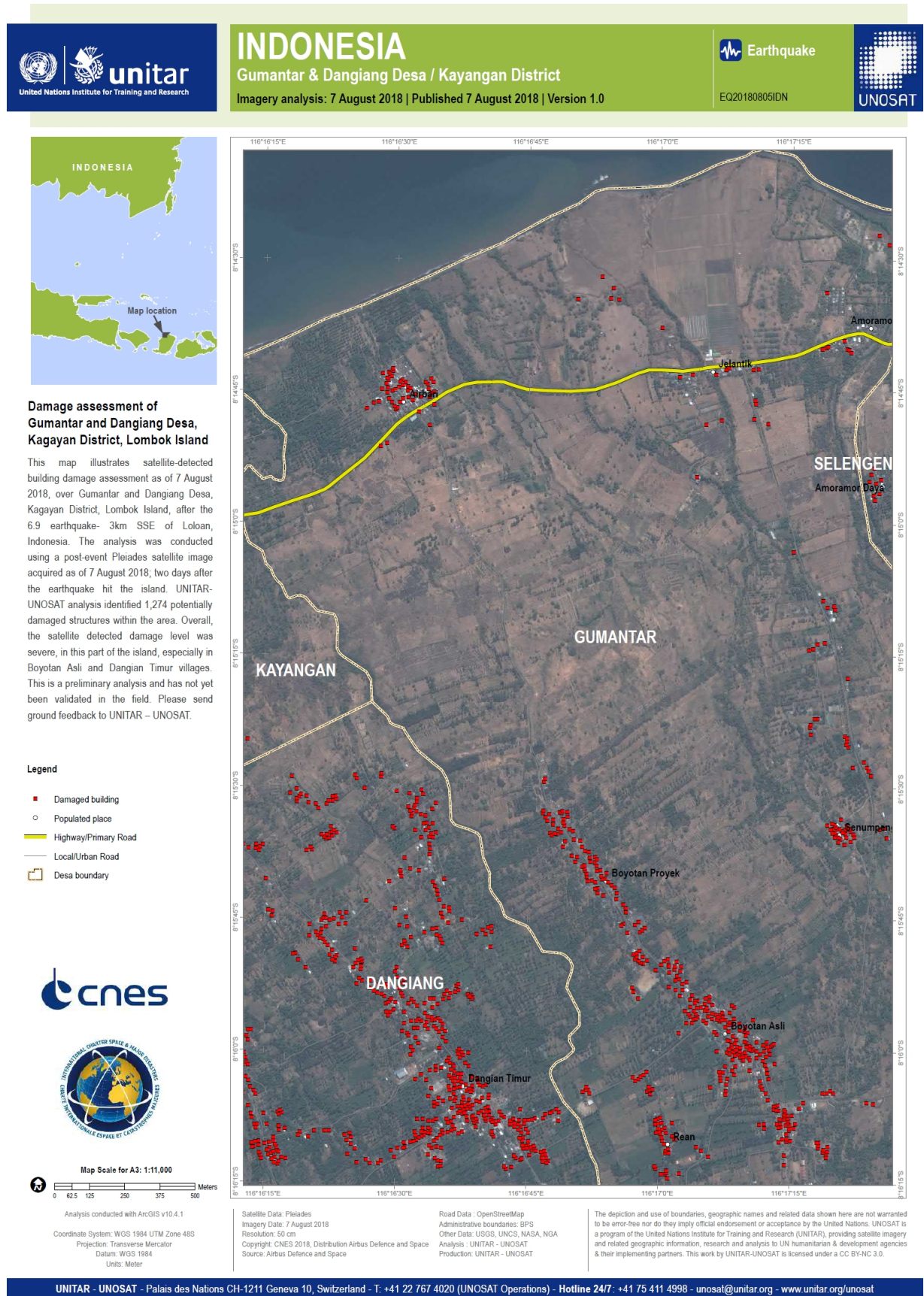


Figure 2.5: Damage assessment map of Gumantar and Dangiing Desa, Kagayan District, Lombok Island, Indonesia after the M6.9 2018 Lombok earthquake. The map has been produced by the UNITAR/UNOSAT team using Pleiades optical data and distributed by the International Charter Space and Major Disasters center (ICMDS).

Optical

Damage maps from spaceborne systems are generated by using either optical or radar instruments. For both systems holds that at a spatial resolution of 10 m. or coarser, earthquake-induced building damage can only be split into several basic damage grades at the (building) block level, whereas moving to meter and sub-meter resolutions allows for detecting damage on the individual building level and precise damage grading (EMS-98 or similar) becomes possible (Dong and Shan [2013]). Optical imagery can be used through either mono-temporal or multi-temporal techniques. Mono-temporal approaches using only post-event imagery mostly consist of visual recognition of damaged elements and is limited to the spatial resolution of the imagery. Hence, if buildings are not clearly recognizable as individual objects in an acquisition it is not suitable for damage detection. However, high spatial resolution imagery (i.e. IKONOS/QuickBird/WorldView) is sometimes freely supplied in disaster response situations by the distinctive organizations, such as during the 2010 Haiti earthquake (Corbane et al. [2011]). Automatic approaches using only post-event data is possible by applying damage detection algorithms such as analyzing anomalies in edges and textures of buildings (Vu et al. [2005]) or by using spectral and textural information to detect damaged buildings (Liu et al. [2004]), but here again very high spatial resolution imagery is needed.

With multi-temporal approaches, manual change detection of optical imagery is still widely used. The detection of building damage is related to changes in the contours of buildings between a (set of) pre-disaster image(s) and a post-disaster image. The multi-temporal approach has an increased set of possible limitations if compared to mono-temporal approaches as a similarity between the set of images in terms of spatial resolution, illumination conditions, clouds or haze, seasonal period, incidence angles, and a minimal temporal gap between the images is preferred. With improving technologies and reduced temporal resolutions (6 days for Sentinel-2) some of these limitations are resolved and by combining data from different optical satellites the time from event to acquisition could be reduced even more. However, due to the dependency on sunlight and surface reflectance there is a low chance of acquiring a usable image when taking into account the day and night rhythm or the amount of cloudcover over the area of interest. Additionally, automatic damage detection is hardly possible due to various issues related to optical data: geometric distortions, improper co-registration, variations in solar illumination, differing off-nadir angle and unrelated changes in the surface (i.e. vegetation, building infrastructure, car traffic) (Stramondo et al. [2006]). Some attempts have been made by exploiting differences between pre- and post-event imagery, subtracted from one another, on color, spectra, texture and other features as done by Pesaresi et al. [2007]. Post classification comparison is based on comparing two independent classification results from pre- and post-event data and assuming that damaged buildings yield a high dissimilarity of edges as compared with intact buildings (Huyck et al. [2005]).

Unfortunately, due to the need of a rather ideal combination of input data for automatic approaches which is rarely available in emergency situations, visual interpretation is still the most often used damage detection approach in rapid disaster response situations. This approach causes the use of optical data to be time-consuming, and therefore drastically increases the response time, one of the key parameters of spaceborne rapid disaster response approaches. Moreover, with manual interaction the response time increases with the extent of the area of interest whereas one of the advantages of satellite imagery is the acquisition of data over a large area. Finally, optical data always depends on weather conditions and once clouds or smoke cover the area of interest none of the aforementioned techniques are applicable, making it unsuitable for reliable rapid damage systems over large areas.

Synthetic Aperture Radar

Satellite Radar imagery is acquired using Synthetic Aperture Radar (SAR) systems. SAR systems use the Doppler Centroid Frequency of multiple acquisitions of the same point in space to process and focus the data. This technique drastically improves the along-track (azimuth) resolution of the imagery. The basic quantity measured by a single-frequency single-polarization SAR system is a pair of signal values in the in-phase and quadrature channels which can be seen as real and imaginary parts of a complex number, as seen in figure 2.6. The raw data coming from the sensor is therefore complex valued and can subsequently be used to compute the intensity and phase information of the backscattered signal through:

$$\text{intensity, power: } I = a^2 = u_{IP}^2 + u_{IQ}^2, \quad (2.1)$$

$$\text{phase: } \phi, \quad (2.2)$$

with I the intensity, a the amplitude, u_{IP} the in-phase channel signal value and u_{IQ} the quadrature channel signal value and ϕ the angle between the horizontal and the line where the two channel signal values meet.

More information regarding SAR systems can be found in Massonnet and Souyris [2008], Moreira et al. [2013] and/or Sarti [2009].

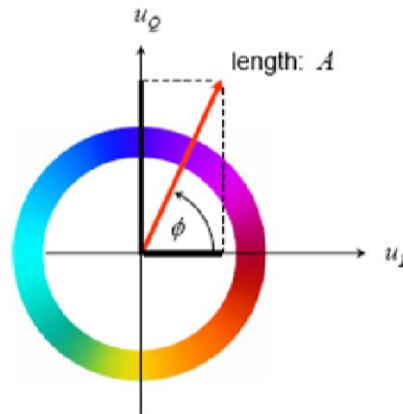


Figure 2.6: Schematic overview of how the in-phase and quadrature channel voltages can be used to compute the intensity and phase information of the complex valued SAR signal Sarti [2009].

The SAR intensity can be related to ground parameters by examining the radar equation, which relates the transmitted and received power by taking in account various influences of the radar system and assumes no dispersion:

$$P_r = \frac{P_t G_A^2 \lambda^2 \sigma_{\text{rcs}}}{(4\pi)^3 R^4}, \quad (2.3)$$

with P_r the received power, P_t the transmitted power, G_A the gain of the Antenna, λ the radar wavelength, σ the radar cross section, or scattering coefficient, of the target and R the range from the satellite to the target. As all of the parameters, except for the radar cross section (σ_{rcs}) and the range (R) are accounted for through internal and external calibration of the radar satellite system, the two remaining parameters can be linked to the intensity and phase. The intensity information represents the backscattered signal intensity of objects (scatterers) contained in each SAR resolution cell and is therefore proportional to the radar cross section of the scatterers/targets:

$$I \sim \sigma_{\text{rcs}}. \quad (2.4)$$

The intensity information is affected by system parameters (i.e., wavelength, frequency, polarization, pulse length, incidence angle, look direction, etc.), surface feature properties (geometrical positions of objects w.r.t. the incoming signal, the target shape and dielectric constant), and environmental variables (e.g., ground water content) (Xia and Henderson [1997]). The phase signal, in its turn, is related to the distance from the satellite to the object:

$$\phi = -\frac{4\pi}{\lambda} R + \phi_{\text{object}}, \quad (2.5)$$

with the radar wavelength as λ , the distance from sensor to the surface as R and the properties of the object affecting the phase as ϕ_{object} . However, this is not an absolute measurement as with other ranging techniques but rather based on the amount of cycles the signal has completed. This feature can only be translated into actual distance measurements when differencing it with another acquisition, where the difference in the amount of completed phases represents the change in distance to the pixel over time. The phase can be related geometrically to elevation differences, motion of reflecting elements on the ground or variations in the propagation velocities in the atmosphere. However, these phase differences can only be observed when the signals in the images are coherent. Decorrelation can arise due to differences in the geometric features, Doppler Centroids, volume of the object, thermal noise of the system, temporal physical changes in the terrain and in the processing steps (Hanssen [2001]). With state-of-the-art satellite missions, decorrelation sources related to the system (differences in baseline, Doppler Centroids, thermal noise and processing errors) have been drastically reduced.

Synthetic Aperture Radar data can be used in different ways to rapidly locate damaged buildings and assist in rescue operations by using either the intensity or phase of the backscattered signal or a combination of the two, as will be discussed in this section. The approaches differ because of the various usages of the SAR signal parameters, the spatial resolution of the SAR satellites used and the length of timeseries that has been analyzed. Next, the various approaches will be discussed and a division between the studies is made based on the SAR parameter(s) that have been used.

Phase The use of the phase in damage detection has resulted in some interesting approaches for rapid disaster response, as the phase information is sensitive to changes in the building shape.

Matsuoka and Yamazaki [2000] used five pre-disaster and one post-disaster JERS/SAR imagery with a 100 km swath and 30 m spatial resolution to perform a damage detection algorithm on the 1995 Kobe earthquake. From this they created and examined four image pairs (two pre-disaster and two co-disaster pairs) which were coregistered, followed by the computation of the complex coherence γ through a 7x7 window (Hanssen [2001], Zebker and Villasenor [1992]):

$$\gamma = \frac{\sum_{i=1}^N z_{1i} z_{2i}^*}{\sqrt{\sum_{i=1}^N |z_{1i}|^2} \sqrt{\sum_{i=1}^N |z_{2i}|^2}}, \quad (2.6)$$

with z_1 and z_2 being the two complex signals of the image pairs, i the sample number and N the amount of signal measurements. The interferometric correlation indicates whether the complex phase signal of the two SAR images is coherent. If the distribution of radar-reflective objects inside a SAR resolution cell is changed between the two acquisitions (i.e. building damage), noise is added to the phase and the coherence is reduced. Matsuoka and Yamazaki [2000] found that an increase in the severity of building damage resulted in a decrease of the magnitude of the coherence $|\gamma|$ due to superficial changes when a building collapses. However, the used image pairs were influenced by either long baselines or a long temporal interval, which both in theory decrease the coherence already and hence may superimpose the effect of decreased coherence due to building damage.

Fielding et al. [2005] have looked at the M6.6 2003 Bam, Iran earthquake using three Envisat SAR acquisitions operated at a 100 km swath and 30m spatial resolution. The imagery has been used to compute the complex coherence for one pre-disaster and one co-disaster image pair, through the approach as shown in equation 2.6. However, they noted that an important aspect of the spatial averaging is that the coherence estimation can be biased downwards by a phase gradient across the averaging window, caused by i.e. co-seismic deformation of the surface (Bürgmann et al. [2000]). Alternatively, reducing the size of the averaging window would reduce the effect of phase gradients as well but this results in a tendency of overestimating the coherence (Bürgmann et al. [2000], Hoen and Zebker [2000]). That is why Fielding et al. [2005] proposed to also calculate the coherence from the phase variance σ_ϕ^2 , which can be computed by first deramping the region (removing a local ramp or phase trend) and then measuring the variance of the phase in the region. Then, the coherence can be computed through phase-sigma correlation, which is the interferometric correlation computed from the standard deviation of the phase, σ_ϕ , and they are related through (Rodriguez and Martin [1992] Rosen et al. [2000]):

$$\sigma_\phi = \frac{1}{\sqrt{2N}} \sqrt{\frac{1-\gamma^2}{\gamma^2}}. \quad (2.7)$$

Here, N is the number of samples. Rewriting and isolating γ results in:

$$\gamma^2 = \frac{1}{2\sigma_\phi n + 1}. \quad (2.8)$$

The effect of a long baseline in the image pairs was visible through the enlarged topographic component but this could be removed using the 3-arc sec Shuttle Radar Topography Mission (SRTM) Digital Elevation Model (DEM) (Rosen et al. [1996]). For the computation of the coherence through phase-sigma correlation a 5x5 window has been applied in order to produce 120m cells. They then subtracted the pre-disaster image pair from the co-disaster one to get a correlation difference map that indicates changes in coherence. This approach makes it possible to separate correlation decrease due to vegetation (or other effects) from earthquake damage. The 100% destruction of structures in the densely populated old parts of the city resulted in coherence changes of -0.7 to -0.3.

An automated approach was illustrated by **Hoffmann [2007]**, again applying it on the M6.6 2003 Bam earthquake and computing the coherence from Envisat imagery through equation 2.6 and a 4x20 window, resulting in 80x80m pixels on the ground. Using five acquisitions, Hoffmann [2007] was able to create one pre-disaster and three co-disaster image pairs. In this way the influence of different temporal and perpendicular baselines on the damage detection results could be studied. The induced effect by longer perpendicular baselines has been minimized by common-bandwidth filtering Gatelli et al. [1994]. Next, for each co-disaster pair the coherence change index ρ was calculated through:

$$\rho = \frac{\gamma_{\text{ref}}}{\gamma_{\text{eq}}}, \quad (2.9)$$

with γ_{ref} being the pre-disaster coherence and γ_{eq} being the co-disaster coherence spanning the earthquake. This coherence change index leads to a high value in areas of high-damage levels and lower values with less damage. However, as the coherence index, like the coherence itself, can only be interpreted meaningfully at a lower resolution and because it may be more useful if results are analyzed over administrative boundaries in rescue operations, the coherence index is averaged for segments of different sizes:

$$\bar{\rho} = \frac{1}{N} \sum_{i=1}^N \min(\rho_i, 3), \quad (2.10)$$

where N is the number of image pixels contained in the segment. The thresholding to values below 3 in the averaging was included to limit the effect of very high values at individual locations on the average, which is supposed to represent an average damage for a larger area. These averaged coherence indexes were then thresholded to classify different damage levels:

Average coherence index range	Damage level class
$\rho < 1.5$	No Damage
$1.5 \leq \rho < 2.0$	Light Damage
$2.0 \leq \rho < 2.5$	Significant Damage
$\rho \geq 2.5$	Severe Damage

Table 2.1: Damage class definitions for the coherence change index ρ as used by Hoffmann [2007].

Close agreement between regions of the highest damage levels in the coherence index images and the severe damage apparent in the IKONOS optical image for all three co-disaster pairs expresses the operability of this approach. The indifference of the damage detection results for the three co-disaster pairs illustrates the usage of common-bandwidth filtering for the different perpendicular baselines and the lack of coherence changes due to different temporal baselines. Note that the common-bandwidth filtering applied here worked due to the Bam area being reasonably flat. Also, for the sake of avoiding under- or overestimation of the estimated damage and thus improved results it is favorable to take a pre-disaster image pair with a short temporal baseline and match a co-disaster image pair with a similar sized temporal baseline but still as quickly acquired after the disaster as possible.

Last, **Yun et al. [2015]** looked at the M7.8 2015 Nepal earthquake using COSMO-SkyMed and ALOS-2 data, respectively having spatial resolutions of 3m and 10m. They used a total of three SAR acquisitions to create one pre-disaster and one co-disaster coherence map by using equation 2.6 and applying a 3x3 window, after topographic phase was removed using the 1-arc sec SRTM DEM. The coherence maps were adjusted to remove estimation bias, registered to each other by calculating dense subpixel offsets, matched in image statistics through histogram matching and finally subtracted from each other and color coded to create a Damage Proxy Map. Good agreement between the DPM and independent analyses by other groups (National Geospatial-Intelligence Agency and United Nations Operational Satellite Applications Programme) has been found. This approach has been applied during the Christchurch earthquake (2011), the L'Aquila earthquake (2016) and the Mexico City earthquake (2017) (figure 2.7).

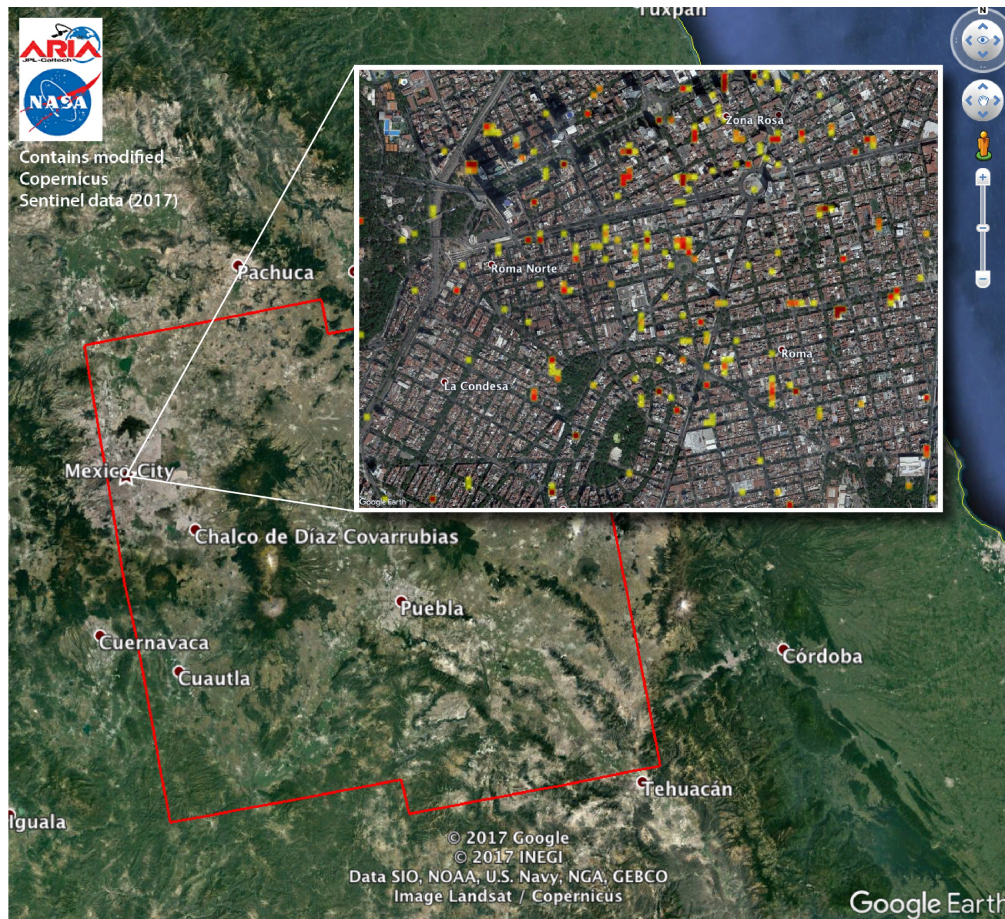


Figure 2.7: Damage Proxy Map derived from Sentinel-1 SAR data for the area of Mexico City after the 2017 M7.1 Raboso earthquake (Brackman [2017]).

Intensity Other studies have examined the operability of the amplitude of the backscattered signal. Although the phase approach is more sensitive to building damage than the intensity approach, the backscattering coefficient provided by the amplitude in its turn is less dependent on the need for similar satellite geometry, acquisition duration or radar wavelength conditions. Contrary to using the phase, the amplitude can be used in mono-temporal damage detection by identifying discontinuities in edges of buildings that could be singled out in the SAR acquisition (Balz and Liao [2010]). Most of these attempts require manual interpretation, which is a time-consuming operation. Hence, by using only post-disaster SAR data, the damage detection approach would not benefit from the automatic approaches possible with SAR data which are key in reducing the time period from data acquisition to damage map.

Polli et al. [2010] attempted to build an automated system to classify building damage levels through a texture-based classifier using post-disaster COSMO-SkyMed images of the L'Aquila (2006) and Haiti (2010) earthquakes. Unfortunately, the results were unsatisfactory as the correlation between the texture-based measures and the block-averaged damage levels was found to weak. In general, damaged buildings do not encompass a distinct scattering signature whereas a collapsed building might still produce a signal comparable to that of an undamaged structure (Dong and Shan [2013]).

In multitemporal approaches, **Matsuoka and Yamazaki [2004]** used four pre-disaster and five post-event European Remote Sensing (ERS) satellite images (100km swath width and 30m resolution) to examine and monitor the backscattered signal for the 1995 Kobe earthquake. Two indications of changed pixels were calculated, the correlation coefficient and the difference. The correlation coefficient, r , between two intensity images, a and b , was calculated within a 13x13 corresponding window as follows:

$$r = \frac{N \sum_{i=1}^N I a_i I b_i - \sum_{i=1}^N I a_i \sum_{i=1}^N I b_i}{\sqrt{(N \sum_{i=1}^N I a_i^2 - (\sum_{i=1}^N I a_i)^2) * (N \sum_{i=1}^N I b_i^2 - (\sum_{i=1}^N I b_i)^2)}}, \quad (2.11)$$

where i is the sample number, $I a_i$ and $I b_i$ are the intensity values as calculated through equation 2.1 for images a and b and N is the total number of pixels within a small window over which the correlations were computed. The difference was computed by averaging over a 13x13 window through:

$$d = 10 * \log_{10} \bar{I} a_i - 10 * \log_{10} \bar{I} b_i, \quad (2.12)$$

where i is the sample number and $\bar{I} a_i$ and $\bar{I} b_i$ are the corresponding averaged backscatter coefficients over the surrounding pixels of pixel i with a small window. From these two indicators a regression discriminant score could be calculated that would result in a distinction between a damaged and non-damaged building based on the two parameters, for all images with respect to a pre-disaster image. Relative good agreement between this approach and field survey data of the Architectural Institute of Japan and the City Planning Institute of Japan was found after applying a Lee-speckle reduction filter on the images.

This same approach has been further examined and applied to the M8.0 August 15 2007 Peru earthquake by **Matsuoka and Estrada [2012]**, using pre- (July 12, 2007) and post-disaster (August 27, 2007) L-band ALOS/PALSAR imagery. Although the spatial resolution of this dataset is higher compared to ERS, 10m vs. 30m respectively, the optimal window size was again 13x13 pixels. Following, by using a damage estimation model acquired by the Japan-Peru Center for Earthquake Engineering and Disaster Mitigation group, a regression discriminant function could be calculated that accounts for the urban structure, the building type and the damage situation in Peru and spatial resolution of ALOS/PALSAR. The regression discriminant function links the discriminant score Z_{Rp} to the calculated difference d and correlation coefficient r . For Peru this function was:

$$Z_{Rp} = -0.089d - 2.576r. \quad (2.13)$$

Next, likelihood functions are formed for each damage rank that provide the probability of being in a damage rank based on the discriminant score. Because these likelihood functions of some damage ranks cross in regions with low discriminant scores, normalized likelihood functions have been computed in which the sum of the likelihood of all damage ranks becomes 1.0. These normalized likelihood functions can then be used to give an indication of the severe damage ratio of an urban area based on the discriminant score calculated from difference and correlation coefficient values from a co-disaster intensity image pair. By incorporating seismic intensity data even higher accuracies for the estimation of the distribution of severely damaged regions could be acquired. When a new earthquake strikes in Peru, this model could be used for damage assessment. This, however, demonstrates the disadvantage of this approach as for each region with

different urban structures, building types or damage situations such an analysis should have been performed prior to a new earthquake, meaning it will not be operable in a rapid response situation.

Another approach was demonstrated by **Stramondo et al. [2006]** for the M7.4 1999 Izmit and M6.5 2003 Bam earthquakes. In the former case study two pairs (one pre- and one post-disaster) with very short temporal baselines of the ERS tandem mission were used, whereas for the latter case study a total of three (two pre- and one post-disaster) ENVISAT SAR images were used, all with a spatial resolution of 4x20 m. In order to partially reduce speckle noise, the images have been multi-looked through a 5x1 averaging window leading to a SAR intensity image of 20x20m resolution (Li and Goldstein [1990]). Next the intensity correlation between a co-disaster pair can be computed through equation 2.11 and the estimations are based on an averaging window size of 7x7 pixels, leading to 140x140m resolution. For the Izmit case, comparing the change detection results from intensity correlation and the complex coherence as explained in equation 2.6 to optical data showed that intensity correlation alone produces better results than complex coherence. When comparing the SAR products to independent ground truth information, which represents the amount of collapsed buildings to the total amount of buildings in a block, interesting results were obtained by using the differenced image between pre- and co-disaster intensity correlation image pairs. For the Bam case study, again the intensity differencing and intensity correlation differencing showed significant results when comparing it to ground truth data of the International Centre for Geohazards, although the sensitivity was lower than with the Izmit case study.

The intensity values have also been used to detect changes in areas of conflict, for example in Homs, Syria during the Syrian civil war by **Tapete and Cigna [2016]**. They used three Sentinel-1 IW and three TerraSAR-X SM acquisitions to perform change detection on and showed the additional improvement of increased spatial resolution. The intensity values have been spatially averaged with a 5x1 and 3x3 filter for both missions, respectively. From these multi-looked intensity values Red-Green-Blue composites could be computed where areas of no change can be observed as grey and changes in one of the acquisitions can be observed as the colour related to that acquisition. However, the interpretation of these results is still done manually and thus not benefiting the automation possibilities related to the use of SAR imagery.

Intensity and Phase The combination of the two parameters of a SAR signal in rapid damage detection has also been exploited, as the phase and amplitude are sensitive to different effects and may therefore be complementary.

Matsuoka and Yamazaki [2000] studied the M7.4 1999 Kocaeli earthquake using three pre- and one post-disaster ERS acquisitions. They calculated the intensity difference (equation 2.12), intensity correlation (equation 2.11) and coherence (equation 2.6) for the image pair temporally closest to the disaster and compared the results to damage ratios of buildings in the city-block level from AIJ data. They found the intensity difference can identify large surface changes, the intensity correlation is sensitive to a wide range of Earth's surface changes while the degree of coherence is sensitive to only slight surface changes. Subsequently, they proposed a procedure to indicate damage levels by thresholding the various SAR products, with coherence to distinguish damaged from non-damaged, intensity difference to detect slight damage and intensity correlation for heavily damaged building blocks. These results showed relatively good agreement with the several damage survey reports.

The same products have been examined by **Gamba et al. [2007]** for the 2003 Bam earthquake using Envisat data. Additionally, they used the coherence of a pre-disaster pair to compare the co-disaster coherence values to and they looked at the original (non-filtered) intensity values. They found, by comparing change detection results to ground truth data, that better results were obtained using the intensity rather than the phase features. Moreover, the best results were obtained by using the pre- and post-disaster intensity values alone. Incorporating ancillary data resulted in even more accurate damage detection results, however this is unfortunately not always available.

Last, **Arciniegas et al. [2007]** again used ENVISAT SAR data for the 2003 Bam earthquake to look at coherence values and changes in the amplitude signal. Contrary to Gamba et al. [2007], Arciniegas et al. [2007] concluded that amplitude values both increased and decreased for various damage levels and therefore showed less conclusive results than the coherence, although the accuracy was low for both. However, the combination of both properties resulted in better damage-extraction results than the use of each separately.

Review All in all, the studies discussed here have illustrated that by using the phase or the amplitude signal individually or a combination of both, building damage can be detected. The studies have been summarized in table 4.1 for clarity. Unfortunately though, none of the approaches presented here have showed an indubitable method that should be used in rapid disaster response situations. First, this is caused by the fact that almost all approaches require some sort of spatial averaging or filtering and thus result in poor spatial resolutions. This hampers the possibility of individual building damage detection, hence the majority of the studies discussed above focussed on damage detection on the building block level. Furthermore, all studies except for Yun et al. [2015] have been completed *ex postfactum* meaning that they were not applied in an operational base. All of these limitations can be overcome by making use of a high-resolution SAR system that has a short revisit time. This would result in the requirement for rapid damage assessment that data can be made available to rescue workers quickly after the disaster. Additional issues for an operational disaster management system that must be addressed are the need to get data quickly, process it in a timely way, and rapidly transfer usable products to the appropriate authorities. Regarding the data processing itself it would be favorable to use an approach that minimizes the amount of spatial filtering needed so that individual building damage can still be detected. This decreases the likelihood of using the phase for damage detection as here spatial averaging needs to be applied to minimize the coherence bias. Moreover, almost all classifications for change detection algorithms are based on bi- or tri-temporal change detection. It would therefore be interesting to see how change detection approaches on long multi-temporal SAR time series could improve damage detection approaches in rapid disaster response situations.

	Choice of Parameter	Spatial Res. [m]	Acquisitions Used [#]	Δt Event-Post [days]	Δt Pre-Post [days]
Matsuoka and Yamazaki [2000]	Phase	150	6	20	352
Fielding et al. [2005]	Phase	120	5	12	35
Hoffmann [2007]	Phase	80	5	12	35
Yun et al. [2015]	Phase	12, 36	3, 3	4, 7	156, 70
Polli et al. [2010]	Intensity	84	1	1	-
Matsuoka and Yamazaki [2004]	Intensity	30	9	126	223
Matsuoka and Estrada [2012]	Intensity	390	2	14	46
Stramondo et al. [2006]	Intensity	140	4, 3	30, 12	35
Tapete and Cigna [2016]	Intensity	60-100, 9-15	3, 3	-	-
Matsuoka and Yamazaki [2000]	Both	60	3	31	35
Gamba et al. [2007]	Both	390	3	12	35
Arciniegas et al. [2007]	Both	100	3	12	35

Table 2.2: Overview of the various studies discussed in this section on SAR parameter used, spatial resolution of the SAR imagery for analysis, amount of acquisitions used, temporal difference from disaster to first available post-disaster acquisition and temporal difference from pre- to post-disaster acquisition (if applicable). For Yun et al. [2015], Stramondo et al. [2006] and Tapete and Cigna [2016], double values for some of the parameters are given. Yun et al. [2015] and Tapete and Cigna [2016] used and compared data from two different satellite systems: Cosmo-SkyMed & ALOS-2 and Sentinel-1 & TerraSAR-X, respectively, whereas Stramondo et al. [2006] used data from two satellite systems (ERS and Envisat, same spatial and resolution) on two case studies: M7.4 1999 Izmit earthquake and M6.5 2003 Bam earthquake.

Review of Spaceborne Approaches

The main advantage of SAR over optical data is that the SAR system is an active sensor and therefore not depending on Sun illumination. Additionally, the signal wavelength is generally long enough to not be significantly affected by clouds or haze. This means that the first acquisition in normal conditions is directly usable for damage detection. In most cases, SAR data of the crisis area is therefore earlier available than cloud free optical data (Plank [2014]). However, the radar signal is more complex compared to optical data and requires a similar acquisition geometry, i.e. single sensor with specific polarization between two acquisitions in order to compare them. The latter drawback can be minimized by having a high revisit time of the satellite constellation. This would lead to a short time frame between the first post- and last pre-disaster acquisition. Additionally, a higher revisit time results in a higher probability of an acquisition close to the moment of the event. This, in its turn favors a rapid response because with spaceborne imagery one is dependent of the moment of the next overpass of the satellite. Other parameters of the satellite constellation that are of great importance in rapid disaster response are spatial resolution, signal wavelength and the swath width. Table 2.3 shows a recap of the advantages and disadvantages of optical versus SAR satellite imagery in a rapid response situation.

	Pro	Con
Optical	Easy to interpret High spatial/temporal resolution Combination of various satellite imagery possible	Dependent of weather High spatial resolution required Hard to combine various resolutions No automation possible Usually not freely available
SAR	Independent of weather Automation possible Reasonable temporal/spatial resolution Sentinel-1 provides free dataset	Hard to interpret Well designed algorithm required No combination of different satellites

Table 2.3: Comparison between the advantages and disadvantages of satellite-based optical and SAR sensors in rapid disaster response situations.

Table 2.4 shows an overview of currently active SAR satellites and some of their parameters. Based on this overview it can be noted that the Sentinel-1 mission has a very large swath width and reasonable revisit time at the cost of spatial resolution, with respect to the other satellite systems. This limits the application of damage assessment to the block level (encompassing several buildings per block) or reasonable sized buildings (Plank [2014]). In terms of wavelength, L-band would be most favorable in rapid disaster response after earthquakes as this wavelength is unaffected by smaller scale processes whereas the signal of interest is caused by the collapsing of buildings and/or building blocks. The returning signal would therefore mainly be affected by the changes in geometry of the collapsed buildings. The C-band of Sentinel-1 is in this case the second best option for this purpose. However, the most important feature of the Sentinel-1 mission is the global coverage and open-data policy that ESA provides, as depicted in figure 2.8. This is contrary to all other missions, where imagery needs to be ordered and no global time-series is available which can be exploited for rapid disaster response after a humanitarian crisis where the location is unknown on beforehand. Therefore the Sentinel-1 mission will be the main data source in this research, in order to detect building damage caused by earthquakes and intentional damage during warfare. The following section will give a more detailed overview of the Sentinel-1 mission.

Mission (Number of satellites)	Period -	Band (λ [cm])	Swath [km]	Spatial Res. [m]	Revisit Time [days]
ALOS-2 (1)	2014-	L (23.6)	70	6	14
Radarsat-2 (1)	2007-	C (5.6)	100	25	24
TerraSAR-X (2)	2007-	X (3.1)	30	3	11
Cosmo-Skymed (4)	2007-	X (3.1)	40	10	4
Sentinel-1 (2)	2014-	C (5.6)	250	3x22	6

Table 2.4: Current radar satellite missions and their characteristics: time since start, wavelength, swath width and resolutions for stripmap mode or similar and the revisit time of the satellite mission (Van Leijen [2014]).

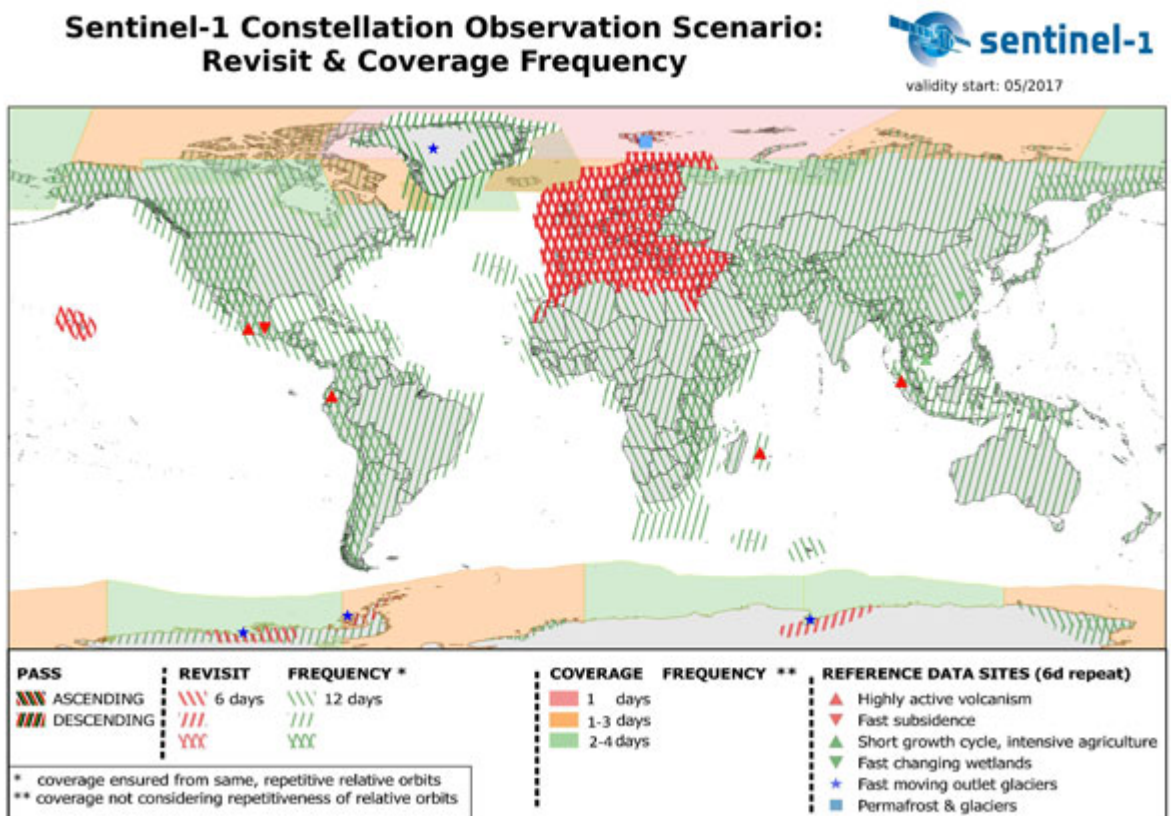


Figure 2.8: Sentinel-1 Constellation revisit and coverage frequency. The highest possible acquisition frequency is performed over Europe and Hawaii whereas both ascending and descending orbits are operated over seismic active areas (Suhet [2013]).

2.4. The Sentinel-1 Mission

The Sentinel-1 mission is the first of five missions that the European Space Agency (ESA) has developed for the Copernicus joint initiative between the European Commission (EC) and ESA. The goal of the Sentinel-1 satellites is to continue the C-band SAR Earth Observation heritage of the European Space Agency's ERS-1, ERS-2 and ENVISAT, and Canada's RADARSAT-1 and RADARSAT-2. Sentinel-1 also provides enhancements over previous missions in the form of reliability, revisit time, geographical coverage and rapid data dissemination (Torres et al. [2012]). The high temporal resolution is especially of importance during rapid response in emergency situations such as floods, earthquakes, volcanic eruptions and landslides, as well as bombings in conflict areas as the imagery should be acquired as quickly as possible after the disaster and the chance of this revisit right after an event increases with a higher temporal resolution.

The enhancement in revisit time has been accomplished by a combination of two factors. First, the Sentinel-1 mission makes use of the Terrain Observation with Progressive Scans SAR (TOPSAR) technique, resulting in a large footprint while maintaining a relatively high spectral resolution (figure 2.9). Second, the Sentinel-1 mission consists out of two satellites which will individually provide radar images every twelve days, disregarding the weather or time of the day. These satellites, Sentinel-1a and Sentinel-1b, share the same orbital plane with 180° orbital phasing difference, so that with the launch of Sentinel-1b the combined temporal resolution has been reduced to 6 days (Yagüe-Martínez et al. [2016]).

The satellites make use of a C-band Synthetic Aperture Radar, which has a wavelength of 5.8 cm. The SAR instrument will allow dual and single polarization. Additionally, Sentinel-1 is able to switch between four different observation modes: Strip Map (SM), Interferometric Wide Swath (IW), Extra-Wide Swath Mode (EW) and Wave-Mode (WV) which all have their specific way of taking radar measurements. This results in different footprints and spatial resolutions, as shown in figure 2.10 (Torres et al. [2012]). WV will be the main acquisition mode for open oceans and IW over land, EW is used for coastal and polar areas and SM is only used in emergency situations or calibration. IW and SM mode are the most promising for the rapid disaster response and are therefore explained in detail below.

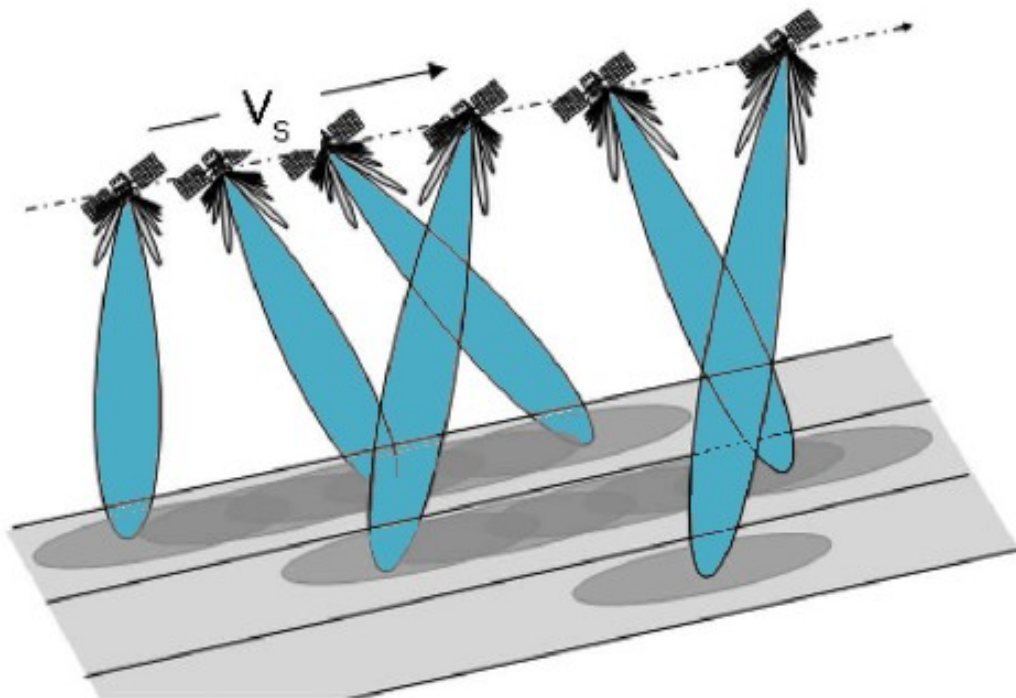


Figure 2.9: Schematic overview of the TOPSAR technique in IW mode. The antenna beam is cyclically switched between 3 adjacent sub-swaths, whereas for each sub-swath the radar antenna is rotated from backward to forward in azimuth direction (Suhet [2013]).

SM mode is implemented to continue the measurements of ERS and ENVISAT missions. It provides a narrow swath width of 80 km, where the imaging swath can be selected by changing the beam incidence angle, and has a spatial resolution of 5 x 5 m. Unfortunately, this mode is only used in exceptional cases and cannot be used for long timeseries analysis in rapid disaster response. The IW mode is the default acquisition mode over land and has a large swath width of 250 km with a moderate spatial resolution of 5 x 20 m (Torres et al. [2012]). This large footprint while maintaining moderate spatial resolution is achieved by applying the aforementioned TOPSAR technique (2.9). The TOPSAR observation mode is an improvement of the ScanSAR technique. During data acquisition with the TOPSAR mode the radar antenna beam is rotated from backward to forward in the azimuth direction in a single sub swath. Compared to SM mode, data from a much longer strip will be obtained in the same amount of time, allowing the antenna to also be steered in range direction to scan a total of 3 sub swaths in IW mode (De Zan and Guarneri [2006]). This results in a total swath width of 250 km compared to 80 km in SM mode, at the cost of spatial resolution: 5 x 20 m for IW mode and 5 x 5 m for SM mode.

Although SM is a mode especially designed for use in emergency situations, it is not suitable as a data source in this research. The reason is that SM mode is only used for a very limited amount of observations. This is contrary to what is required for the creation of damage detection maps; a continuity in data in order to create a time series of the same area with acquisitions as close to the moment of the earthquake as possible. Therefore, the Sentinel-1 data used in this research has been obtained in IW mode, which is the standard acquisition mode over land and hence provides a consistent data flow. In order to determine the usefulness of the Sentinel-1 data in rapid disaster response situations, the data latency due to ESA processing has been determined. By checking the difference in time between the end position of an acquisition and the ingestion date of the data in the open portal one can calculate the time between acquisition and availability. To create a trustworthy average of the data latency the average difference between data acquisition and availability for all Sentinel-1 acquisitions of the past two months has been calculated, resulting in an average difference of 5 hours and 30 minutes. This is way below the restriction ESA has put on the data availability of 24 hours and shows that this satellite mission, operated by ESA, is not restricted on data latency due to downlinking and preprocessing on ESA's side for rapid disaster response. The usage of SAR data in rapid response situations as well as the usability of Sentinel-1 data in the Google Earth Engine in terms of damage detection is discussed in the next chapter.

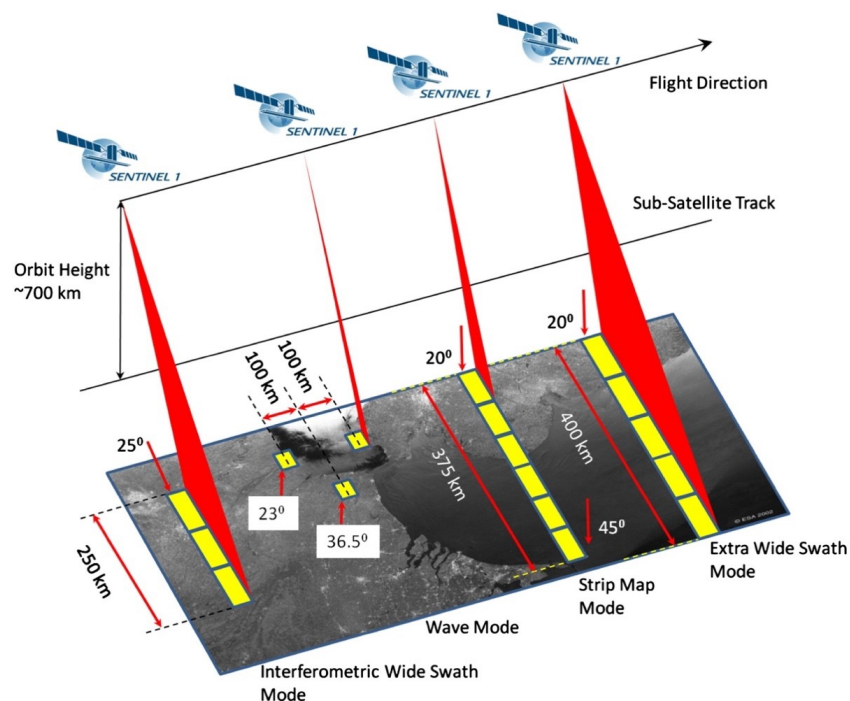


Figure 2.10: Schematic overview of the various observation modes of the Sentinel-1 mission. From left to right they are: Interferometric Wideswath Mode (IW), Wave Mode (WV), Strip Map Mode (SM) and Extra Wide Swath Mode (EW) (Suhet [2013]).

3

Methodology

This chapter will describe the processing software which has been used in order to process the Sentinel-1 data in this research: the Google Earth Engine (EE). EE is used in this research to develop and operate the damage detection algorithm as it contains the entire Sentinel-1 GRD imagecollection, which can be quickly accessed and processed to a damage detection map. The algorithm development process is also described in this chapter on a step-by-step base.

3.1. Google Earth Engine

The Google Earth Engine is a cloud-based platform for petabyte-scale scientific analysis and visualization of geospatial datasets, both for public benefit and for business and government users Google [2017]. The Earth Engine (EE) allows this data availability by storing satellite imagery, organizing it, and making it available for global-scale data mining. The public data archive includes Earth imagery going back more than 40 years and new imagery that is collected on a day-to-day basis. Additionally, it grants access to various imagery (optical and radar), geophysical, climatological, meteorological and demographic datasets. Some examples include the entire (USGS/NASA) Landsat catalog, MODIS datasets, precipitation data, elevation data, sea surface temperature, U.S. National Agriculture Imagery Program (NAIP), CHIRPS climate data and above all: Sentinel-1 GRD imagery. All of the input datasets have been preprocessed and georeferenced.

The processing is performed on Google's infrastructure, which allows for fast and efficient computations. The EE automatically parallelizes data analyses in order to run them simultaneously on many CPUs located at Google's data centers. Furthermore, the computed results are cached so that multiple requests for the same data do not result in recomputation, increasing the efficiency even more. This network in its turn allows for processing planetary-scale computations with multiple datasets and algorithms. Note that the results may be evaluated in a commercial or operational environment but use is not allowed for sustained production use, and data products generated by the EE may not be sold. Because the EE is free of use for research, education, governmental and non-profit use, there is an ever-growing community who use the system to analyze large scale geospatial data. This results in quick improvement of the engine and fast development of new algorithms which may or may not be shared with the public.

The two main drivers to use the Google Earth Engine for this research are:

- **Unprecedented Speed**
The cloud-based processing in the GEE reduces the time used for geospatial analyses of large areas significantly, which is one of the largest bottlenecks in rapid disaster response.
- **Easy accessible and open access**
The easy processing and visualization of data in the IDE results in quickly analyzing of results. The petabyte-sized data archive which is provided in the GEE can be combined for algorithm development and improvement.

Data analysis can be done through the Application Programming Interface (API) in both JavaScript and Python, whereas EE also provides other tools. The API supports complex geospatial analyses including: overlay, map algebra, array operations, image processing, classification, change detection, time series analysis, joins,

raster-vector conversions, vector-based extraction of image statistics etcetera. The Integrated Development Environment (IDE) is designed for rapid prototyping and visualization of complex spatial analyses. In the IDE, scripts can easily be saved and opened and the results nicely displayed for quick analysis. As the IDE (JavaScript) offers a map to easily scan through the data which makes it easy to use for non-remote sensing specialists and it is available online it is used for most of the processing done in this research. The IDE is depicted in figure 3.1.

The online code editor contains several important features which make it rather easy to use, run and share the code. First of all, there is a searchbar at the top which allows you to easily search for datasets and places, show the details of that particular result and lets the user import them in the script when needed.

Secondly, there are three boxes in the top that all have specific functions. The top-left box is related to the coding and contains tabs with a script manager, API documentation and an asset manager. The script manager (*Scripts* tab) contains all of your personal scripts as well as shared and example scripts in Git repositories hosted by Google. This Git system also allows you to modify scripts outside of the EE or sync them with an external system. The *Docs* tab refers to the JavaScript API documentation used in the programming. Lastly, the *Assets* tab refers to the asset manager which allows the user to upload and manage personal image assets in the EE. The top-center box is used for the actual coding with buttons to save, run or get a link to the script. The top-right box is focused on the results with an *Inspector*, *Console*, *Tasks* and a *Profiler* tab. With the *Inspector* tab opened the user can analyse values and information of the layers covering a certain point on the map. In this case it is very useful to inspect timeseries of a certain feature on the map, such as a predefined damaged building. The *Console* outputs information on printed objects such as imagecollections as well as error messages generated by the code. When a part of the code takes to much time to process and therefore gets timed out, a user can export it as a task. Additionally, when an intermediate or end result is needed for processing out of the EE it can be exported. Both of these type of tasks will appear in the *Tasks* manager which allows the user to choose the size, resolution and format of the product after which it shows the progress of exportation. Lastly, the *Profiler* provides information on the duration and CPU load of the running of the code. When inspecting these values one has a better idea of the performance and possible room for improvement of the code.

Last, The *Map* in the lower half automatically loads imagery and features that have been requested to project in the code. It allows to switch between a schematic and a representational base layer, provides a layer manager to select and adjust projected layers and has geometry tools to manage and create geometries. Panning over images goes very smoothly as the processing within the EE determines which tiles of the entire image are within the shown area and therefore only represents those. Additionally, zooming in/out causes pixels to be resampled, reducing the amount of pixels needed for visualization. More information on the processing and the possibilities the EE offers is discussed in Gorelick et al. [2017] and Google [2017].

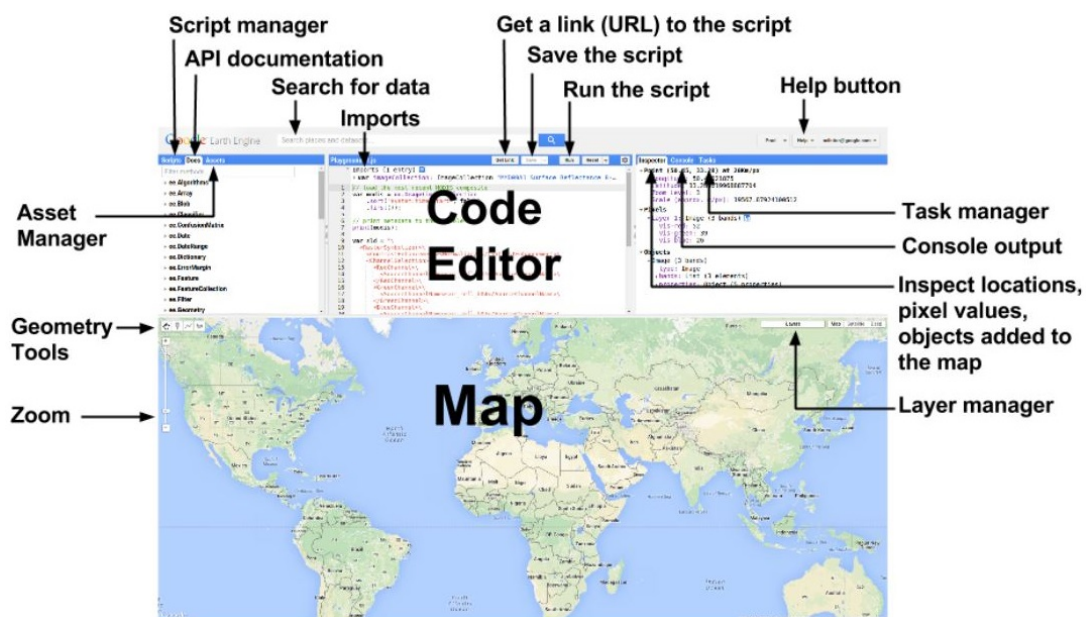


Figure 3.1: Overview of the web-based IDE for the EE JavaScript API.

3.2. Sentinel-1 Data

The main dataset used for this research is the RADAR data acquired by the Sentinel-1 mission and made available in the EE. However, to get from the acquisition of the radar signal to the final calibrated, ortho-rectified GRD product in EE, processing steps are applied by both ESA and EE itself. These steps will be discussed in this section.

3.2.1. ESA Processing

Sentinel-1 data makes use of the TOPSAR mode for Earth observation, which acquires data in bursts for three sub-swaths. The raw data (level-0) is transformed and focused to a level-1 product (Single Look Complex (SLC) or Ground Range Detected (GRD)) through calibration and the application of various algorithms, as indicated in figure 3.2. Compared to the SLC format, the GRD scenes have been detected, multi-looked and projected to ground range using an Earth ellipsoid model such as WGS84. For GRD products, the bursts are concatenated and sub-swaths are merged to form one image. The bursts overlap minimally in azimuth and sub-swaths overlap minimally in range. Bursts for all beams have been resampled to a common grid during azimuth post-processing. In the range direction, for each line in all sub-swaths with the same time tag, the adjacent sub-swaths are merged. The overlapping region in range, is merged along the optimal sub-swath cut, which is defined from the Noise Equivalent Sigma Zero (NESZ) profiles between two sub-swaths. If the two NESZ profiles intersect inside the overlapping region, the position of the intersection point is the optimal cut. The ellipsoid projection is corrected using the terrain height of the satellite, which varies in azimuth but is constant in range. Due to this ground projection all phase information is lost and the pixel values only represent intensity values. The resulting product has approximate square pixels with reduced speckle at the cost of reduced geometric resolution (Suhet [2013]).

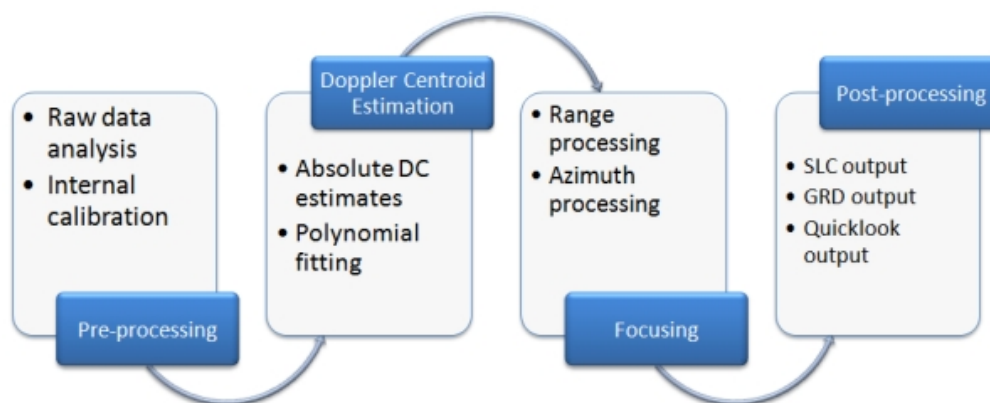


Figure 3.2: Processing flow of the raw radar data as observed by the Sentinel-1 mission to level-1 products Suhet [2013].

For converting digital pixel values to radiometrically calibrated backscatter, all the required information is distributed through Look-Up Tables (LUTs). A calibration vector is included as an annotation in the product allowing conversion of image intensity values into sigma, beta or gamma nought values. Further details on the calibration of the GRD intensity values can be found in subsection 3.2.2. The ellipsoid projection in GRD products is corrected using the terrain height of the satellite, which varies in azimuth but is constant in range. Due to this ground projection all phase information is lost and the pixel values only represent intensity values. The resulting product has approximate square pixels with reduced speckle at the cost of reduced geometric resolution (Suhet [2013]). This final GRD dataformat is then distributed through the SciHub and also made available to EE's pipeline.

3.2.2. EE processing

Earth Engine (EE) offers the entire dataset of Sentinel-1 images in Ground-Range Detected (GRD) format. EE uses the following preprocessing steps (as implemented by the Sentinel-1 Toolbox) to derive the backscatter coefficient in each pixel:

1. Apply orbit file (using restituted orbits)
2. GRD border noise removal
3. Thermal noise removal
4. Radiometric calibration
5. Terrain correction (ortho-rectification)
6. Archive implementation

1. Apply Orbit File

In SAR processing, changes in geometry and topography can induce significant differences in the observed signal. Therefore as a first step restituted orbit files are applied to the GRD file. This orbit file contains information on the orbital position of the satellite at the moment of acquisition and adjust for it. Precise orbital information contains even more accurate positional information compared to the restituted orbital information, but as the precise orbits generally take one week to be determined versus 1 day for restituted orbits the latter are favoured. Furthermore, because the Sentinel-1 mission follows an orbital tube with a rms of only 50m the restituted orbits are of sufficient quality to perform the correction. This is the first step in order to compare and combine GRD imagery.

2. Border Noise Removal

Border noise in Level-1 products is expressed as no-data and pixels with very low values at the cross-track and along-track borders. These artefacts are introduced in the generation of Level-1 products from RAW Level-0 data. More specifically, the artefacts appear mainly during the azimuth and range compression and its subsequent handling of the sampling window start time, being the time offset between the start time of the transmitted pulse and the start time of the current received sampling window (Ali et al. [2018]). This step is needed to compensate for the change in the Earth's curvature. The removal of this noise is easy in SLC products as dedicated information is provided for each burst, however for GRD products the masking is not straightforward due to the ground range detection of the data. In order to remove this noise in the GRD imagery, the "Sentinel-1 Remove GRD Border Noise" step in the SNAP toolbox is applied, which detects and masks these invalid data and low intensity pixels by applying denoising vectors on the co-polarisation channel (HH or VV). The choice to use it on the co- instead of the cross-polarisation channel is due to a higher signal-to-noise ratio for the co-polarisation channel. More extensive explanation of the "Sentinel-1 Remove GRD Border Noise" step in the SNAP toolbox can be found in Collecte Localisation Satellites [2016].

3. Thermal Noise Removal

Thermal noise in the returned signal is noise caused by microscopic motions of electrons due to an increased temperature. This heat is mostly provided by the internal circuitry of the satellite and the emissivity of the Earth's surface. As this thermal noise can have a significant effect, in particular when imaging dark targets, it is favourable to remove these effects. The thermal noise contribution is estimated in slant range coordinates by first calculating the range spreading loss vector, followed by the correction for the elevation beam pattern after which the scalar contributing factors are applied (ESA [2016]). See Piantanida et al. [2017] for more information on the thermal denoising of Sentinel-1 products. The range varying shape is of importance as the noise can be different between swaths, causing an intensity step at swath boundaries. These thermal noise vectors are then converted to ground range coordinates and saved to an annotation data set provided by ESA (Bourbigot [2016]). The thermal noise removal step uses these thermal noise vectors to apply a correction by subtracting the noise from the power, in each image. This causes objects that typically have a very low backscattering effect, such as water bodies and certain types of vegetation, to actually possess low amplitude values.

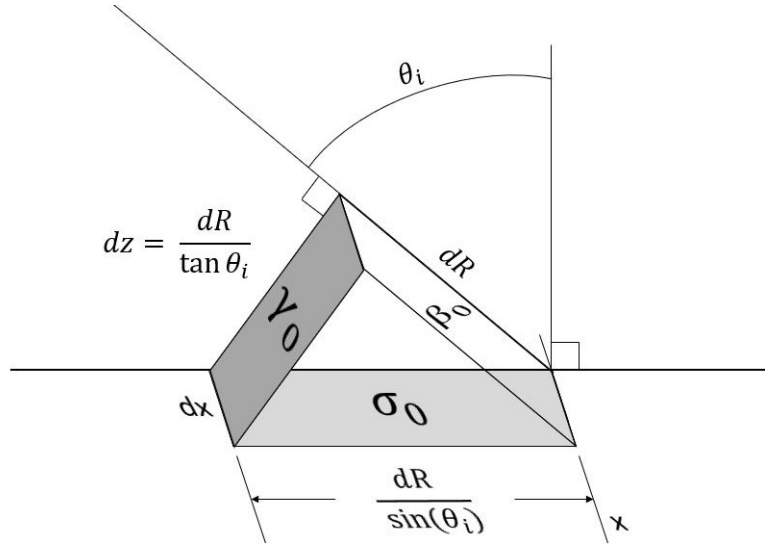


Figure 3.3: Schematic illustration of the various backscatter scalings: β_0 , σ_0 and γ_0 including the conversion equations from β_0 . θ_i represents the local incidence angle (Raney [1998]).

4. Radiometric Calibration

To make time series comparable, radiometric calibration is applied. This results in imagery of which the pixel values can directly be related to the radar backscatter of the scene (ESA [2016]). The radiometric calibration uses one of the four provided Look-Up Tables (LUTs) to undo the application output scaling applied by the processor and apply the desired scaling. The various scaling factors related to their geometry are shown in figure 3.3. These LUTs are used to produce β_{0_i} , σ_{0_i} and γ_{0_i} values (Bourbigot [2016]). Here, β_0 resembles the returned backscatter from a distributed scatterer on the ground in slant-range coordinates (radar brightness). As slant-range pixels cover different areas on the ground which vary with the local incidence angle (looking geometry and Digital Elevation Model (DEM)), it comprises a geometric impact on the backscatter signal. σ_0 is the backscatter returned to the antenna from a unit area on the ground. By using a DEM in the viewing geometry of the satellite during the acquisition, the original pixel values can be converted in order to minimize the effect of topography on the backscattering signal. Last, γ_0 represents the backscatter per unit area of the incident wavefront, which is perpendicular to slant-range. Here again the local incidence angle is used to compute γ_0 from the DN or β_0 . The LUTs apply a range-dependent gain including the absolute calibration constant. For GRD products additionally a constant offset is applied. The actual radiometric calibration is applied through (Bourbigot [2016]):

$$V(i) = \frac{|DN_i|^2}{A_i^2}, \quad (3.1)$$

where, depending on the selected output the $V(i)$ is one of β_{0_i} , σ_{0_i} or γ_{0_i} and A_i is the calibration scaling factor for one of the desired outputs. When a pixel falls between points defined in the LUT, bi-linear interpolation is applied. Note that due to this calibration, the thermal noise vectors also have to be scaled to the chosen output. The noise calibration is done as follows (Bourbigot [2016]):

$$n(i) = \frac{\eta_i}{A_i}, \quad (3.2)$$

where $n(i)$ is the calibrated noise profile for one of β_{0_i} , σ_{0_i} , γ_{0_i} or *OriginalDN*_{*i*}. η_i is the *noiseLUT*(*i*) and A_i is again one of the scaling factors. Once the calibrated noise profile has been obtained it can be removed from the GRD dataset. As the desired output within the EE is σ_0 , for all variables the noise vectors relating to *sigmaNought*(*i*) have been used.

5. Ortho-rectification

Ortho-rectification, or Terrain Correction, is the last post-processing step within the Sentinel-1 toolbox that is applied. Terrain correction converts data from slant-range, which does not take terrain into account, to ground range geometry using the acquisition geometry of the satellite and the SRTM 30 meter DEM or the 90 meter ASTER DEM for high latitudes (greater than 60° or less than -60° latitude). By simulating a SAR image based on the local incidence angle, effects such as foreshortening and layover can be simulated and then identified in the original GRD file with the use of Ground Control Points (GCPs). Hence, the pixels of the GRD image can be reshaped using bilinear interpolation to their real, geographical location. This radargrammetric approach allows for a better integration with Geo-Information Systems (GIS) or digital maps, such as the EE. Terrain correction is needed when comparing imagery obtained with different incidence angles or when spatial differences are of interest. Note that this step is embedded in the EE processing of Sentinel-1 GRD data and redundant in the change-detection approach discussed in this research as this step is needed for comparing spatially separated pixel values but not needed for pixel timeseries analysis.

6. Archive Implementation

Finally, post-processing steps are applied using Numpy in Python in order to make the images suitable for implementation in the EE. First, the unitless backscatter coefficient is converted to dB in order to retrieve an evenly distributed value range from the non-gaussian distributed values through:

$$\sigma_0(\text{dB}) = 10 * \log(\sigma_0(\text{power})). \quad (3.3)$$

Note that this conversion is only applied to the general COPERNICUS/S1_GRD imagecollection, but not to the daily updated COPERNICUS/S1_GRD_FLOAT imagecollection which will be used in the approach developed in this research.

Next, pixel values are clamped to the 1st and 99th percentile to preserve the dynamic range against anomalous outliers, and quantized to 16 bits to allow fast processing. Clipping usually results in a cut-off at 0 dB and since values > 0 dB are generally caused by man made structures, clamping them will lose less valuable information, as compared to not using clamping and having large tails of very high and very low values which would have reduced the amount of information available for biomass or water detection. When frames are scaled on the 1% and 99% quantiles, it matters how many pixels in a scene are in these extreme quantiles. So, if scenes include some urban areas, the quantiles > 0 dB tend to be small, and everything gets clamped. Over extended mountainous areas, where large quantiles can be > 0 dB, positive dB values are retained meaning that the 0 dB cut-off is variable. This naturally causes limitations in the processing algorithm, as urban structures are objects of interest in rapid disaster response. However, because the GRD files have been multi-looked compared to the SLC format the returned signal is a mixture of various objects within the pixel. Hence, strong reflectors are leveled out by weaker reflectors within the same pixel.

It should be mentioned that developers of the EE are changing the processing pipeline so that the pixel values do not get clipped any more as well as quantizing the values in 32-bits, thus increasing the accuracy (Ilyushchenko [2018]). Depending on how fast the ESA uploads the newly acquired images to the Scientific Data Hub (SciHub), the EE provides a daily updated dataset of the Sentinel-1 GRD images in near-real time (Google [2016]). The EE developers restricted the data latency from the moment an acquisition is made available by ESA to it being post-processed and ingested in the EE to a maximum of two days. This generally is completed faster than this restriction of 48 hours, however no statistics are available, according to Ilyushchenko [2018].

Final Product

The final Sentinel-1 GRD collection contains all of the GRD scenes and is updated daily. Each scene has one of three resolutions (10, 25 or 40 meters), four band combinations (corresponding to scene polarization) and one of three instrument modes (IW, EW, SM). The possible polarization combinations are single band VV or HH, and dual band VV+VH and HH+HV. Each scene also includes an additional 'angle' band that contains the approximate viewing incidence angle in degrees at every point. For IW mode the GRD files are provided with a multi-look factor of 5x1 (High Resolution, 4.4 Equivalent Number of Looks (ENL)) and 22x5 (Medium Resolution, 81.8 ENL). In terms of resolution this results in a pixel spacing of 10x10m and a spatial resolution of 20x22m for high resolution and 40x40m pixel spacing and 88x87m spatial resolution for medium resolution. For this research the highest spatial resolution is preferred and therefore the high resolution IW mode GRD data will be used. In IW mode only dual band VV+VH is available over the non-polar regions.

3.3. Optical Data

Besides SAR data, the EE also provides optical data. Within this research, optical data is used to classify and mask vegetated and water areas by making use of the Normalized Difference Vegetation Index (NDVI) and the Normalized Difference Water Index (NDWI), as these areas are not of interest for damage detection purposes. The three optical datasets available for this approach are: Sentinel-2, Landsat and MODIS. However, as the optical data will be used to classify non-urban pixels it is beneficial to have a spatial resolution comparable to that of the Sentinel-1 imagery. Because MODIS data has a spatial resolution of 250m it is unfavorable to use this dataset when alternatives such as Sentinel-2 and Landsat are available.

Sentinel-2 is a wide-swath, high-resolution, multi-spectral imaging mission launched as part of the Copernicus initiative of the ESA. Its aim is to monitor vegetation, soil and water cover, as well as to observe inland waterways and coastal areas. The Sentinel-2 data in the EE consists of 13 spectral bands representing Top of Atmosphere (TOA) reflectance scaled by 10000 (Suhet [2015]). In addition, three Quality Assessment (QA) bands are present where one (QA60) is a bitmask band with cloud mask information. This QA band is able to identify dense and cirrus clouds and provides statistical information on the percentage of cloudy pixels in the cloud mask (ESA [2017]). Each Sentinel-2 product (zip archive) may contain multiple granules, whereas each granule becomes a separate Earth Engine asset. The spatial resolution of Sentinel-2 pixels is 10x10m and it has a revisit time of five days under the same viewing geometry (Google [2016]).

The Landsat 8 SR dataset in the EE contains atmospherically corrected surface reflectance imagery from the Landsat 8 OLI/TIRS sensors operated by NASA (NASA [2016]). These images contain five visible and near-infrared (VNIR) bands, two short-wave infrared (SWIR) bands processed to orthorectified surface reflectance and two thermal infrared (TIR) bands processed to orthorectified brightness temperature. The VNIR, SWIR and TIR bands all have a spatial resolution of 30m, where the TIR bands have been resampled from an original 100m spatial resolution. The data has been atmospherically corrected using the Landsat 8 Surface Reflectance Code (LaSRC) (NASA [2017]). It also includes a cloud, shadow, water and snow mask produced using the C Function of Mask algorithm (CFMASK) (Foga et al. [2017]), as well as a per-pixel saturation mask. Landsat data is collected on a nominal 16-day repeat cycle. Strips of collected data are packaged into overlapping "scenes" covering approximately 170x183km, using a standardized reference grid (Google [2017]).

In order to decide which of these two datasets is most useful for classifying non-urban areas by exploiting the NDVI and NDWI, a few qualifications have been determined:

- **Spatial Resolution**
The spatial resolution of the pixels should be as high as possible in order to distinguish the urban pixels.
- **Revisit Time**
It is beneficial to have a high revisit time in order to get the most up-to-date data on urban settlements, however as urban areas generally do not change within a time span of several days it is not of high priority.
- **Cloud Masking**
With optical data, clouds limit the ability to identify targets on the surface. Therefore it is important that a reliable automated cloud detection algorithm can be applied so that clouded pixels are masked.
- **Atmosphere Corrected**
For the best results it is important that the influence of the atmosphere on the received radiance signal has been removed, resulting in surface reflectance.

Comparing the parameters from the Sentinel-2 with Landsat 8 SR datasets provided in the EE, it can be noted that the Sentinel-2 mission is more favorable considering spatial resolution (10 m. vs 30 m.) and revisit time (5 days vs 16 days). However, the Landsat-8 dataset contains a more extensive cloud masking algorithm as well as atmosphere corrected radiance values. Both result in more accurate non-urban area classification results. Additionally, the Landsat dataset is longer than that of the Sentinel-2 mission (April 11 2013 vs June 23 2015) meaning that more historical data is available for use. As the spatial resolution does not differ significantly considering the size of urban areas and the revisit time is not as important as the other qualifications the Landsat-8 SR dataset will be used as optical imagery within this research.

3.4. Damage Detection System

The approach for the change detection algorithm proposed in this research is to use a set of pre-disaster images of the area that contain a “background noise” signal, being variations in the data that have natural causes. This pre-disaster timeseries is then compared to the post-disaster image closest to the moment of the earthquake or intentional damage during warfare in order to keep the influence of additional temporal changes unrelated to the earthquake at a minimum. From the approaches based on the (combination of) amplitude and/or phase of a SAR system that can be used in rapid disaster response situations as discussed in section 2.3.3, the proposed approach presented in this research is based on the amplitude, or the backscatter intensity, of an object as this is the only parameter in the Sentinel-1 dataset that is provided by the EE.

In order to successfully process the amplitude time series for damage detection and thus maximize the correct detection of collapsed structures, three parameters need to be determined. First parameter is the polarization of the signal, where VV, HH, VV+VH and HH+VH are available. Also, the length of the pre-seismic set should be correctly determined as a reliably long period should be used in order to calculate a correct average, minimizing the influence of outliers. However, the set should also not start too far back in time as additional variations, such as construction and/or demolition or previous earthquakes, might disturb the reference signal. Lastly, the threshold used to distinguish a pixel as a collapsed building should be determined carefully. This threshold needs to be area-specific as the size and material of the buildings can influence the backscatter signal significantly. However, it can be assumed that buildings generally give a constant reflection of the radar signal in the temporal domain, so that a significant change in the σ_0 value of an urban pixel is likely to be caused by a change in the geometric shape of the building. The goal of the entire damage detection approach is to use a common change detection algorithm regardless of the area, but does result in individual thresholds to properly detect damage. It should also automatically select the correct data for an area in a way it can be operated by non-remote sensing specialists.

3.4.1. Data Selection

In order to successfully run the algorithm for a certain area, there are three different parameters which need to be set: dates, location and relative orbit numbers. The date of the earthquake needs to be set after which the algorithm should automatically isolates the last pre-disaster and the first post-disaster acquisitions from the entire timeseries. The total timeseries for each situation runs from January 1 2015 until the most recent acquisition, as January 1 2015 is the beginning of the Sentinel-1 mission and hence results in a significant long timeseries. This date can be moved more towards the present if, for example, the area of interest has already been struck by an earthquake during sentinel-1 data acquisition. For the location only a point of interest is required as input, most likely to be the epicenter of an earthquake or the center of a conflict area. A buffer with a certain distance (currently 150km) is introduced to this point to create an area of interest (AOI) to which the change detection algorithm is applied and changed pixels are identified. The relative orbit numbers of the Sentinel-1 tracks are used to create timeseries of the AOI only from imagery acquired under similar geometric conditions. These orbit numbers are automatically extracted from the most recent post-disaster acquisition that is available in both ascending and descending orbit but can also be manually given as input if the most recent acquisition does not cover the area of interest sufficiently.

General Selection Parameters

To get to the required dataset, the available set of Sentinel-1 GRD images in the EE needs to be filtered on date, area, polarization, instrument mode and resolution in order to further specify it. A significantly long time period is used that includes pre-seismic and the first co-seismic image available whereas the area is the polygon computed from the point of interest given as input. As explained in section 2.4, IW mode has the most desirable combination of parameters from the available modes in Sentinel-1 acquisition: being a reasonable spatial resolution of 20x5m in azimuth and range, a continuous temporal record of every 6 days and a swath width of 250km. For this application the highest possible resolution for the GRD images is selected, resulting in 20x20m pixels. Last, the polarization that is used is VV: a vertically polarized transmitted and received signal. Although several studies have pointed out that using HH polarization gives the most accurate results in detecting Persistent Scatters (PS) (Parizzi et al. [2016], Pipia et al. [2009], Navarro-Sanchez and Lopez-Sanchez [2012]), generally being man-made structures in urban areas (Usai [1997], Usai and Hanssen [1997]), HH polarization is not usable in the current research as the Sentinel-1 satellites only acquire HH polarization over the polar areas. The available polarizations are VV and VH and as Parizzi et al. [2016] pointed out, VV polarization is favored to be used in urban areas.

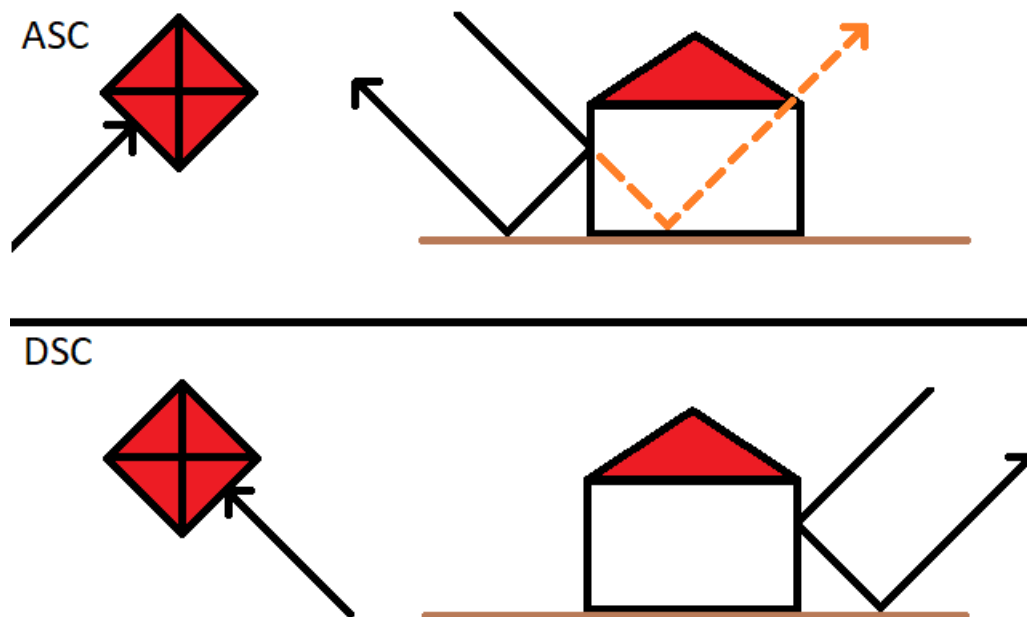


Figure 3.4: A schematic and simplified overview of the difference in backscattering signal of the same building in ascending and descending orbits. On the left the top view of the building with incoming radar signals (top: ascending, down: descending) is shown. The right-hand side shows the side view of the same building whereas in the ascending situation we are looking in the north-west direction and in the descending situation in the north-east direction. In the case the south-west wall and (part of) the roof collapse, the ascending signal will encounter a change in backscattering signal (top-right, orange arrow) whereas the descending signal will stay largely unchanged.

Next, the dataset is split into ascending and descending orbits using the relative orbit numbers extracted from the post-disaster acquisition. The need to split the imagecollection in the two orbit directions is due to the relation between looking angle and building geometry. As an example, say that in an area struck by an earthquake a north-west south-east orientated building is located where only the wall on the east side of the building collapsed. The stack of ascending images will show a massive change in the returned radar signal as the main reflector in that pixel has collapsed, whereas in the descending images no massive change will be observed when the other walls and possibly a part of the roof are still intact. This situation is schematically depicted in figure 3.4 for clarity.

When observing changes in non-urban areas, splitting the imagecollection in two orbit directions would be sufficient as the terrain correction discussed in subsection 3.2 would account for differences in the σ_0 value caused by different incidence angles of parallel relative orbits. However, due to the complex scattering of the radar signal in urban areas the terrain correction based on the 30m SRTM DEM will not be sufficient. Hence, splitting the timeseries based on ascending and descending orbits alone will not suffice and the relative orbit numbers are needed to only select acquisitions with the same incidence angles. As in some cases multiple acquisitions of the same relative orbit cover the AOI, images with similar dates are mosaicked together to create one image within the imagecollection for each date covering the AOI. Each orbit direction timeseries is then split into pre-disaster and post-disaster image selections by using the disaster date given as input. Both pre- and post-disaster imagery are clipped to the AOI and if it includes a coastal regions the data can optionally be masked by selecting pixels of which the SRTM dataset has a value that is equal to 0m, which holds for large low-lying water bodies as the no-data value there is set on 0m. It is important to check whether this function affects pixels on land that are within the AOI. This same processing scheme is repeated for the Sentinel-1 dataset with VH polarization which is used in the following processing step.

Correcting Spatially Extensive Effects

The pre-earthquake dataset will be used to determine the natural variation of the σ_0 value per pixel. These variations can be caused by changes in the geometry of the objects in the pixel not related to any seismic events (speckle), changes in the dielectric constant of the objects or the uncertainty in the measurements. However, changes can also be consistent over a large part of the image if, for example, rain occurred. Rain

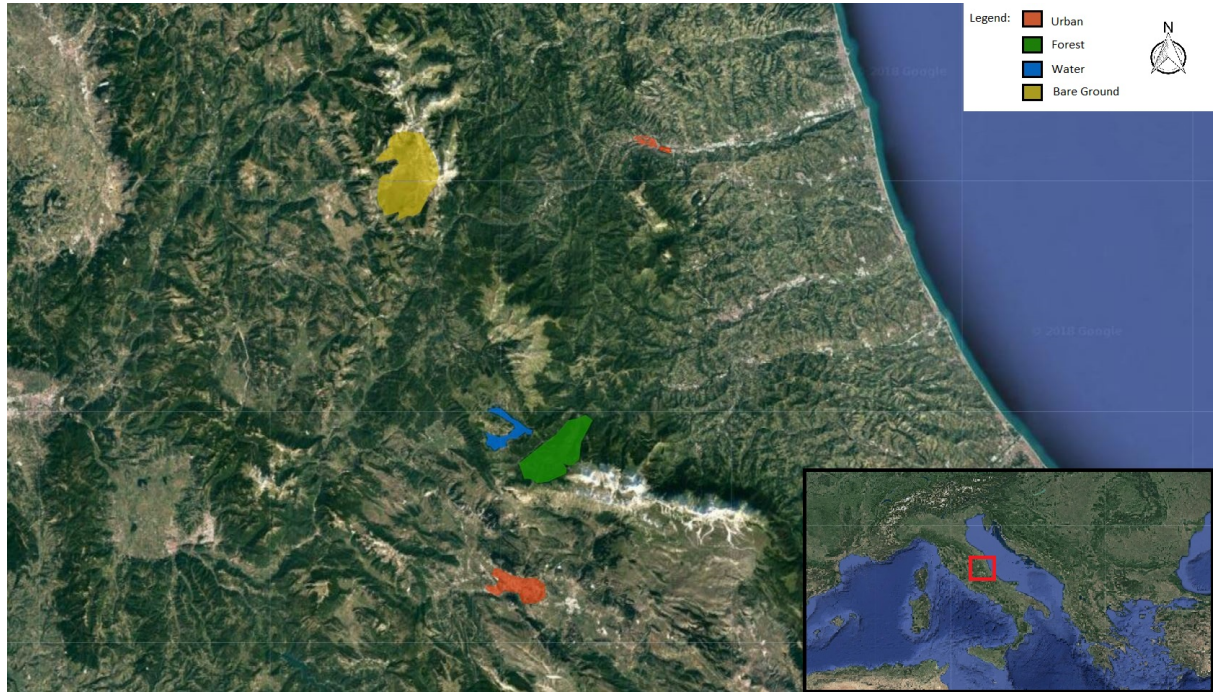


Figure 3.5: Polygons shown here have been used to analyze histograms of pixel values of NDVI, Amplitude Dispersion and σ_0 in VV and VH polarization and ascending and descending orbits.

is an unwanted effect that makes the pre-earthquake signal more variable. To minimize these large spatial effects, each image in the pre-earthquake timeseries is corrected by comparing the values of a collection of stable pixels to the median of the entire timeseries for that group of pixels. This selection of pixels that are assumed to be stable is based on pixels that contain a fairly constant geometrical position such as buildings and mountains without vegetation. The selection of these pixels is completed by using the NDVI from Landsat imagery and Sentinel-1 σ_0 in VH polarization. Before the NDVI of each pixel can be determined, first the Landsat dataset is filtered with the same AOI and length as used for the pre-earthquake Sentinel-1 dataset. Additionally, the Landsat pixels are masked whenever a cloud or the shadow of a cloud is present using the CFMASK function (see section 3.3). Then, for each pixel in every image of the timeseries the NDVI is calculated by using the NIR (band 5, 0.85-0.88 μm) and Red (band 4, 0.64-0.67 μm) bands of the Landsat 8 dataset through (NASA [2016], Ke et al. [2015]):

$$NDVI = \frac{NIR - RED}{NIR + RED}, \quad (3.4)$$

which results in an NDVI value between -1 and +1, where positive values relate to vegetation. To determine the thresholds to correctly identify pixels with a fairly constant geometrical structure, pixel values of four different geographical groups have been analyzed: Urban areas, Water, Forest and Bare Ground in the area around L'Aquila, Italy (see figure 3.5). The Urban group is the main focus of this selection and thresholds for various parameters have been compared to isolate these spatially distributed pixels.

Besides the NDVI and σ_{0VH} in ascending and descending orbit, the σ_{0VV} in both directions as well as the normalized amplitude dispersion of σ_{0VH} and σ_{0VV} in ascending and descending orbits have been observed. The normalized amplitude dispersion per pixel is calculated through:

$$D_A = \frac{\sigma_A}{\mu_A}, \quad (3.5)$$

where D_A represents the normalized amplitude dispersion, being a measure of the temporal variability of the amplitude signal of a pixel, σ_A the standard deviation of σ_0 in time and μ_A the mean of σ_0 . For the NDVI the maximum value over a one-year timeseries is used whereas for the σ_{0VV} and σ_{0VH} timeseries the mean is computed and analyzed. To determine the correct threshold in order to isolate the urban pixels the histograms of specific statistics of these five parameters over the four geographical classes have been compared. By analyzing the spatial histograms of these parameters for each geographical class, eventually a

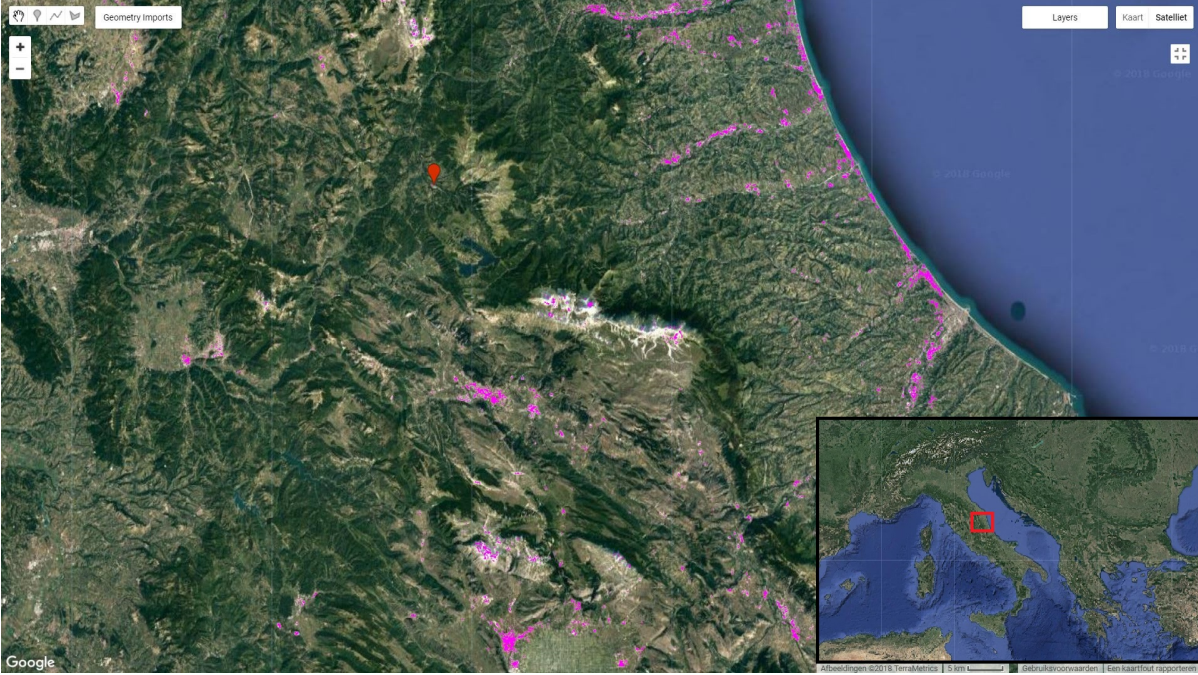


Figure 3.6: Pixels masked with the purple color have been identified as stable pixels based on the thresholds discussed in this chapter.

mask has been computed which uses the aforementioned combination of the highest observed NDVI value and the highest observed amplitude value of $\sigma_{0_{VH}}$ for each pixel. The threshold for the NDVI is that the maximum value in the timeseries should be lower than 0.4, as this would indicate that during the year the pixel is not covered by a significant amount of vegetation. Each pixel should also have a maximum σ_0 value of the radar signal higher than 0.3 in both ascending and descending orbit. By setting this threshold this high water is being left out because water has a very low σ_0 value due to most of the radar signal is reflected away from the sensor due to its smooth surface. By applying this threshold on both orbit directions also a significant part of mountainous pixels are disregarded, as mountainous areas usually are highly reflective in only one orbit direction. Applying these thresholds on the area of L'Aquila results in the selection of pixels shown in figure 3.6, which mostly indicate urban areas with only a few selected pixels over mountainous areas. The selection therefore performs well for indicating urban areas, unfortunately no confusion matrix has been generated to more specifically validate the selection algorithm.

By using the selection of pixels as presented in figure 3.6, each image in the timeseries can be corrected for large spatial effects. This correction consists of three parts where first a reference value for each selected pixel, being the median of the timeseries, is being divided by the σ_0 value of that same pixel pix of an acquisition n :

$$F_{n,pix} = \frac{\tilde{\sigma}_{0_{pix}}}{\sigma_{0_{n,pix}}}, \quad (3.6)$$

where $F_{n,pix}$ is the ratio per selected pixel for each image, $\tilde{\sigma}_{0_{pix}}$ is the reference value for that selected pixel (the median of the timeseries) and $\sigma_{0_{n,pix}}$ the amplitude pixel value for each selected pixel in a specific acquisition. Secondly, the median value of the ratio of all pixels is calculated in order to reduce the local effect of outliers and calculate a correction factor for the entire image. In the case only a part of the image is significantly changed by a certain effect the effect of the correction is evened out by this approach. If the median of the ratio of all pixels in an image is lower than 1 it means that most part of the image has a higher σ_0 value compared to the median of the timeseries and when the median ratio is higher than 1 this averaged value is lower compared to that median. As a third and last step, the specific acquisition is multiplied with this correction factor in order to correct the entire image:

$$\sigma_{0,corij} = \sigma_{0_{ij}} * \tilde{F}_n, \quad (3.7)$$

where $\sigma_{0,corij}$ represents the corrected σ_0 value of each pixel in an acquisition, $\sigma_{0_{ij}}$ the original amplitude value in an acquisition and \tilde{F}_n the correction factor for the entire image computed from the median of the

various ratios. What results is a timeseries containing images that have been corrected for large spatial effects that affect a large part of the image.

Unfortunately, this step could not be incorporated in the final operational damage detection algorithm. The amount of processing power required to perform this step caused the calculation to be timed out by the EE, as every user has a limit on the amount of processing power one is allowed to use. This could be avoided by asking permission from the EE developers to exceed this user limit, but still the time it takes to perform this step limits the application of the final damage detection algorithm in rapid response situations. Therefore, the possible added effect on improved damage detection does not way up to the need for quick damage detection map generation which is key for this operational approach. Fortunately, the damage detection still shows prospective results for various case studies as shown in section ??.

Expectation of Heterogeneous Surface in Medium Resolution Observations

If this correction would be applied, remaining temporal changes in the corrected timeseries have been caused by small-scale effects, such as: changes in dielectric constant and changes in the geometry of objects within a pixel. It is expected that these "natural" effects have a smaller effect on the σ_0 value of an urban pixel compared to the collapsing of a building or structure within that same pixel. By splitting the timeseries in a pre- and post-disaster part, the background noise of a pixel can be evaluated and compared to the effect the disaster had on a building and thus the σ_0 value. Here, it is important to estimate the backscattering signal of a pixel based on the natural behaviour of that same pixel in the pre-disaster timeseries. Based on the assumptions determined by Madsen [1986] and Bamler and Hartl [1998], Hanssen [2001] already described the derivation of the marginal probability density function (PDF) of the amplitude ($\sigma_0(\text{amp})$) from the PDF of a complex circular Gaussian variable y representing the complex-valued reflectance of the incoming radar signal (Goodman [1975], Davenport and Root Jr [1987]):

$$\text{pdf}(y) = \text{pdf}(\text{Re}(y), \text{Im}(y)) = \frac{1}{\pi 2\sigma^2} \exp\left(-\frac{(\text{Re}(y))^2 + (\text{Im}(y))^2}{2\sigma^2}\right), \quad (3.8)$$

with

$$\sigma^2 = \sigma_y^2 = \sigma_{\text{Re}(y)}^2 = \sigma_{\text{Im}(y)}^2, \quad (3.9)$$

being the variance of the complex circular Gaussian variable. The marginal PDF of the amplitude (a) in the SAR resolution cell can be written as:

$$\text{pdf}(a) = \begin{cases} \frac{a}{2\pi\sigma^2} \exp\left(-\frac{a^2}{2\sigma^2}\right) & \text{for } a \geq 0 \\ 0 & \text{otherwise} \end{cases}. \quad (3.10)$$

This equation resembles the Rayleigh distribution (Papoulis [1968]). Additionally, as the intensity is related to the amplitude through: $I = A^2$, the intensity is described by an exponential function. However, as the GRD scenes have been detected, multi-looked and projected to ground range with respect to the original SLC scenes the backscattering values are altered resulting in the need to account for the applied processing steps. First, Raney [1998] described the effect of averaging of X resolution cells (multilooking) on the PDF of the intensity value as a χ^2 -distributed PDF with $2N$ degrees of freedom:

$$\text{pdf}(p_{2N}) = \frac{p^{X-1}}{E(p)^X \Gamma(X)} \exp\left(-\frac{p}{E(p)}\right). \quad (3.11)$$

So for $X = 1$ this equals to the exponential PDF and for $X \rightarrow \infty$ it equals to a Gaussian PDF (Hanssen [2001]).

However, another issue arises when trying to apply the derivation of the marginal PDF of the amplitude from the PDF of the complex-valued reflectance of the incoming radar signal on the situation described in this research as the first assumption of Madsen [1986] and Bamler and Hartl [1998]:

"No single scatterer should dominate the others in a resolution cell. This assumption generally holds for, e.g. agricultural fields, forests, deserts and many other natural scatters."

does not hold when applying it to urban areas. Bamler and Hartl [1998] noted that the condition is violated if only a few dominant scatters are present in a resolution cell such as artificial objects and urban areas. This is because buildings, infrastructure and vehicles can result in single-, double or triple-bounce reflections and hence an increased backscattering compared to distributed scatters (Perissin and Ferretti [2007]).

In order to determine the temporal distribution of the backscattering signal for an urban pixel in a GRD image the PDF has been derived empirically. First, urban areas were detected with the use of optical imagery and polygons were drawn around them manually (figure 3.7). Then for each acquisition of the pre-disaster timeseries in ascending and descending orbit the σ_0 values for all of the pixels within these polygons were averaged and set as the image value. This resulted in a new timeseries with the mean value of each acquisition for urban areas. From this newly acquired timeseries a histogram was formed which represents the averaged expectation of σ_0 (int) in urban areas, shown in figure 3.8.

The histograms for both ascending and descending orbits show a significant peak around a σ_0 value of ~ 0.5 with a longer tail towards the higher values. The histograms are accompanied by a plot of a log-normal distribution for this dataset and it can be seen that the histograms have the same shape as the log-normal distribution. The more centralized log-normal distribution of the amplitude values compared to the estimation of a Rayleigh distribution for the same amplitude values described in Hanssen [2001] is most likely caused by the effect of multilooking over stable scatters (Raney [1998], Guarnieri [2013]). Moreover, the relatively high amplitude values are caused by the strong backscattering effect of urban areas containing many man-made objects which operate as stable scatterers (Usai [1997], Usai and Hanssen [1997]). The scale parameter of the log-normal distribution is slightly underestimated resulting in a difference between the amount of occurrences per value bin and the PDF. Based on these figures it can be stated that the PDF of the σ_0 value of urban pixels in GRD imagery follows, up to some extent, a log-normal distribution over a short interval of relatively high σ_0 values. This is in line with previous research on the distribution of backscatter values in urban areas. George [1968], Kuruoglu and Zerubia [2004], Kuttikkad and Chellappa [1994], Laur [1989], Szajnowski [1977] and Delignon et al. [1997] have presented the log-normal distribution as the distribution for the intensity values when a resolution cell is dominated by a strong scatterer in a very heterogeneous surface (e.g. urban areas) (Tison et al. [2004]).

Other possible distributions for resolution cells containing a strong scatterer in urban areas are the Rice distribution (or Nakagami-Rice distribution) for intensity values when a resolution cell is dominated by a single scatterer in a homogeneous clutter (Goodman [1975], Dana and Knepp [1986], Argenti et al. [2013], Gao [2010]) and the Fisher distribution for high resolution SAR statistics over urban regions (Tison et al. [2004], Tison et al. [2003], Moser et al. [2006], Nicolas and Anfinson [2002]). The Rician Model is appropriate to describe an image of which the strong scatters are embedded into the surrounding weak clutter environment in the case of low resolution, according to Goodman [1975] and DeVore et al. [2000]. As the GRD imagery is of medium resolution (20x20m) and we are looking at a heterogeneous surface, also based on these descriptions the log-normal distribution is the most plausible distributions for our situation.

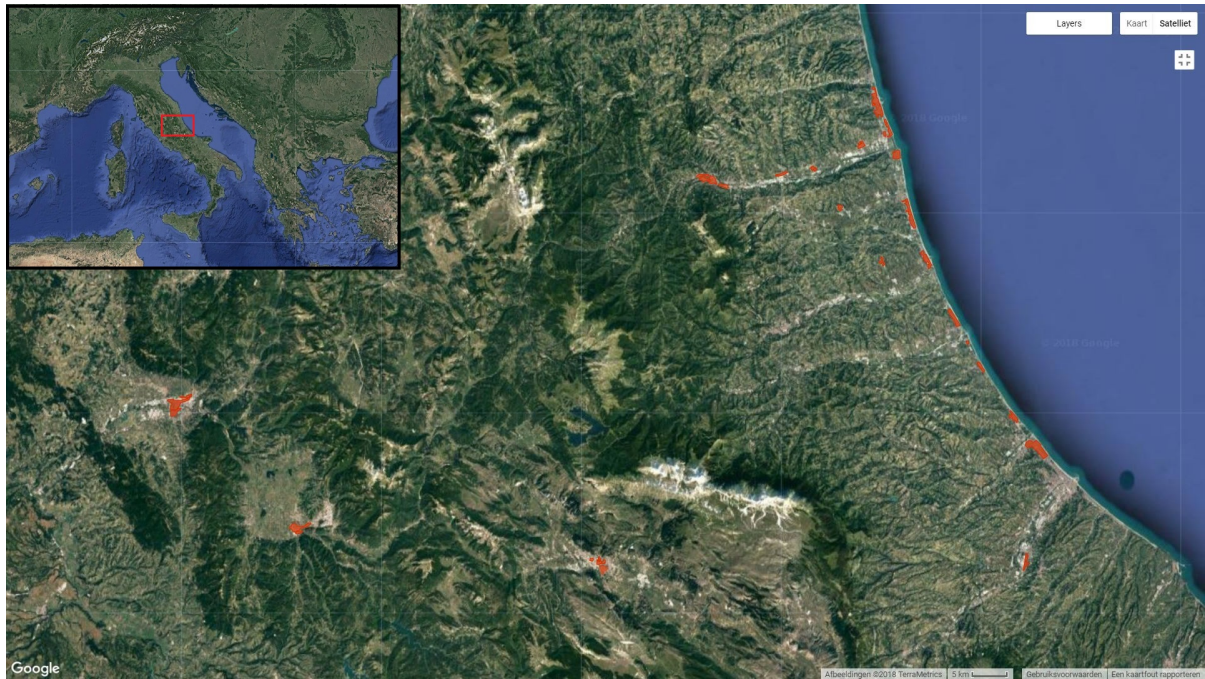


Figure 3.7: Overview of the urban areas that were selected to empirically determine the PDF of the backscattering signal of urban pixel in a GRD image. The red polygons indicate which areas have been selected.

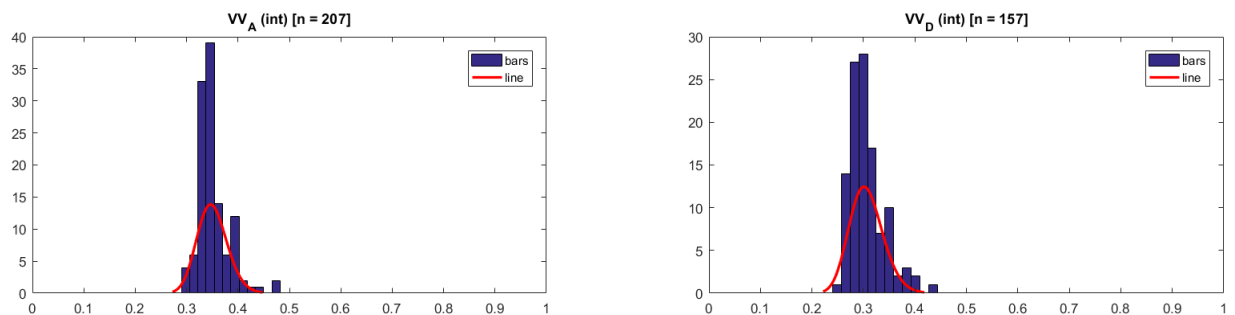


Figure 3.8: Histograms of the spatially averaged timeseries of the backscattering signal in intensity over urban areas in GRD files, based on the pixel selection depicted in figure 3.7. The histogram (blue bins) on the left-hand side represents the VV polarization in the ascending orbit and the histogram on the right-hand side represents the VV polarization in descending orbit. A log-normal distribution has been plotted over the histogram using (red line). It can be seen that the histograms have the same shape as the log-normal distribution but the scale parameter of the log-normal distribution is slightly underestimated resulting in a difference between the amount of occurrences per value bin and the PDF.

3.4.2. Change Detection Algorithm

The final step of the damage-detection algorithm is the change detection itself. The approaches proposed here are based on the assumption that the changes between the most recent pre- and post-disaster acquisitions are caused by the disaster itself. It is thus favorable to take the most recent pre- and post-disaster image as close to the moment of the disaster as possible so that the timespan is kept at a minimum and avoiding effects on the backscattering signal unrelated to the disaster. In order to determine whether the change in the reflection of the surface due to collapsing buildings also significantly alters the backscattering signal σ_0 , three change detection algorithms have been applied and evaluated on accuracy of identifying collapsed buildings.

The first two change detection approaches have been based on the assumption that the collapsing of a building would result in such a significant change in the backscattering intensity, that the value is significantly higher or lower compared to any of the previous intensity values observed in the timeseries. The third and last approach is based on the assumption that the collapsing of a building causes a sudden change in the backscattering intensity of the co-disaster pair that is higher or lower compared to the maximum observed $\Delta\sigma_0$ in the pre-disaster timeseries. Note that whether the collapsing of a building due to a disaster leads to a significant increase or decrease in the σ_0 value of the first post-disaster acquisition depends on the geometry of the building and the way it collapsed, as depicted in figure 3.9.

For validation, the three change detection approaches will be applied to the city of Amatrice that suffered from the M6.2 2016 Central Italy earthquake. To determine the accuracy of the damage detection, the results are also compared with a damage grading map generated by the Copernicus GMES EMS team (see figure 3.16). The grading map is obtained by manually comparing high resolution optical pre- and post-disaster imagery and checked for changes in urban structures and areas of rubble. The final map was generated 7 days after the event happened and shows roads and buildings that have been detected as destroyed (red), highly damaged (dark orange), moderately damaged (light orange) and negligible to slight damage (yellow) for an area of interest (green polygon).

Ideally, the results of the approaches are compared to ground truth data with detailed information on the amount and type of damage in order to determine the significance of a pixel detected as changed compared to the actual status of a building. From here on a confusion matrix could be derived that would indicate the significance of the classification, as depicted in figure 3.1. Unfortunately, this is not available for this case and therefore, the grading map, which has been derived without in situ validation as explained in the disclaimer, is the best available option for the validation. Note that these maps have been generated as a rapid disaster response product and may therefore still contain some errors in the indicated damage classifications and locations. Moreover, the damage classes have been based on manual interpretation of optical satellite imagery meaning that the depth of analysis is limited to the spatial resolution of the satellite system and the nadir view. If a wall collapsed but the roof is still intact, this would be very hard, if not impossible, to detect. The off-nadir radar signal, however, may detect this collapsed wall as a change in the backscattering intensity.

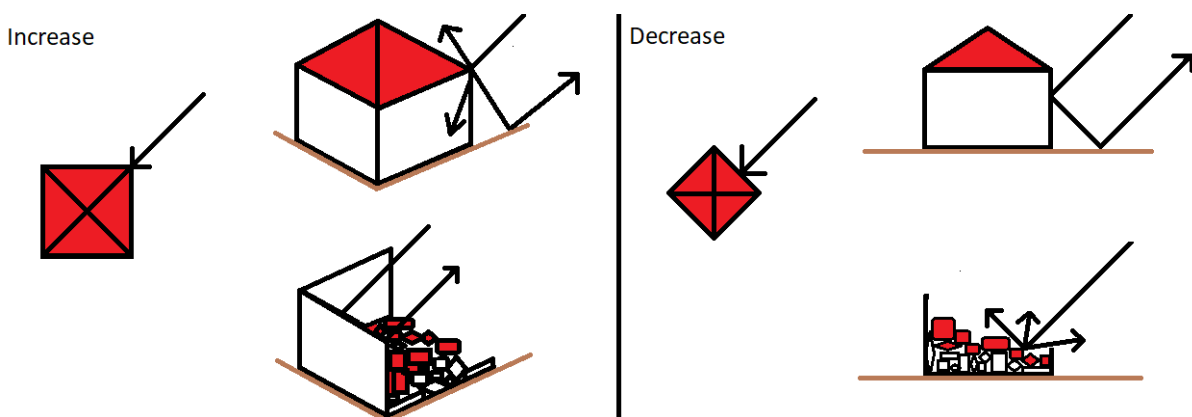


Figure 3.9: A schematic overview of the possible changes in the σ_0 value due to a partly collapsing building. On the left-hand side a situation is illustrated where the incoming radar signal reflects on the corner or side of a building causing the radar signal being reflected away from the satellite (top). Once the north and east wall together with the roof collapse, the remaining walls and ground might form a corner reflector and hence cause an increase in the backscattered signal (bottom). On the right-hand side again an incoming radar signal in ascending orbit is illustrated where now in the normal situation the wall and ground result in a double-bounce (top). Now, when this wall and the roof collapse the radar signal will interact with the debris and scatter, resulting in a decrease of the backscattered signal (bottom).

The three damage detection approaches will be explained in more detail and evaluated on how accurately they detect damaged buildings. The significance of pixels detected as changed is determined by comparing the co-disaster result with a reference result from the same area where no disaster occurred. If an algorithm already detects many pixels in the reference image (false positives), then the added detection due to the disaster might not be as evident and thus not easily interpretable for rescue workers. By comparing the damage detection maps from the three approaches to both the damage grading map and the reference images, the best change detection approach will be selected for implementation in the final damage detection algorithm. Best is defined here as the approach that most optimally detects changes that correspond with actual buildings that collapsed due to the earthquake, hence minimizing the amount of false positives and false negatives. False positives are pixels detected as changed but that do not correspond with damaged buildings, whereas false negatives are pixels that do not have been detected as changed but do overlap with damaged buildings. This is also depicted for clarity in table 3.1.

Actual Value	Detection Outcome	
	Change Detected	No Change Detected
Damaged Building	True Positive	False Negative
No Damaged Building	False Positive	True Negative

Table 3.1: Table showing the confusion matrix for the damage detection approaches.

If the damage detection maps are used as indications of damaged buildings during ASR 1 (see p. 11) in wide area assessment by search and rescue teams and they would only visit the sites indicated on the map, a false negative would mean that they do not visit the site of a collapsed building. This, of course, is a concerning situation as victims may reside in the damaged building that is now being missed during search and rescue operations. On the other hand, a false positive would mean that the site is being visited but the search and rescue team would notice on the spot that the building has not been damaged after which they can move on. One could argue that the time saved by having a preliminary indication of possible damaged buildings with a minimized amount of false positives is more time saving than not having such information at all. From a rescue worker point of view the damage detection map is therefore best interpretable if false positives are kept at a minimum and the false negatives are preferably even not present at all.

Normal Distribution Approach

The first change detection algorithm that was applied uses the mean and standard deviation of the pre-disaster σ_0 values as thresholds. This approach is based on the assumption that each pixel consists of a timeseries which follows a normal distribution (in dB), where extreme values are less frequent than values that are closer to the mean of the timeseries. In the case (a part of) a building collapses due to a disaster, the next time the satellite overpasses the radar reflection might be significantly higher or lower compared to the averaged reflection of that same building from before the disaster, thus resulting in an extreme value:

H_0 = Building did not collapse and the σ_0 in dB follows a normal distribution.

H_A = Building did collapse and the σ_0 in dB exceeds one of the standard deviation thresholds.

Because we assume a normal distributed signal, adding/subtracting one, two or three times the standard deviation to/from the mean results in a pixel value that theoretically would enclose 68%, 95% or 99.7% of the possible pixel values based on the background noise in the pre-disaster timeseries. If a pixel value of the post-disaster image would exceed one of these thresholds, the pixel is masked with a yellow, orange or red color, respectively:

$$\text{Thresholds} = \begin{cases} \mu_{\sigma_0} - \sigma_{\sigma_0} > \sigma_0 > \mu_{\sigma_0} + \sigma_{\sigma_0} & \text{the pixel is masked with a yellow color.} \\ \mu_{\sigma_0} - 2\sigma_{\sigma_0} > \sigma_0 > \mu_{\sigma_0} + 2\sigma_{\sigma_0} & \text{the pixel is masked with an orange color.} \\ \mu_{\sigma_0} - 3\sigma_{\sigma_0} > \sigma_0 > \mu_{\sigma_0} + 3\sigma_{\sigma_0} & \text{the pixel is masked with a red color.} \end{cases}$$

This also has been depicted for a single pixel and its coherent timeseries in figure 3.10. The results of this approach are shown in figure 3.11. It can be seen that a lot of pixels have been identified as changed in the reference image, and thus exceeding the one sigma confidentially interval. This complicates the determination whether a changed pixel actually indicates a damaged building (correctly classified) or an effect unrelated to the earthquake (false positively classified). However, there is a strong increase of pixels that have been severely altered based on the 3 sigma confidentially interval (red color) over the old city center in the post-disaster change detection map. Here, many buildings have been damaged or even collapsed and this is where a high density of changed pixels is expected. It can therefore be concluded that it does perform well on the damage detection side, although keeping in mind that the amount of false positives is very high. It would in that sense benefit the interpretation of the change detection map if both a post-disaster as well as a pre-disaster change detection map are provided so that differences between the two can be interpreted as damaged buildings.

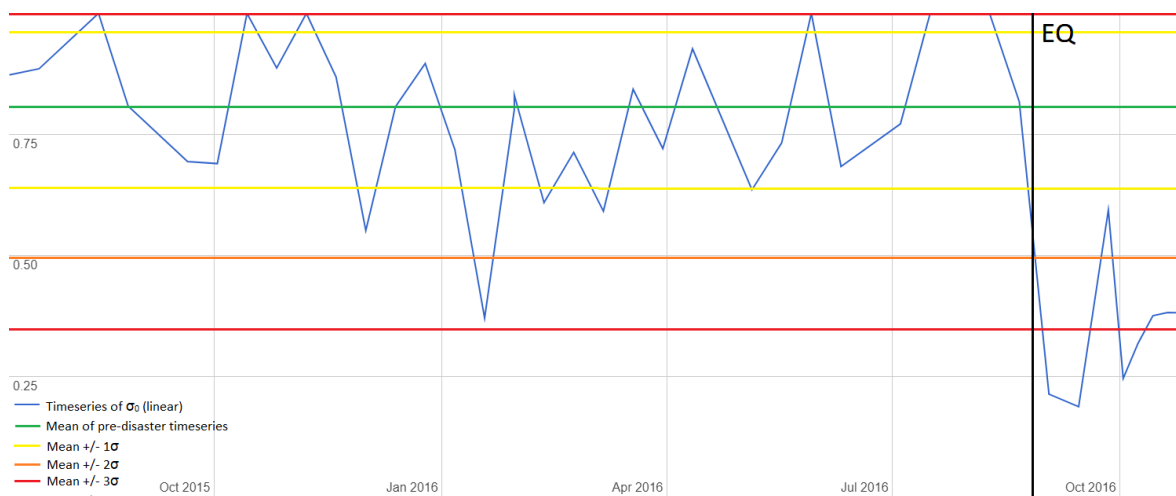


Figure 3.10: Example of how the Normal Distribution damage detection approach would work for a pixel. If the post-disaster value (first point after the earthquake line in black) exceeds one of the thresholds that are based on the mean and standard deviation of the pre-disaster timeseries, the pixel is colored yellow, orange or red depending on the post-disaster value of σ_0 .

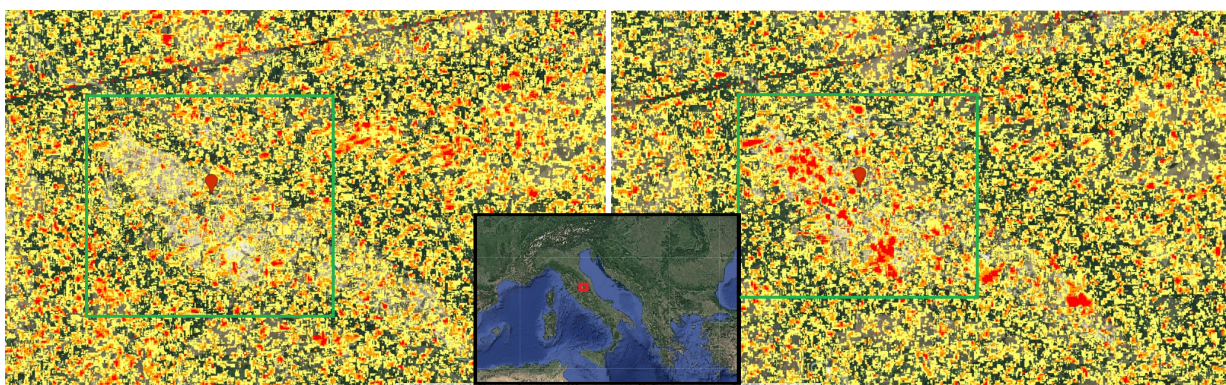


Figure 3.11: Results from the Normal Distribution approach over the area of Amatrice, Italy after the L'Aquila 2016 earthquake. On the left-hand side the result of a reference test with the last pre-disaster image and on the right-hand side the results with the post-disaster image. Pixels are masked with a yellow, orange or red color once the pixel value of the first post-disaster acquisition exceeds the thresholds determined by adding/subtracting one, two or three times the standard deviation to/from the mean of the pre-disaster timeseries, respectively. The line is a gap in the data due to a mosaicking error between two Sentinel-1 acquisitions. The green square overlaps with the green square in the ground truth data in 3.16.

Percentile Approach

Another approach, related to the first approach, results from a more general assumption that the pre-disaster timeseries follows a certain distribution that is not known on forehand and might be different per pixel:

H_0 = Building did not collapse and the σ_0 value falls within 80% of the middle percentiles.

H_A = Building did collapse and the σ_0 value falls within the lower or upper 10% percentiles.

Exploiting this assumption, one can use the percentiles of the pre-disaster timeseries to determine the values of the 10%, 5% and 1% limits for each pixel that have occurred in the pre-disaster timeseries and compare these limits to the pixel values of the post-disaster image. Here again we expect the disaster to affect the σ_0 values in such a way that either in the ascending or descending direction a significant increase/decrease is detected. If a post-disaster pixel value is greater or smaller than the 10%, 5% or 1% limit values the pixel will get masked by a yellow, orange or red color, respectively, to indicate it is changed based on these thresholds:

$$\text{Thresholds} = \begin{cases} \text{lower 10\% percentile value} > \sigma_0 > \text{upper 10\% percentile value} & \text{the pixel is masked with a yellow color.} \\ \text{lower 5\% percentile value} > \sigma_0 > \text{upper 5\% percentile value} & \text{the pixel is masked with an orange color.} \\ \text{lower 1\% percentile value} > \sigma_0 > \text{upper 1\% percentile value} & \text{the pixel is masked with a red color.} \end{cases}$$

This also has been depicted for a single pixel and its coherent timeseries in figure 3.12.

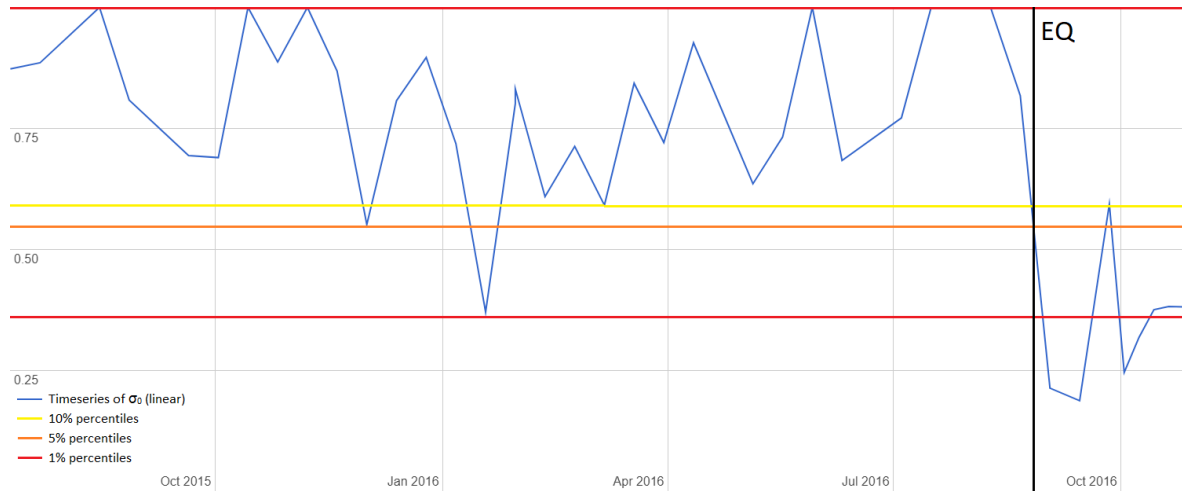


Figure 3.12: Example of how the percentile damage detection approach would work for a pixel. If the post-disaster value (first point after the earthquake line in black) exceeds one of the thresholds that are based on the percentiles of the pre-disaster timeseries, the pixel is colored yellow, orange or red depending on the value of σ_0 .

The results of this algorithm are shown in figure 3.13. With respect to the previous change detection approach it can be seen that fewer pixels have been false positively identified as damaged buildings. Again the concentration of colored pixels increases over the city center where many buildings collapsed, indicating that the algorithm correctly responds to building damage. However, the amount of false positively classified pixels again limits the ability to determine accurate locations of damaged buildings. This could be improved by providing a reference map of pre-disaster data.

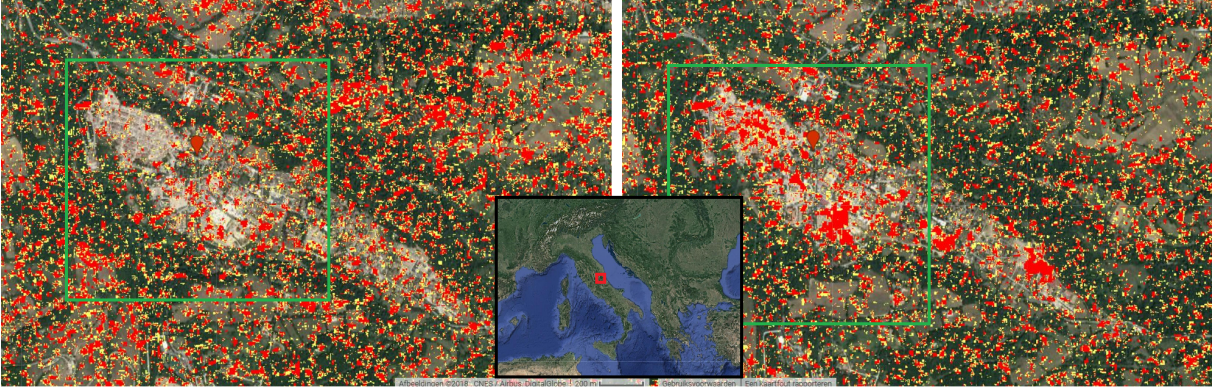


Figure 3.13: Results from the percentile approach over the area of Amatrice, Italy after the L'Aquila 2016 earthquake. On the left-hand side the result of a reference test with the last pre-disaster image and on the right-hand side the results with the post-disaster image. Pixels are masked with a yellow, orange or red color once the pixel value of the first post-disaster acquisition exceeds the thresholds determined by the values of the 10%, 5% and 1% limits of the pre-disaster timeseries, respectively. The green square overlaps with the green square in the ground truth data in 3.16.

Gradient Approach

A different approach is based on the change of a pixel σ_0 value between two subsequent acquisitions. Assuming the change in the reflected radar signal for a pixel in the co-disaster image pair ($\Delta\sigma_0$) is significantly larger than the natural changes in the pixel values based on the pre-disaster timeseries, this can be exploited for change detection. This is related to the differencing approach as discussed by Matsuoka and Yamazaki [2004] in equation 2.12. However, here we will not make use of a spatial averaging as the GRD imagery already has been averaged through a 5x1 window. Furthermore, the linear scaling will be used instead of the logarithmic scaling that is applied by Matsuoka and Yamazaki [2004] as discussed in subsection ???. What remains is the following equation:

$$d = I a_i - I b_i, \quad (3.12)$$

with d being the difference between the intensity I of pixel i in image a and that same pixel in image b . From here on, a new timeseries is computed where each image contains pixel values that represent the change between pixel values of two subsequent acquisitions:

$$C_{N_{ij}} = O_{N+1_{ij}} - O_{N_{ij}}, \quad (3.13)$$

where $C_{N_{ij}}$ represents Nth image of the new timeseries containing the differences in pixel values of image N+1 ($O_{N+1_{ij}}$) and image N ($O_{N_{ij}}$) of the original timeseries. The maximum value of $\Delta\sigma_0$ is determined for each pixel and then compared to the $\Delta\sigma_0$ of the co-disaster pair. If this co-disaster pixel value exceeds the threshold it is indicated as changed:

H_0 = Building did not collapse and the absolute $\Delta\sigma_0$ value does not exceed any of the $\Delta\sigma_0$ values previously observed.

H_A = Building did collapse and the absolute $\Delta\sigma_0$ value is does exceed the maximum observed $\Delta\sigma_0$ value previously observed.

This approach accounts for the fact that, when using one of the algorithms discussed above, the σ_0 value was already low in the last pre-disaster acquisition due to natural variations and that an additional natural effect might decrease the backscattered reflection even more. This sequence of natural effects decreases the σ_0 value of a pixel in such a way that it surpasses the above mentioned threshold and is then identified as changed. By looking at the absolute changes of the pixel values instead of the pixel values themselves, this aspect is avoided. In order to interpret the severity of the co-disaster $\Delta\sigma_0$ value compared to pre-disaster $\Delta\sigma_0$ values, a ratio between the two is calculated and the pixels are colored according to the value of the ratio. So, if the co disaster $\Delta\sigma_0$ value exceeds the highest observed pre-disaster $\Delta\sigma_0$ value, the following ratio is calculated:

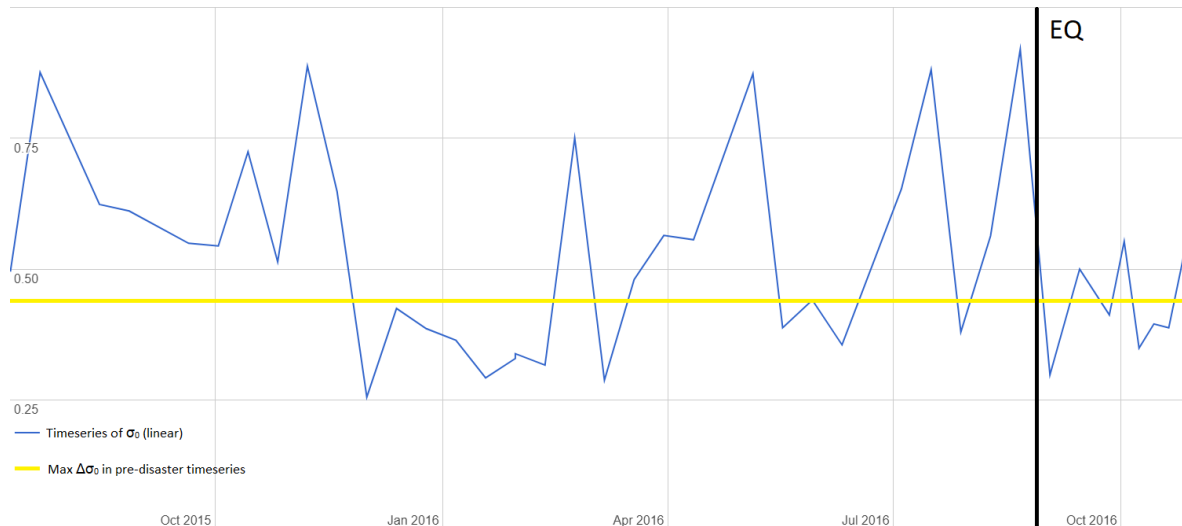


Figure 3.14: Example of how the gradient damage detection approach would work for a pixel. If the co-disaster $\Delta\sigma_0$ (points before and after the earthquake line in black) exceeds the threshold that is based on the maximum $\Delta\sigma_0$ of the pre-disaster imagepairs, the pixel is detected as significantly changed. Then, a ratio is calculated between the co-disaster $\Delta\sigma_0$ value and the maximum $\Delta\sigma_0$ of a pre-disaster imagepair and based on this ratio the pixel is colored gradiently from yellow to red.

$$S_{\Delta\sigma_0} = \frac{\Delta\sigma_{0co-disaster}}{\max(\Delta\sigma_{0pre-disaster})}. \quad (3.14)$$

Then if the pixel is masked with a color ranging from yellow to red for values of $S_{\Delta\sigma_0}$ ranging from 1.0 to 2.0. The use of the maximum observed pre-disaster $\Delta\sigma_0$ for thresholding also has been depicted for a single pixel and its coherent timeseries in figure 3.14. Note that each pixel that is indicated as changed has a minimal co-disaster $\Delta\sigma_0$ value of 1.0 dB as this is the radiometric accuracy of the backscattering intensity for the Sentinel-1 mission (Suhet [2013]). It can be seen in figure 3.15 that the amount of false positively classified pixels has significantly decreased over both vegetation and urban areas when comparing this reference image to the reference images of the two previous approaches. Also, the amount of changed pixels increases over the area that consists of many damaged buildings in the post-disaster image. These are two important aspects that make the result of this approach the most easy to use and interpret damage detection map from the three approaches presented in this research. In order to further show the possibilities of this change detection algorithm it is applied to various case studies and analyzed as a tool for rapid disaster response situations in the next chapter but first, a complete overview of the damage detection algorithm will be presented in the next section.

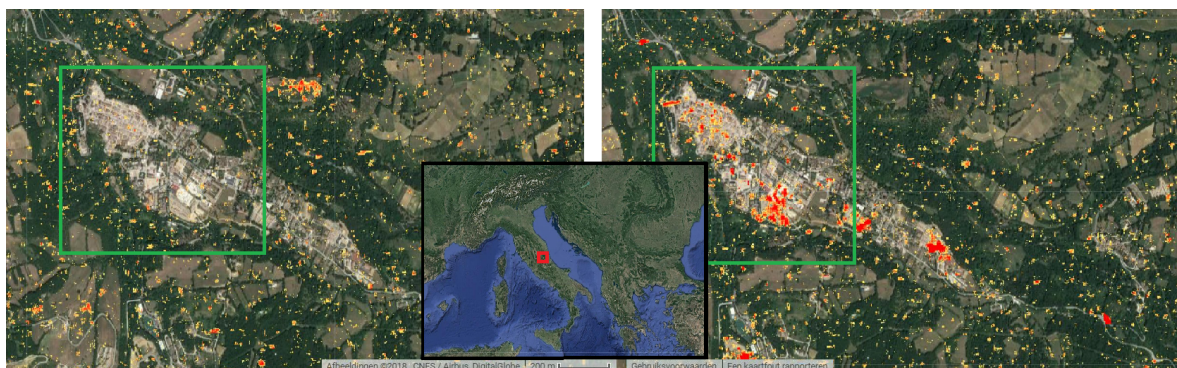


Figure 3.15: Results from the Gradient approach over the area of Amatrice, Italy after the L'Aquila 2016 earthquake. On the left-hand side the result of a reference test with the last two pre-disaster images and on the right-hand side the results with the co-disaster imagepair. Pixels are masked with an yellow, orange or red colour once the absolute change in the pixel σ_0 value in the co-disaster acquisition pair is larger than the largest observed $\delta\sigma_0$ between the acquisitions in the pre-disaster timeseries. The colors are scaled to the maximum observed absolute change in the pre-disaster timeseries ranging from 1.0 (yellow) to 2.0 (red). The green square overlaps with the green square in the ground truth data in 3.16.

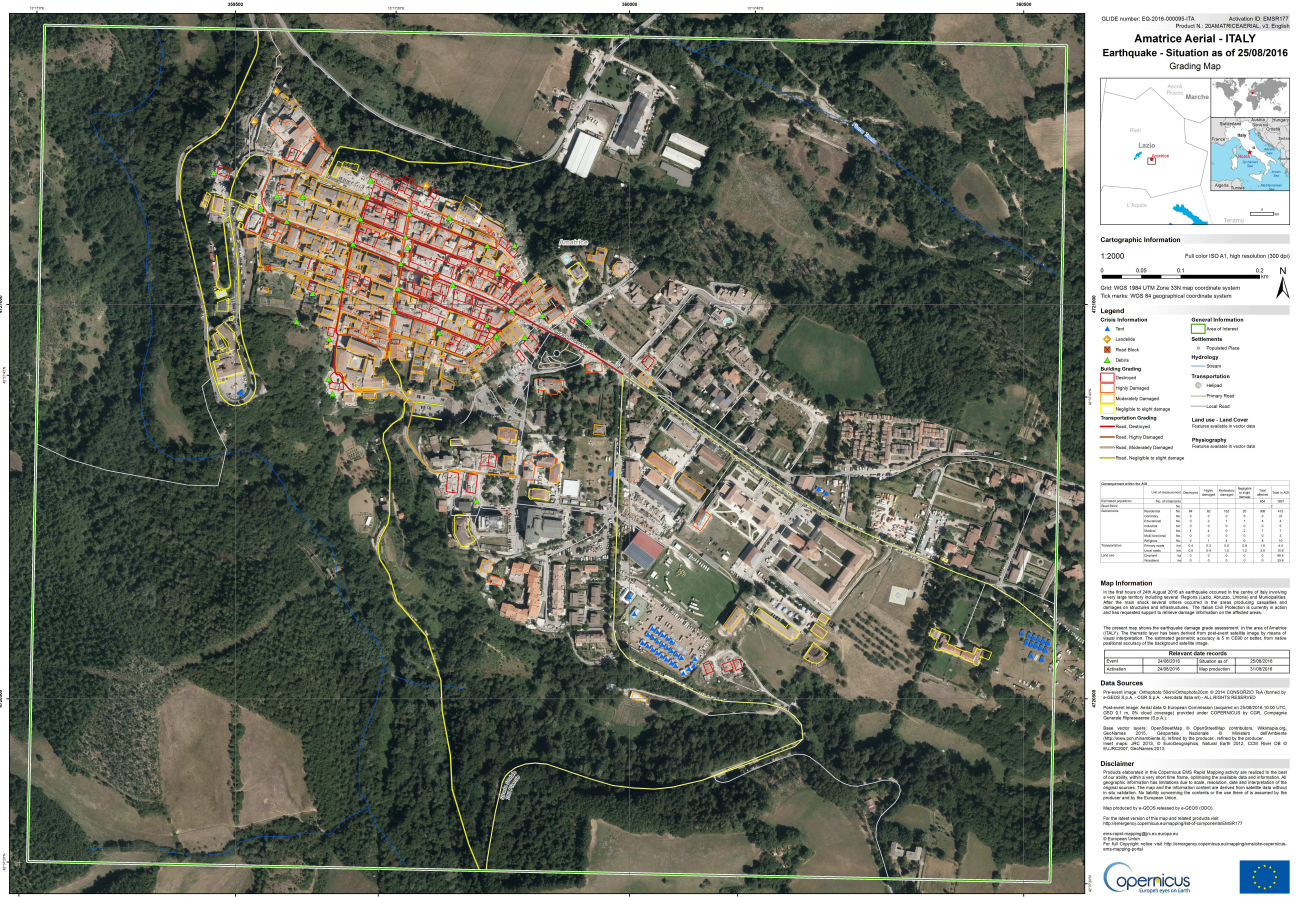


Figure 3.16: Ground truth data of the L'Aquila earthquake on the 24th of August 2016 for the city of Amatrice, published by the GMES-ERS on 31-08-2016 (<http://emergency.copernicus.eu/mapping/list-of-components/EMSR177>).

3.5. Application of Damage Detection System into Practice

This section will present a complete and thorough overview of the damage detection algorithm as a whole in case a disaster would happen and the search and rescue teams would like to use the damage detection algorithm presented here. This overview will discuss every step in the script on how to start the algorithm, how the result should be interpreted, what data latency can be expected and what to do if no post-disaster acquisition is available.

The first task of any search and rescue group in a disaster area is the Assessment, Search and Rescue Level 1 where the size of the disaster is estimated and the area is divided in sectors to maintain overview, identify possible hazards and prioritize tasks for a plan of action. Within this first level, the damage detection algorithm proposed in this research can be immediately put to use once the location and date are known. In the case a large earthquake strikes anywhere on Earth, the USGS sends out a warning containing the magnitude and epicentre of the earthquake. With this information, one should visit https://code.earthengine.google.com/?accept_repo=users/jeroenvheyningen/Open which accesses the Google Earth Engine Code Editor (figure 3.1). In the `Damage_General` script, the input parameters can be inserted and processed by the algorithm once Run is pressed. This initiates the algorithm to gather the available VV polarized, high-resolution Sentinel-1 GRD imagery in IW mode from the very first image in the imagecollection to the most recent image acquired over the area of interest for both ascending and descending orbits.

In case no post-disaster acquisition is available yet for both ascending and descending orbits, a notification is generated that shows a the date for the next acquisitions in ascending and descending orbits after which the algorithm is terminated. If for either one of the orbits a new acquisition is available, the script continues while displaying the date of the next acquisition for the missing orbital direction and a notification that the damage detection results may be less accurate when using acquisitions from only one of the orbits. This is due to geometrical complications between the incoming signal and the building orientation as depicted in figure 3.4. So, the possible outcomes for the post-disaster acquisition check are:

Post-disaster Acquisition = Check Outcome	}	Continuation without notifications	if Post-disaster Acquisition in both Asc & Dsc are available
		Continuation with notification of next Asc/Dsc acquisition and warning on map result	if No Dsc/Asc post-disaster acquisition is available
		Termination of script and notification of next Asc & Dsc acquisition	if No Asc & Dsc post-disaster acquisitions are available

The calculation of the next expected data is completed by checking which relative orbits cover the area of interest in both orbital directions in reversed chronological order. Then, if an acquisition of a certain relative orbit is found for the second time in the reversed chronological order the repeat frequency can be determined for that specific area. This repeat frequency is then added to the date of the acquisition prior to the repeated relative orbit, as the prior relative orbit is expected to pass the area of interest next. This results in a calculation of the date a next acquisition is made of the area of interest. However, this does not mean that at the given moment the acquisition is also ready to use in the Google Earth Engine. The moment an acquisition is available in the EE can only be approximated as the data latency can be caused by either the observation scenario of the Sentinel-1 mission, the processing of the GRD imagery by ESA or the downloading from SciHub and post-processing of the data by the GEE. The data latency due to the observation scenario of the Sentinel-1 mission has been taken care of by applying the calculation discussed above, so what remains is the data latency by ESA or the GEE. The processing of the raw SAR data to Level-1 GRD imagery by the ESA is always done within 24 hours after acquisition. However, on an operational basis this is generally reduced to only a few hours with an average of 5.5 hours. Last, there is the data latency caused by the downloading of the GRD imagery from SciHub and the post-processing by the GEE before it can be inserted in their own data archive. The GEE aims at performing this within 48 hours after it being made available on SciHub, but this is generally also done faster. Unfortunately, no statistics on this part are available according to Ilyushchenko [2018]. This would lead to a cumulative maximum data latency of 72 hours after the acquisition has been made, which is within the maximal time it would take for the USAR team to arrive in the affected country.

The algorithm can be repeatedly operated until a post-disaster image is available for one of the orbital directions. If both orbital direction imagecollections contain a post-disaster acquisition, based on the point given as input the most recent imagery that has a proper coverage of the AOI is selected and the relative orbit numbers are extracted for both orbital directions. From here on, the ascending and descending imagecollections can be filtered on their specific relative orbit numbers so that the latest acquired image can be compared with pre-disaster imagery that has been observed under similar conditions. What results is a pre-disaster imagecollection and a post-disaster image for each orbital direction. However, if for only one of the orbital directions a post-disaster acquisition is available the algorithm continues and only does the processing for that orbital direction.

As an intermediate step, Landsat 8 imagery is imported and filtered for the AOI and data range of January 1 2015 to the most recently acquired imagery. For each individual image the NDVI is calculated per pixel. Following, for each pixel the highest observed NDVI value in the entire data stack is taken and compared to a threshold value of 0.9. If the highest observed NDVI value would exceed this threshold, it would mean that during the aforementioned time period the pixel has been classified as vegetation at least once. Furthermore, the Normalized Difference Water Index (NDWI) for open water bodies is calculated using the Green (band 3, 0.53 - 0.59 μm) and NIR (band 5, 0.85-0.88 μm) from the same Landsat dataset through McFeeters [1996]:

$$NDWI = \frac{GREEN - NIR}{GREEN + NIR} \quad (3.15)$$

The NDWI also varies from -1 to +1 where values higher than 0 indicate water. In the algorithm the median of the entire timeseries is used and the threshold of 0.5 is applied to classify water bodies. These masks will be used as a non-urban mask later on in the processing.

After these calculations, the change detection algorithm is applied to the two imagecollections separately. For the pre-disaster timeseries the change in σ_0 is calculated for each image pair, as well as for the co-disaster image pair. Then, depending on whether the $\Delta\sigma_0$ of the co-disaster image pair has increased or decreased, the ratio is calculated between the $\Delta\sigma_0$ of the co-disaster pair and the highest positive or lowest negative $\Delta\sigma_0$ of the pre-disaster image pairs. Once this ratio exceeds the value of 1.0, the pixel is indicated as "changed" and is colored a range of yellow to red scaled to the value of the ratio from 1.0 to 2.0, respectively. If post-disaster from both acquisitions are available, the results from the ascending and descending orbits are combined to one final damage detection map. This combination of the two maps is completed by selecting the result for each pixel that detected the highest amount of change in the post-disaster imagery. So if one of ascending or descending orbits did detect a change, that pixel result is selected and if both of the orbits have detected a significant change the highest change detection ratio is selected:

$$\text{Final Map Result} = \begin{cases} \text{No change detected} & \text{if Asc \& Dsc did not detect a change} \\ \text{Asc change} & \text{if Dsc did not detect a change} \\ \text{Dsc change} & \text{if Asc did not detect a change} \\ \text{Highest observed change} & \text{if Asc \& Dsc did detect a change} \end{cases}$$

For this combined change detection map the vegetation is masked through the vegetation mask from Landsat data. Next the map is displayed on the Map in the Google Earth Engine. Here, the point that is given as input is displayed as a blue cross and one could scroll through the map to search for urban areas and check the damage detection results. The map can optionally be exported as a KML file through the Tasks tab by pressing Run. As an indication: the processing of the algorithm for Syria took around 14 seconds, the loading of the resulting damage detection map around 1 minute and 5 seconds and the exporting of the map to the Google Drive 40 seconds. These time indications are for a case where 152 ascending and 149 descending Sentinel-1 GRD images and 806 Landsat 8 images have been processed.

The damage detection map should be interpreted as a change detection map that indicates locations of possible damaged or collapsed buildings in urban areas after a disaster. The heavier the building is damaged, the higher the backscattering signal is expected to be affected and, assuming that this effect is more severe than what the backscattering signal of this pixel has experienced in the pre-disaster timeseries, the more reddish the color of the detected pixel will be. Note that due to the viewing geometry of the satellite system with respect to the geometry of the building that is observed, the change in the backscattering intensity might be more or less heavily affected due to changes in the reflecting properties as a result of building damage. Also, false positives may arise due to changes in the surface properties not related to the earthquake that affect the backscattering intensity in such a way the pixel also is detected as changed.

This damage detection map can then be put to use in the estimation of the size of the disaster, the division of the area in sectors and the prioritization of these sectors in terms of amount of potential damaged buildings and thus potential casualties. The complete approach presented in this research is depicted in figure 3.17 for clarity. In the following section this approach is repeated for various case studies in order to evaluate the operativeness of this algorithm in a rapid response situation.

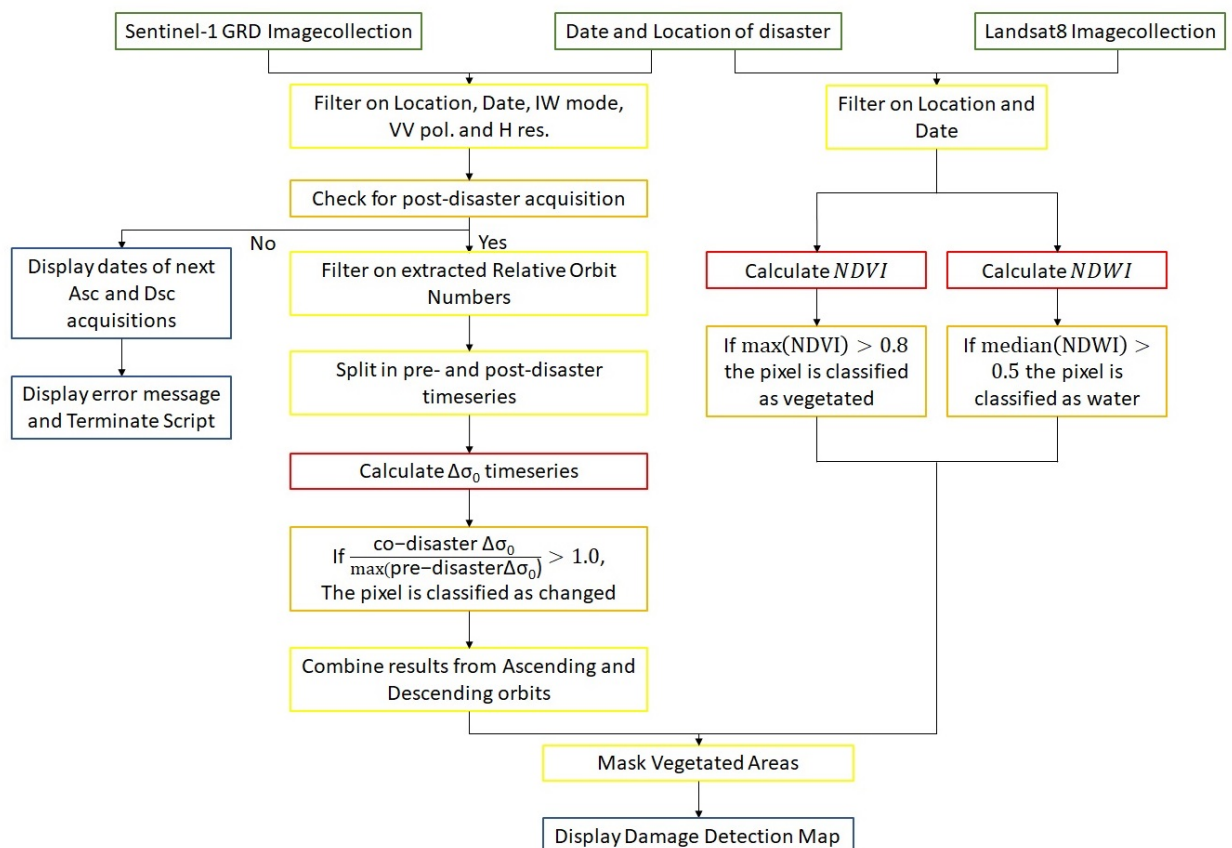


Figure 3.17: Overview of the algorithm that results in the damage detection maps as presented in this research. It depicts the input used for the algorithm (green), the data selection applied to the imagecollections (yellow), the statements the data needs to fulfill (orange), calculations applied per pixel on the data and finally the most important aspects that have been displayed (blue).

4

Results

In this chapter, the performance of the change detection algorithm will be discussed by evaluating the generated damage detection maps for multiple test cases. In order to determine the performance of the algorithm, it will be applied to various areas that have been affected by earthquakes or intentional damage during military strikes. Ideally, a general algorithm results in correctly identified collapsed buildings for various regions. In order to remove pixels that have been detected as collapsed buildings outside urban areas, and hence being falsely detected as collapsed buildings, an additional non-urban mask will be applied. The goal while designing this algorithm was for it to be user friendly so that rescue workers without any remote sensing experience are able to understand and use it, efficient so that it will not take hours to generate the damage detection map and of course accurate as it should correctly detect collapsed buildings. It can be argued that ideally the algorithm will only detect collapsed buildings, but as in any hypothesis testing there are false positives (pixels detected as changed that do not cover collapsed buildings) and false negatives (collapsed buildings that have not been detected as changed). In the situation of rapid disaster response, it is more valuable to create a damage detection map where the false negatives are at a minimum, as you would rather visit sites that are still intact than miss sites where casualties may reside. All of these aspects are of importance in order to determine whether the algorithm can be useful for rescue operations in rapid disaster response situations.

So in conclusion, the main goals for the damage detection algorithm as a whole and the damage maps in particular is to maximize the following aspects:

- Time efficiency
- Applicability
- Reliability
- Interpretability

Ideally, the accuracy of the damage detection maps and hence the significance of the detected pixels is evaluated for the case studies by comparing the maps to detailed ground truth data. This would give a proper insight in the performance of the change detection algorithm in detecting building damage. Unfortunately, such information was not openly available and could therefore not be used in this research. Instead, various maps indicating building damage in the various areas have been used. Note that due to the high variability of building types and urban environments where disasters may occur, such detection accuracy indications for the case studies presented here do not guarantee a similar performance for other areas. In order to comply to the added value of the damage detection algorithm presented here regarding global applicability and high impact, an alternative is presented in the manual as presented in B.1.

Three locations have been selected as case studies in order to test the operativeness of the algorithm (figure 4.1). The first case study is the M6.2 2016 Central Italy earthquake, the second is the M7.1 2017 Central Mexico earthquake and third and last the 2018 Syrian military strikes. Each case study will be accompanied by a description of the situation, the evaluation of the damage detection algorithm as a whole, a description of the validation data used and finally the validation of the damage detection map itself for a specific location. As mentioned in subsection 3.2, the algorithm requires a manual input of the date of the disaster and the point of interest after which the damage detection map is automatically generated and displayed in the Google Earth Engine. Enlarged figures of the results and the coherent validation data can be found in appendix A.



Figure 4.1: Overview of the locations of the three case studies that have been selected to demonstrate the effectiveness of this damage detection algorithm.

4.1. Earthquake: Amatrice, Italy (2016)

An earthquake of M6.2 hit Central Italy on August 24, 2016 at 03:36:32 CEST. The epicenter was located 45 km north of L'Aquila, the capitol of the Abruzzo region with a population of +/- 71,000 inhabitants. Because of the time of the earthquake, many people were asleep and therefore surprised by the tremors. The earthquake caused the death of a total of 299 people, of which 234 in Amatrice. As most casualties were found in Amatrice, this city is selected as the first case study for the testing of this algorithm. Additionally, clear ground truth data of collapsed building was distributed by the GMES as depicted in figure 3.16 which resulted in the ability to compare the results of the algorithm to the ground truth data. The variable parameters used for this case study are depicted in table 4.1 and have been based on the epicenter (42.71°N , 13.17°E) and the date (24/08/2016) of the earthquake:

Date of Disaster	24-08-2016 01:36:32 UTC
Post-disaster Acquisition	27-08-2016 17:05:18 UTC (Asc) 26-08-2016 05:19:23 UTC (Dsc)
Area of Interest	Polygon 43.18°(N) , 14.18°(E) , 41.86°(S) , 12.37°(W)
Orbit Numbers	117 (Asc) 95 (Dsc)

Table 4.1: Overview of the input parameters and acquired imagery for the 2016 Central-Italy earthquake (M6.2).

In this case study the imagery from descending orbit has been acquired within 72 hours after the earthquake struck, whereas the imagery from the ascending orbit was obtained within 88 hours. Unfortunately, the selected acquisition in descending orbit cannot be used for rapid damage detection over the city of Amatrice, because Amatrice was located on the very edge of the Sentinel-1 swath. And as discussed in subsection 3.2, the edge of a Sentinel-1 swath consists of no-data and low intensity values which have been introduced in the generation of the Level-1 products from raw data and subsequently masked in the GRD border noise removal step. As the final damage detection map identifies changed pixels over areas where both orbital directions are covered, the final map also only covers half of the AOI. One could use the change detection map based on only ascending acquisitions but as illustrated in figure 3.4 this approach might oversee collapsed buildings related to the viewing geometry.

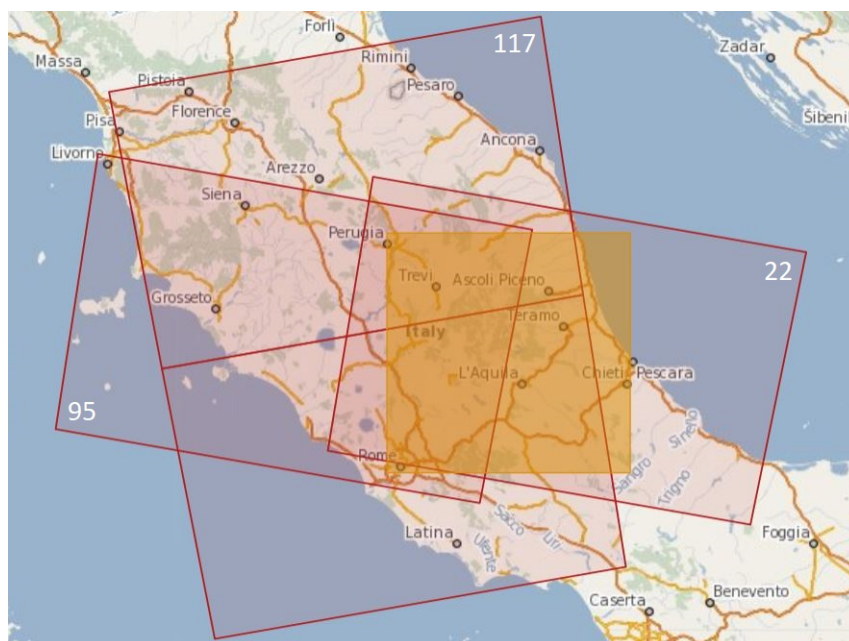


Figure 4.2: Overview of the suitable relative orbits for this case study. Here, it can clearly be seen that the descending orbits both (partly) cover the AOI (yellow box) but that relative orbit 95 only covers half and hence excluding i.e. Amatrice, whereas relative orbit 22 results in a satisfying coverage. Image obtained from SciHub: <https://scihub.copernicus.eu/dhus/>

In order to analyze the damage detection algorithm over the city of Amatrice, the Copernicus Sci Hub data portal was manually checked and it was found that relative descending orbit number 22 better covers the area of interest, as depicted in figure 4.2. An overview of the change detection algorithm from combined ascending and descending acquisitions (from manual input) is depicted in figure 4.3. Here, the colored pixels represent significantly changed pixels, meaning that the co-disaster $\Delta\sigma_0$ is larger than the highest observed pre-disaster $\Delta\sigma_0$. Downside of changing this relative orbit is that the most recent post-disaster acquisition is from September 2nd, more than nine days after the earthquake and thus obstructing a rapid disaster response. This directly illustrates the disadvantage of satellite-based damage detection approaches. However, for the purpose of checking the accuracy of the damage detection algorithm the acquisitions of relative orbits 117 and 22 will be used, while keeping in mind that the damage detection based on imagery from the descending orbit might also be affected by the effects due to the (partial) clearing of the debris. Note that the clearing of the debris alters the backscattering signal and might hamper a correct evaluation of the change detection algorithm.

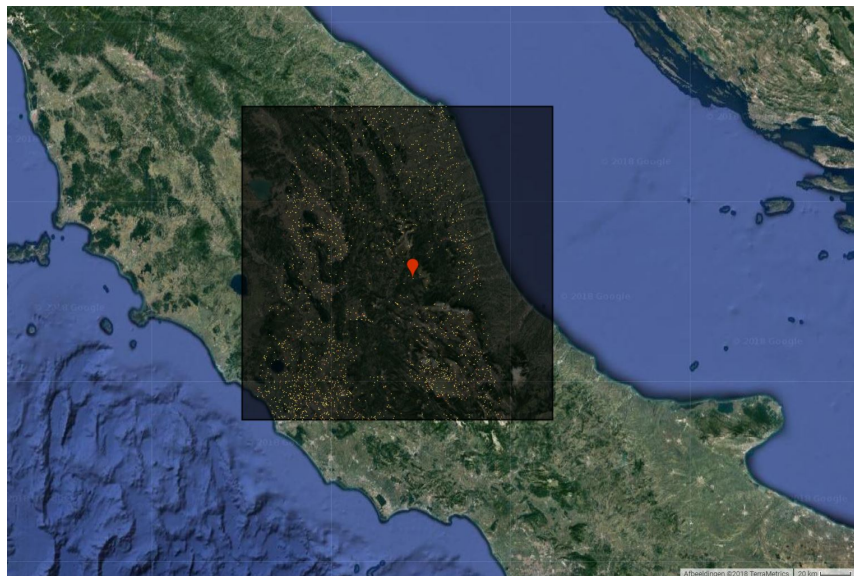


Figure 4.3: Overview of the results from the gradient approach damage detection algorithm for the M6.2 Central-Italy earthquake (2016), based on acquisitions of relative orbit numbers 117 (Asc) and 22 (Dsc). The grey box represents the AOI whereas pixels that qualify as non-vegetated (yearly maximum NDVI lower than 0.8) and non-water (yearly median NDWI lower than 0.5) have been colored in the range yellow to red when the ratio between the observed co-disaster change in σ_0 and highest observed change in σ_0 is in the range of 1.0 to 2.0. The red marker indicates the city of Amatrice.

The results of this approach have been compared to a grading map of damaged buildings in Amatrice, generated by the Copernicus Emergency Management System. As explained in section 3.4.2, the grading map is obtained by manually comparing high resolution optical pre- and post-disaster imagery and checked for changes in urban structures and areas of rubble. The final map was generated 7 days after the event happened and shows roads and buildings that have been detected as destroyed (red), highly damaged (dark orange), moderately damaged (light orange) and negligible to slight damage (yellow) for an area of interest (green polygon). However, as this grading map is based solely on satellite imagery these classifications are thus solely based on what could be seen from the satellite point of view, being damage to the roof or clear piles of rubble next to a building. Cracks or ruptures in the building material on the sides of a building could therefore not be identified. Ideally, the results of the approaches are compared to actual ground truth data which describes every type of damage to a building but as this is not available, the grading map, which have been derived without in situ validation as explained in the disclaimer, is the best available option for the validation.

The comparison between the Copernicus EMS grading map and the gradient approach damage detection result is shown in figure 4.4. As can be seen in the grading map, the city centre in the top-left part of the image (white polygon) was heavily damaged. Unfortunately, this is not as clear when looking at the damage detection image. From the damage detection map, three interesting areas can be identified as indicated by the blue numbered circles. Area 1 covers the western part of the city center and shows many pixels that have been detected as changed. Most of the heavily changed pixels (red color) correspond to buildings that have been identified as destroyed or highly damaged in the grading map. The moderately changed pixels (yellow to orange color) overlap with moderately damaged buildings in the grading map. In this area three larger clusters of heavily changed pixels can be identified, two in the top and one in center left. The cluster in the top left nicely overlaps with a building classified as damaged, whereas the cluster in the top right overlaps with buildings that have been classified in a range from slight to heavily damaged. However, the cluster in the center left overlaps with trees and a road indicated as negligible to slight damage. This clearly is a false positive error in the damage detection gradient approach, which could have been masked out by a very precise vegetation mask. The vegetation mask applied here is not that precise as the Landsat 8 spatial resolution is 40m and the threshold for detecting vegetated areas is set high so that the situation, where pixels that are not most definitely vegetated throughout the year are masked, is avoided. Last mention for this area is the cluster of moderately to heavily changed pixels on the right which overlaps with moderately to completely damaged buildings in the grading map. A clear illustration for this cluster considering ground truth evidence is depicted in figure 4.5.

Area 2 covers the eastern part of the city center and some apartment blocks and living areas to the south of the city center. Again, the amount of pixels detected as changed over the city center does not match with what would be expected from the severity of damage as illustrated in the grading map results. The damage detection map shows a few clusters of heavily changed pixels over the city center but most of them are in the range of moderately changed (yellow to orange) and overlap with buildings identified as destroyed in the damage grading map. Just south of the city center, three larger clusters of heavily changed pixels can be seen. Of these three, the most right one matches with a moderately damaged building. The other two (on the left and in the center) mostly overlap with trees and a parking lot and are therefore false positively detected as damaged structures. The center cluster however, extends somewhat more in a north-south direction than the one on the left and it therefore also overlaps with a moderately damaged building in the north and a slightly damaged building in the south. In the bottom of the circle again three clusters of heavily changed pixels can be seen, of which the left one overlaps with destroyed buildings, the center one with a heavily damaged building and the most right one with a moderately damaged building. This increase in level of damage from right to left also nicely matches the increase in size and redness of the three clusters. Moreover, the bottom left cluster, as well as the large cluster of heavily changed pixels in the top right of area 2, have also been identified in figure 4.5 as a collapsed apartment block and a damaged church, respectively.

Most remarkably in the damage detection map is the large area of detected pixels in the lower-central part of the image (area 3) which is not indicated by any means as severely damaged in the grading map, i.e. false positives. Except for a heavily changed cluster in the top that overlaps with moderately to heavily damaged buildings and a cluster of heavily changed pixels in the bottom that overlaps with destroyed buildings, the rest of the heavily changed pixels do not overlap with any kind of damage. Further inspection of this area points out that it is some sort of industrial terrain including blue markers that indicate tents. Looking at the split change detection results from the ascending and descending orbit, both show such a large area of detected pixels and as the co-disaster date ranges in both orbit directions differ (August 15 to August 27 and August 21 to September 2, respectively) we can assume significant changes of the backscattering in the SAR pixel must have occurred somewhere between August 21 and August 27. As we know from the grading map that tents have been put up in that same area, this effect might be related to the search and rescue operations after the earthquake.

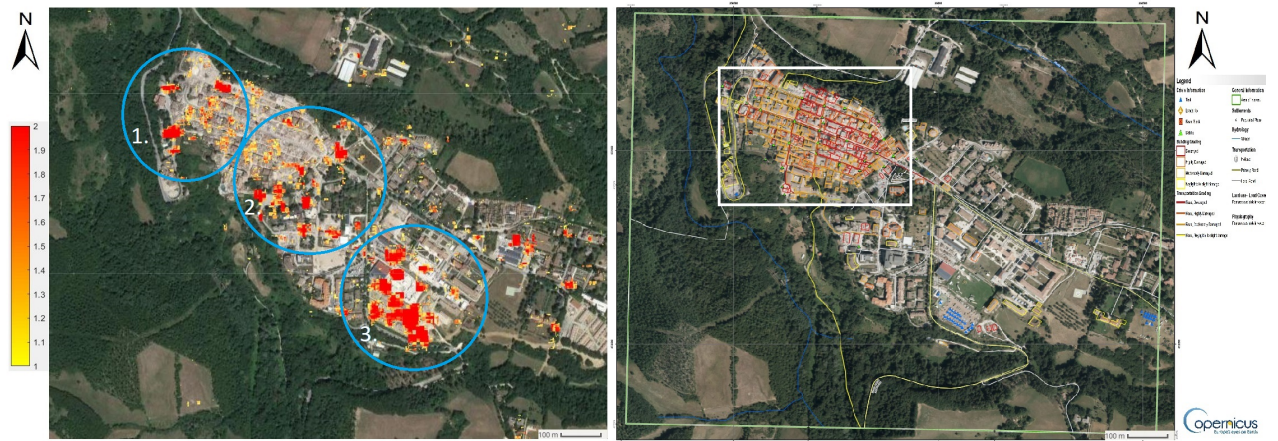


Figure 4.4: Results of the gradient approach damage detection algorithm for the city of Amatrice after the M6.2 2016 Central-Italy earthquake (left). Pixels that qualify as non-vegetated (yearly maximum NDVI lower than 0.8) and non-water (yearly median NDWI lower than 0.5) have been colored in the range yellow to red when the ratio between the observed co-disaster change in σ_0 and highest observed change in σ_0 is in the range of 1.0 to 2.0. The image on the right-hand side shows the grading map provided by the Copernicus Emergency Management System that indicates damaged buildings. Enlarged versions of the result and validation data are depicted in section A.1.

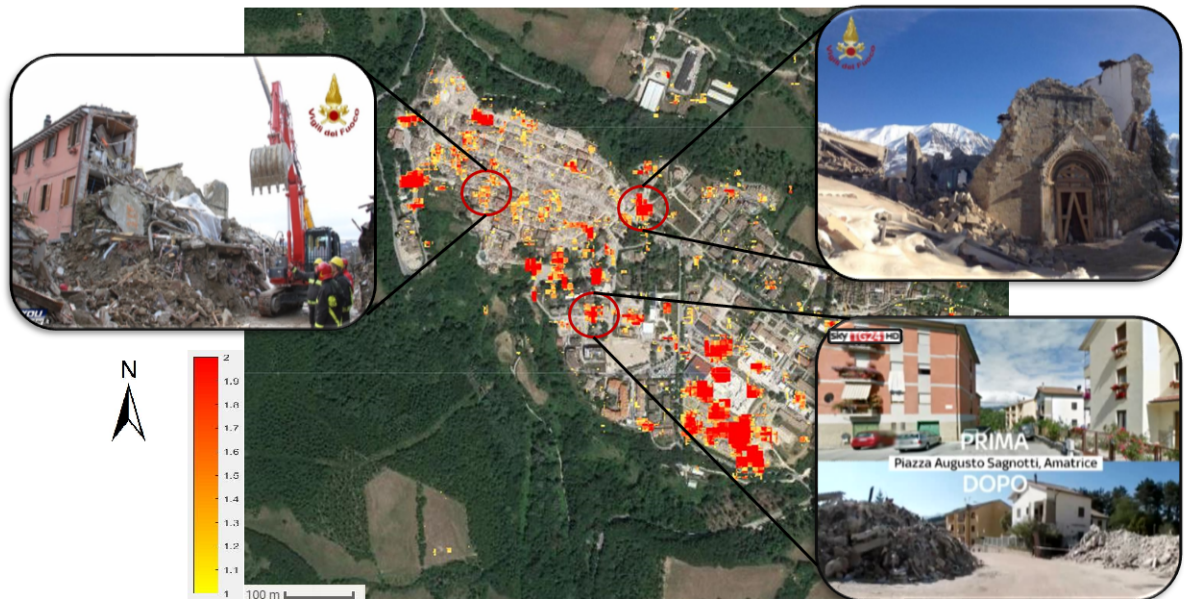


Figure 4.5: Results of the gradient approach damage detection algorithm for the city of Amatrice after the M6.2 2016 Central-Italy earthquake. Pixels that qualify as non-vegetated (yearly maximum NDVI lower than 0.8) and non-water (yearly median NDWI lower than 0.5) have been colored in the range yellow to red when the ratio between the observed co-disaster change in σ_0 and highest observed change in σ_0 is in the range of 1.0 to 2.0. Three of these clusters of detected pixels have been inspected and pictures of collapsed buildings at those same locations have been found and depicted here. The top two images have been obtained from the Vigili del Fuoco whereas the bottom right image has been obtained from SkyTG24.

Concluding for this case study it can be said that the collapsed buildings in the city center were not as obviously detected as changed by the algorithm, except for a few individual cases, as would have been expected from the severity of damage in that same area. This could have something to do with the looking direction of both ascending and descending orbits as the main streets are mostly east-west oriented and the incoming radar signal is directed to the north-west-west (ascending) or north-east-east (descending). And in a small Italian city, where buildings are built close to each other, the collapsing of a structure might not alter the radar reflection enough as complex scattering can take place within the collapsed structure or with the building behind the collapsed building in the line of sight, but this is speculation. What can be concluded is that the severity of the change in the backscattering signal overlapped for most cases with the severity of damage as indicated by the grading map. Also some areas of false positively changed detected pixels have been observed, mostly covering streets, parking lots, trees and the industrial area. In these areas significant changes have been observed that did not overlap with damaged structures, but this does not directly mean that the changes observed in those pixels were not related to the earthquake. As discussed in the previous paragraph, the large cluster of changed pixels might have been related to the setting up of search and rescue tents. This could also have been done on the parking lot or streets that were detected as changed, also possibly related to demolition and clearing of the debris. Additionally, the need for using acquisitions from both orbit directions has been shown as damage detection results improve significantly when using both orbit directions (figure 4.6). Most importantly is the conclusion that, although not on the individual building level, the large area of damaged buildings can be identified as multiple clusters of moderately to heavily changed pixels where this cannot be seen over the area of Amatrice where no damaged buildings were identified.



Figure 4.6: Results of the gradient approach damage detection algorithm for the city of Amatrice after the M6.2 Central-Italy earthquake (2016). Pixels that qualify as non-vegetated (yearly maximum NDVI lower than 0.8) and non-water (yearly median NDWI lower than 0.5) have been colored in the range yellow to red when the ratio between the observed co-disaster change in σ_0 and highest observed change in σ_0 is in the range of 1.0 to 2.0. The image on the left-hand side shows the results from only using ascending acquisitions while the image on the right-hand side resulted from using both ascending and descending acquisitions.

4.2. Earthquake: Mexico City, Mexico (2017)

On September 19, 2017 at 13:14:38 CDT an earthquake of M7.1 hit the area of Central Mexico. The epicenter was about 55 km south of the city of Puebla, the capitol and largest city of the state Puebla in Mexico. Many horrifying videos appeared of buildings that shook and collapsed in Mexico City during the 20-second period of strong shaking. The earthquake killed a total of 370 people and it induced collapsed buildings, including 228 in Mexico City. Because of the wide availability of building damage reports in Mexico's capital and the ability to test the damage detection algorithm in a dense urban environment this situation has been selected as a case study. The variable parameters used for this case study are depicted in table 4.2 and have been based on the epicenter (18.58°N, 98.40°W) and the date (19/09/2017) of the earthquake:

Disaster Date	19-09-2017 18:14:38 UTC
Post-disaster Acquisition	20-09-2017 00:39:42 UTC (Asc) 23-09-2017 12:24:44 UTC (Dsc)
Area of Interest	Polygon 19.48°(N), -97.45°(E), 17.68°(S), -99.34°(W)
Orbit Numbers	5 (Asc) 143 (Dsc)

Table 4.2: Overview of the input parameters and acquired imagery for the 2017 Puebla earthquake (M7.1).

In this situation the imagery has been acquired within 90 hours after the earthquake struck. Although this is longer than the critical 72 hours of significant survival rates found for the 1995 M7.2 Kobe earthquake, this time period of significant survival rates is expected to be longer for this case study as the most common building material used in Mexico City is reinforced concrete (Murakami [1996]). Using this material generally increases the survival rate up to a time period of 6 days(144 hours) of significant survival rates, meaning that the damage detection results obtained for this case study might still have been useful in search and rescue operations. Contrary to the Amatrice case study, the relative orbits that were automatically selected by the algorithm proved to be useful in terms of coverage of the AOI. Hence, the resulting damage detection map automatically generated from only the date of the earthquake and the coordinates of the epicenter would be directly usable.

An overview of the resulting damage detection algorithm for the entire region is shown in figure 4.7. Here, the colored pixels represent significantly changed pixels for the combined ascending and descending orbits, meaning that the co-disaster $\Delta\sigma_0$ is larger than the highest observed $\Delta\sigma_0$ in the pre-disaster timeseries. A clear distinction in the concentration of changed pixels can be observed between the top and bottom half of the AOI. Further inspection points out this distinction is visible in the change detection results of the descending orbits, whereas the pre-disaster imagecollection contains less acquisitions in the bottom half (49) than the top half (106) due to the observation scenario of the Sentinel-1 mission. As mentioned before, the algorithm determines whether a pixel has been changed significantly based on the $\Delta\sigma_0$ of the co-disaster pair relative to the highest observed $\Delta\sigma_0$ in all pre-disaster pairs. However, natural variations in the backscattering intensity may coincidentally result in a similarly large change in the backscattering intensity signal between two acquisitions. This effect should be accounted for when more reference acquisitions are included in the pre-disaster timeseries, so that all possible ranges of $\Delta\sigma_0$ for each pixel due to natural variations have been observed. From then onward one may expect that only changes in geometric features of objects on the surface, either man-made (i.e. construction work) or natural (i.e. collapsing buildings due to earthquakes), will result in a pixel to be detected as changed. Although successful damage detection through the change detection algorithm in the lower half might have been more difficult due to the lower amount of available acquisitions, Mexico City is located in the top half and thus not expected to be affected by this issue.

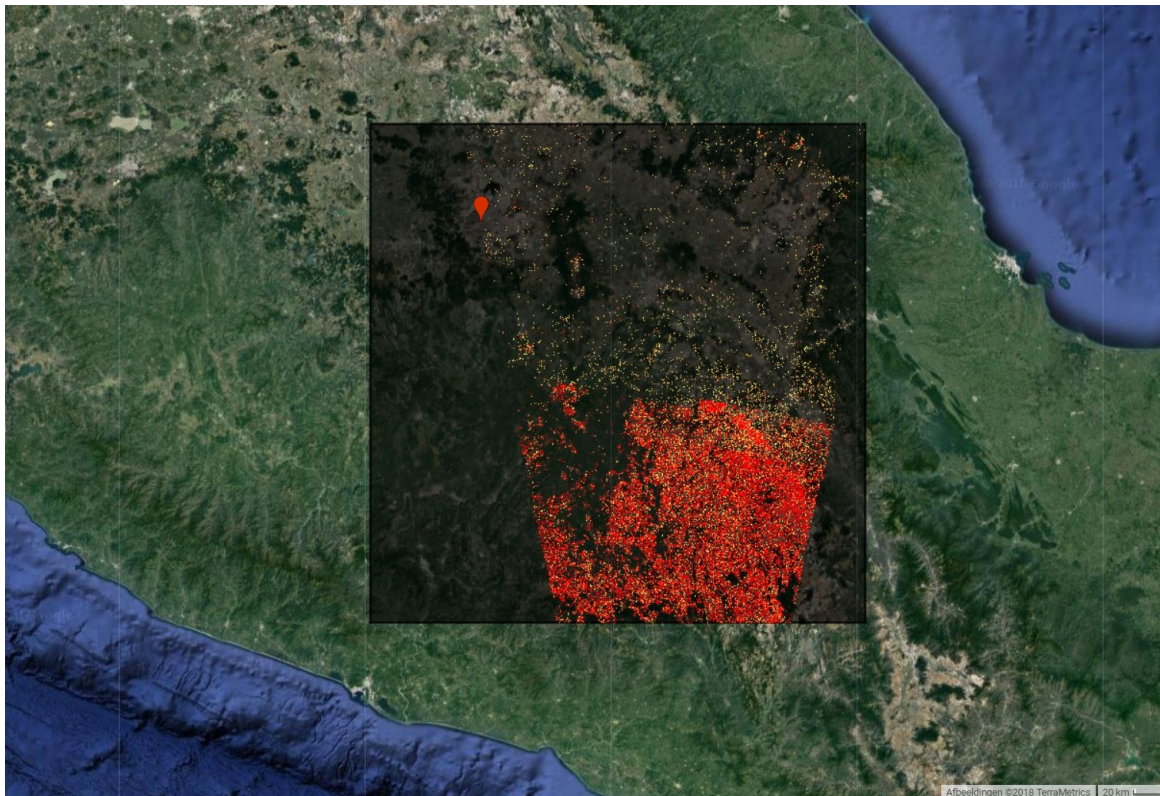


Figure 4.7: Overview of the results from the gradient approach damage detection algorithm for the M7.1 Central-Mexico earthquake (2017). The grey box represents the AOI whereas pixels that qualify as non-vegetated (yearly maximum NDVI lower than 0.8) and non-water (yearly median NDWI lower than 0.5) have been colored in the range yellow to red when the ratio between the observed co-disaster change in σ_0 and highest observed change in σ_0 is in the range of 1.0 to 2.0.

As no damage grading map has been generated by the Copernicus EMS, the results of this algorithm for the area of Mexico City has been compared to a crowd-sourced Google Map that also has been used by the JPL ARIA team to evaluate their damage proxy map. Additionally, some damage grading maps have been distributed by the International Charter Space and Major Disasters, but these maps focused only on small parts of Mexico City. The crowd-sourced validation map extends further over the city but this area has been chosen as this also has been pointed out by the ARIA team for the high density of collapsed or damaged buildings. The crowd-sourced map shows markers that identify the locations of collapsed (red), mayor damaged (orange), moderately damaged (yellow) buildings and shows locations of gas leaks (purple) and other aspects related to the earthquake (grey). As it is a crowd-sourced map, the damage scales cannot be directly linked to the EMS-damage grading scale and the precise type of damage cannot be linked to the severity of the change in the backscattering signal. However, the locations of the markers are assumed to be correct.

The comparison of the damage detection algorithm presented in this research with the crowd-sourced ground truth map is shown in figure 4.8. On average about 50% of the markers indicating collapsed or heavily damaged buildings correspond to pixels detected as changed by the algorithm. However, for this area the detection performance is lower and corresponds to roughly 35%. In particular the two markers on the Avenida Alvaro Obregon correspond really well with two clusters of severely changed backscattering intensity values. One of these buildings was an office building which collapsed with still many people present in the building at the moment of the earthquake. The collapsed building is pointed out in figure 4.9. However, also multiple clusters of detected pixels in the top-left, bottom-left and center-right can be seen that do not overlap with any indication of collapsed or damaged buildings and are thus false positives resulting from non-damage related changes on the surface. These areas still could have been caused by other activities resulting from the earthquake, such as search and rescue operations or demolition, but this is speculation.

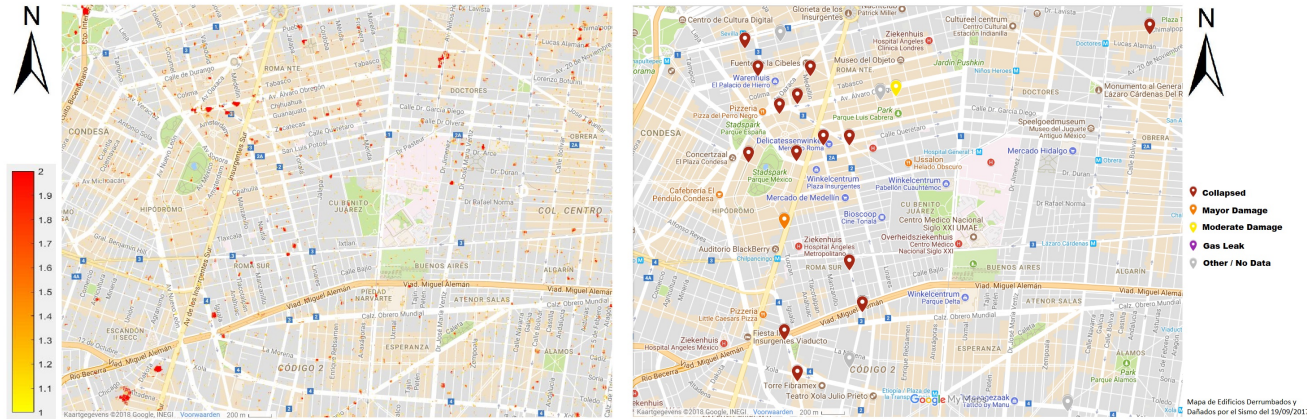


Figure 4.8: Results of the gradient approach damage detection algorithm for Mexico-City after the M7.1 Central-Mexico earthquake (2017) are shown in the left-hand side. Pixels that qualify as non-vegetated (yearly maximum NDVI lower than 0.8) and non-water (yearly median NDWI lower than 0.5) have been colored in the range yellow to red when the ratio between the observed co-disaster change in σ_0 and highest observed change in σ_0 is in the range of 1.0 to 2.0. On the right-hand side, a crowd-sourced Google map indicating collapsed and damaged buildings is shown as validation. The crowd-sourced map is obtained from https://www.google.com/maps/d/u/0/viewer?mid=1_V971bdgLFHpx-CtqhLWlJAnYY&ll=19.415634726751634%2C-99.16466053928525&z=15. Enlarged versions of the result and validation data are depicted in section A.2.

All in all, for this case study it can be stated that the algorithm does work very well with the date and location parameters given as input. From those two inputs, the right data is selected and damage detection algorithm is applied to result in a damage detection map. The damage detection itself is able to locate actual damaged buildings up to some extent but not every building is identified by the algorithm. This definitely is a loss as, stated before, it would be key for rescue workers planning their search and rescue operations if every collapsed building is actually detected (no false negatives) and it would be less disturbing when a pixel is identified as changed where this does not correspond to a damaged building (accepted false positives). The reason for missing collapsed buildings could again be related to the building environment with high buildings located closely together and hence resulting in a complex reflection of the radar signal. This could lead to a hampering of a significant change in the backscattering signal once a building collapses, as other structures in the surroundings could still result in a proper reflection.

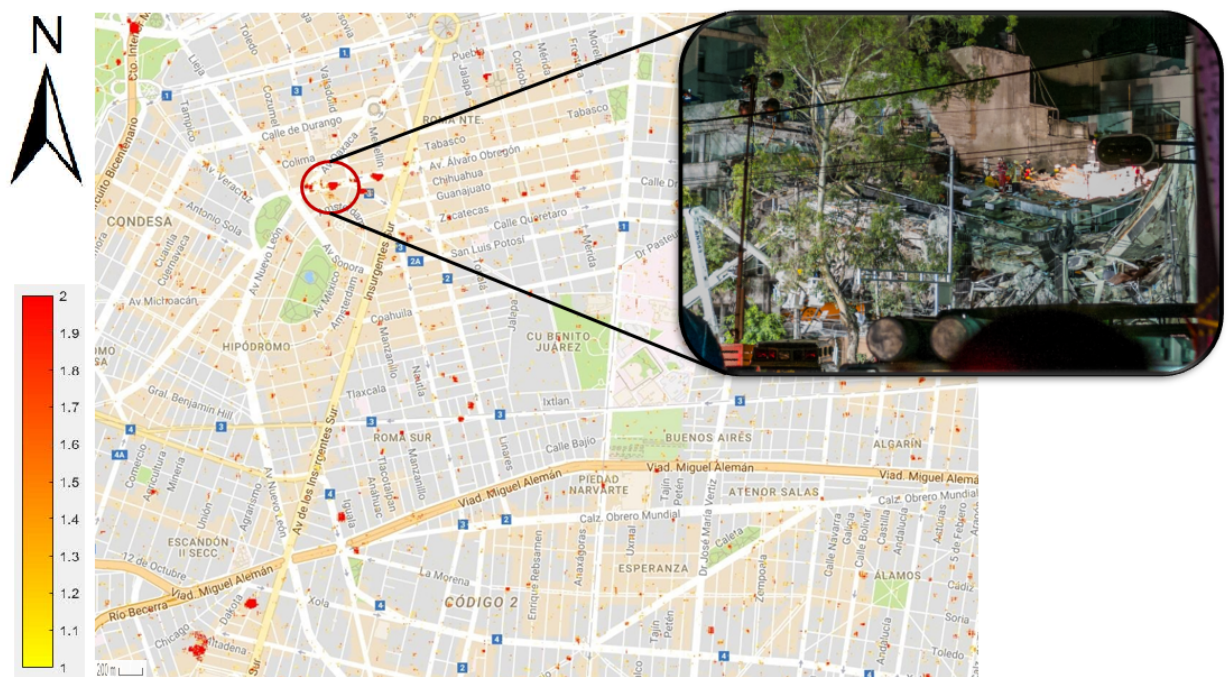


Figure 4.9: Results of the gradient approach damage detection algorithm for Mexico-City after the M7.1 Central-Mexico earthquake (2017) are shown in the left-hand side. Pixels that qualify as non-vegetated (yearly maximum NDVI lower than 0.8) and non-water (yearly median NDWI lower than 0.5) have been colored in the range yellow to red when the ratio between the observed co-disaster change in σ_0 and highest observed change in σ_0 is in the range of 1.0 to 2.0. One of these clusters has been further inspected and pictures of collapsed buildings at that same locations have been found and depicted here. The image has been obtained from LA Times.

4.3. Military Strikes: East-Ghouta, Syria (2018)

Instead of a disaster response approach, the algorithm could also be operated from a monitoring perspective. With continuous bombings in various regions of the Middle East, it is rather complex for the rescue teams and NGO's to offer help to the civilians trapped in the ongoing violence. It might in those situations be useful if a continuous monitoring system is implemented that automatically detects collapsed buildings. This way the supporting organizations know where to go and then assess themselves whether it is safe for them to start offering help. As a case study the algorithm is applied to the series of military strikes in Syria on 14-04-2018, which begun at 04:00 EEST. The military strikes were carried out by the United States, France and the United Kingdom as a reaction on the suspected chemical attack on April 7 by the Syrian government. The chemical attack was aimed at the remaining rebel groups in the Eastern Ghouta region, specifically the city of Douma, and was responsible for over 70 casualties and at least 500 injured. During the series of military strikes, three targets have been bombed, being: the Barzah Research and Development center in Damascus, the Him Shinshar Chemical Weapons Storage Facility near Homs and the Him Shinshar Chemical Weapons Bunker and Command Center also near the city of Homs. The variable parameters used for this case study are depicted in table 4.3 and have been based on the location of the research center in Damascus (33.53°N, 36.34°E) and the date (14/04/2018) of the bombings:

Disaster Date	14-04-2018 01:00:00 UTC
Post-disaster Acquisition	18-04-2018 15:31:46 UTC (Asc) 19-04-2018 03:34:02 UTC (Dsc)
Area of Interest	Polygon 34.91°(N), 37.93°(E), 32.21°(S), 34.71°(W)
Orbit Numbers	14 (Asc) 21 (Dsc)

Table 4.3: Overview of the input parameters and acquired imagery for the 2018 Military Strikes in Syria by the US, French and British forces.

In this situation the imagery has been acquired within 122 hours after the bombings started. Again, the automated approach selected acquisitions of relative orbits that sufficiently cover the AOI. An overview of the resulting damage detection algorithm for the entire region is shown in figure 4.10. Here, the colored pixels represent significantly changed pixels, meaning that the co-disaster $\Delta\sigma_0$ is larger than the highest observed $\Delta\sigma_0$. With respect to the overview of the M7.1 2017 Mexico case study, here no distinctions in the concentration of changed pixels can be observed. Therefore it can be concluded that the resulting damage detection map can be used and analyzed for accuracy based on the automated approach of the algorithm. As the airstrikes were aimed at specific targets, the results of the algorithm will be inspected for these three locations.

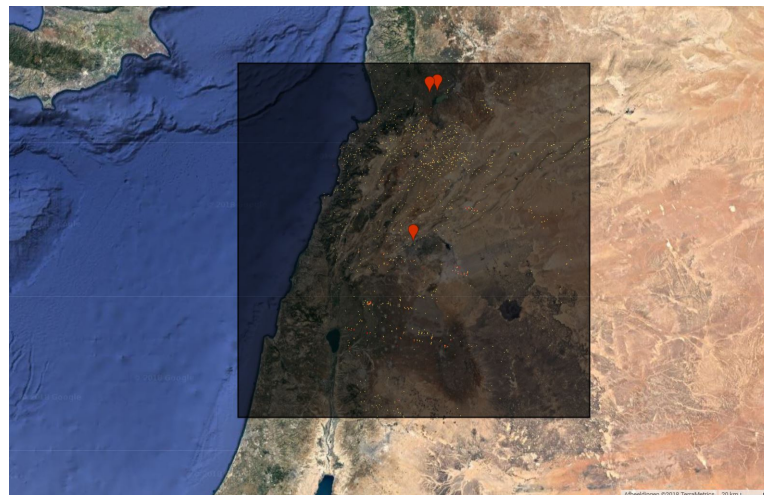


Figure 4.10: Overview of the results from the gradient approach damage detection algorithm for the Rif Damashq Offensive in February 2018. The grey box represents the AOI whereas pixels that qualify as non-vegetated (yearly maximum NDVI lower than 0.8) and non-water (yearly median NDWI lower than 0.5) have been colored in the range yellow to red when the ratio between the observed co-disaster change in σ_0 and highest observed change in σ_0 is in the range of 1.0 to 2.0.

The first comparison is made for the research center near Damascus, using Image Sat International data from the Pleiades satellite as depicted in figure 4.11. From this before and after validation image it can be concluded that the building has been completely destroyed. This severity of destruction can also be observed when looking at the damage detection map as the damaged research center is accurately indicated by a large cluster of reddish colored pixels. Related to other clusters of changed pixels, in the middle-right and bottom-center, it can be seen that the severity of significant change (degree of red of a pixel) is lower but the size of the cluster is larger. However, due to the limited amount of information for this region and the ongoing Rif Damashq Offensive of the Syrian government it could still be possible that these other significant changes within the urban area are related to building collapse or other types of damage.



Figure 4.11: Results of the gradient approach damage detection algorithm for the military strike of the Barzah Research and Development Center in Damascus, indicated by the white circle. Pixels that qualify as non-vegetated (yearly maximum NDVI lower than 0.8) and non-water (yearly median NDWI lower than 0.5) have been colored in the range yellow to red when the ratio between the observed co-disaster change in σ_0 and highest observed change in σ_0 is in the range of 1.0 to 2.0. The results on the left-hand side are compared to Image Sat International optical data of the bombed site, acquired by the Pleiades satellite. Enlarged versions of the result and validation data are depicted in section A.3.

The second comparison is done for the Him Shinshar Chemical Weapons Storage Facility near Homs, using a before and after comparison map generated from the U.S. Department of Defence. Here, three separated buildings were targeted with air-strikes and as a result have again been completely destroyed. Note that the size of these buildings is about a factor 5 smaller than the research center (20m), so the expected spatial extent of the clusters is also smaller. This would also be the smallest building size the algorithm is expected to resolve due to the spatial resolution of 20x20m for Sentinel-1 GRD imagery. The comparison is depicted in figure 4.12 with the facility indicated by the black circle in the image on the left. From the three individual buildings, building damage in the middle and right one have been observed as a significant change in the backscattering intensity by the algorithm. For the building in the middle, the co-disaster $\Delta\sigma_0$ was at least twice as large as the highest observed $\Delta\sigma_0$ in the pre-disaster timeseries, indicated by the red pixel. For the building on the right, a somewhat larger cluster of detected pixels can be seen with a range between one and two times the ratio of co-disaster and maximal pre-disaster $\Delta\sigma_0$. These significant changes can, besides the building damage, also be related to changes in the surface surrounding the facility as the missile impact may have created a crater that increases and decreases the backscattering intensity through the change in slope. Again, three clusters of severely changed pixels in the urban area on the right can be seen that are supposedly unrelated to the air-strike. It is less likely that this area is related to the Rif Damashq Offensive as this only held for the East-Ghouta district. These significant changes may therefore be caused by changes in the geometrics of surface features such as building construction or the positioning of trucks and/or cars in the resolution cell.



Figure 4.12: Results of the gradient approach damage detection algorithm for the military strike of the Him Shinshar Chemical Weapons Storage Facility near Homs, indicated by the white circle. Pixels that qualify as non-vegetated (yearly maximum NDVI lower than 0.8) and non-water (yearly median NDWI lower than 0.5) have been colored in the range yellow to red when the ratio between the observed co-disaster change in σ_0 and highest observed change in σ_0 is in the range of 1.0 to 2.0. The results on the left-hand side are compared to data from the U.S. Department of Defence. Enlarged versions of the result and validation data are depicted in section A.3.

The final comparison has been completed for the Him Shinshar Chemical Weapons Bunker near Homs, using again a before and after comparison map generated from the U.S. Department of Defense. Three objects have been targeted by the air-strikes, all three with a spatial extent of no more than 7m. This is smaller than the spatial resolution of the GRD pixel cells and it is therefore expected that, unless the impact is significantly large for it to dominate the backscattering intensity in the resolution cell, it will not be observed by the damage detection algorithm. The structures are harder to identify but it is assumed that the buildings have at least been damaged with partial collapse as a result. The comparison is depicted in figure 4.13 with the facility indicated by the black circle in the image on the left. Looking at the damage detection result it can be seen that only at the location for the object on the far-right a significant change has been observed. However, as it is colored yellow it means that it barely surpassed the threshold of the maximal observed $\Delta\sigma_0$ in the pre-disaster series. This signal is also insignificant when comparing it to the already present false-positively detected pixels due to the natural variations in the backscattering intensity. The larger cluster of detected pixels north of the objects may be related to changes in the slope of the surface due to the impact of the missiles. This is can also be partially observed in the before and after imagery, showing that the hilly structures surrounding the bunker have been flattened.

For this case study it can be concluded that the damage detection algorithm can also be operated for detecting building damage due to bombings in conflict areas, under the assumption that the spatial extent of the objects is larger than the spatial resolution of the pixel cells (20x20m) in order to be resolvable. When the spatial extent is smaller than or equal to this threshold, the effect of building damage is not significant enough to dominate the backscattering intensity in the resolution cell. Hence, it will not be measured as a significant change in $\Delta\sigma_0$.



Figure 4.13: Results of the gradient approach damage detection algorithm for the military strike of the Him Shinshar Chemical Weapons Bunker near Homs, indicated by the white circle. Pixels that qualify as non-vegetated (yearly maximum NDVI lower than 0.8) and non-water (yearly median NDWI lower than 0.5) have been colored in the range yellow to red when the ratio between the observed co-disaster change in σ_0 and highest observed change in σ_0 is in the range of 1.0 to 2.0. The results on the left-hand side are compared to data from the U.S. Department of Defense. Enlarged versions of the result and validation data are depicted in section A.3.

5

Discussion and Conclusions

This chapter presents a discussion of the entire damage detection algorithm and its results by answering the three sub-questions stated at the start of this research, being:

1. Is the Sentinel-1 archive usable for detecting building damage?
2. How does this damage detection algorithm perform in a rapid disaster response situation after earthquakes and intentional damage in conflict areas?
3. Are the resulting building damage maps sufficiently informative and useful for rescue operation teams in their planning and rescue work?

Furthermore, the conclusion of this master thesis research is presented, together with recommendations and an outlook. The conclusion focuses on formulating an answer to the main research question:

"How can the entire Sentinel-1 SAR archive be used operationally for rapid disaster response situations?"

5.1. Discussion

This research has aimed to show the opportunities of Sentinel-1 SAR GRD data hosted by the Google Earth Engine for damage detection during rapid disaster response situations with the Dutch USAR team as a possible end-user. Currently, search and rescue operations are initiated by ground teams that, as a first step, perform wide area assessment. Here, the area of interest is divided into sectors and tasks are prioritized for a plan of action. The USAR team in particular, determines as quickly as possible after a disaster whether or not their help may be useful. They make the decision for deployment based on whatever information they can get their hands on, ranging from traveling guides from the bookstore to web-based applications such as Google Maps and Streetview. A valuable addition to these types of information are maps with indications of damaged structures in the area of interest, which can be acquired through remote sensing techniques.

Remote sensing instruments placed on various platforms (UAVs, airborne and spaceborne) show prospective results for damage detection but vary in their ability to assist on a large scale. UAV and airborne platforms usually depend on whether pre-disaster data is available and the size of the area that can be covered, which limits their performance in wide area assessment. For satellite platforms these aspects are resolved as they have a repeating track over the surface of the Earth and thus measure the surface over a large area repetitively. A distinction can be made between optical and SAR imagery, which both can be operated for rapid damage detection. The advantage of SAR over optical data is that the radar signal is independent of illumination, hence it can be operated during day and night, and is able to penetrate clouds, causing each successful acquisition to be available for damage detection.

Multiple studies have shown the possibility of using the phase or amplitude of the SAR signal or a combination of both for damage detection. However, most studies have been completed when large SAR datasets were not easily accessible and most of these change detection algorithms have hence been based on bi- or tri-temporal change detection. With the consistent observation scenario and the open-data policy of the

Sentinel-1 mission by ESA, more extensive and consistent pre-disaster timeseries are available which can be exploited for new damage detection approaches in rapid disaster response situations.

1. Is the Sentinel-1 archive usable for detecting building damage?

The Google Earth Engine provides, among others, the entire Sentinel-1 GRD dataset on their web-based server. By bringing the algorithms to the data instead of the other way around, significant amount of time can be saved as no data has to be downloaded individually. Unfortunately, the GRD product only offers intensity information of the backscattered radar signal with a 20x20m spatial resolution. Therefore we cannot benefit the highest spatial resolution or the use of the phase of the SAR signal for the development of a damage detection approach.

Following, three different change detection approaches using the backscattering intensity have been tested for the city of Amatrice after the M6.2 2016 L'Aquila Italy earthquake. Restrictions for a correctly working change detection algorithm in rapid disaster response were that, obviously, damaged buildings were correctly identified, false negatives were avoided as much as possible and the amount of false positives were kept at a minimum to allow for easy interpretation of damaged buildings in the change detection map. The best performing approach based on these restrictions was the algorithm that calculated the $\Delta\sigma_0$ for each pre-disaster image pair and compared the highest observed change to the $\Delta\sigma_0$ of the co-disaster pair.

The assumptions made here are that the change in geometrical features in a SAR resolution cell due to the collapsing of a building dominates the backscattering intensity and can therefore be measured as a change in the σ_0 value. This is a valid assumption due to the relative larger size of buildings compared to other surface features that reflect the incoming radar signal. The change in the backscattering intensity due to building damage is assumed to be larger than changes in the backscattering intensity due to natural variations on the surface. Therefore, the decrease or increase of the backscattering intensity that can be caused by a damaged building should be compared to the highest observed $\Delta\sigma_0$ in the pre-disaster signal. Finally, the vegetated and water areas are masked in the damage detection maps using Landsat imagery in the Earth Engine, as these areas are not of interest to the search and rescue teams and might even hamper an efficient interpretation of the results.

2. How does this damage detection algorithm perform in a rapid disaster response situation after earthquakes and intentional damage in conflict areas?

The gradient approach has been applied to three case studies (2016 Central Italy earthquake, 2017 Mexico Earthquake and 2018 Syria military strikes) in order to determine the operability of the algorithm in a rapid disaster response situation. Based on the location and date of the disaster, the algorithm automatically gathers and processes the data to generate a change detection map of potentially damaged buildings for an area of 90.000 km^2 . If no new post-disaster acquisition is available the algorithm will present an approximation of when the new acquisition will be available, which is useful information for rescue teams. The approximation of a new acquisition date is based on the revisit time of the Sentinel-1 mission for the area of interest and the relative orbit the next expected acquisition will belong to. By evaluating the three case studies, it is shown that the change detection algorithm performs really well in a rapid disaster response situation for both earthquakes and intentional damage. The correct data is selected and processed, which then can be interpreted by rescue workers.

The accuracy of the change detection algorithm for damaged buildings, however, can still be improved. In the Amatrice case study it could be observed from damage grading maps that a large part of the old city center collapsed, whereas the algorithm detected changes in the backscattering intensity and indicated them as clusters of colored pixels. Although not the entire damaged part of the city center was detected, the area could be interpreted in the damage detection map as an area consisting of damaged buildings through observing the larger concentration of small clusters of severely changed pixels. These clusters of changed pixels were caused by several individual buildings that suffered from the earthquake and caused a significant change in the intensity. However, for the Mexico City case study where individual buildings collapsed instead of an entire building block, the damage detection was less obvious. Some smaller clusters of severely changed pixels matched nicely with locations of building collapse but also some damaged buildings were not identified by the change detection algorithm. This is concerning as these buildings may be easily missed by search and rescue operations when the prioritization would be based only on this map. About 50% of the locations of severely damaged buildings (EMS95 grades 4 and 5) were detected by the algorithm. From the Syria case study it can be concluded that this proposed algorithm can also be used for damage detection due to bomb-

ings. Note that the spatial extent of the damaged structures must be at least equal to or larger than the spatial resolution of the GRD data for it to be detectable. For structures that were larger than the GRD spatial resolution and suffered from severe building damage the damage detection algorithm worked extremely well, correctly and clearly indicating the damaged structure.

3. Are the resulting building damage maps sufficiently informative and useful for rescue operation teams in their planning and rescue work?

The results have been presented to the Urban Search And Rescue team of the Netherlands, which are operational within 24h-72h after a disaster in the affected country and have a long tradition in offering help in search and rescue operations. They saw great potential for a system as presented here as it is easy to operate, freely available and fast in processing which makes it ideal to assist in wide-area situation awareness operations. Note that the fast processing holds only for the algorithm. Data latency from the moment of the disaster to an acquisition actually being available is dependent on the revisit time of the satellite (0h-72h), the downlinking and processing of the raw data to a GRD image by ESA (on average 5.5h) and the downloading of GRD imagery from the SciHub and post-processing by the Earth Engine (max. of 48h). The data latency due to the revisit time of the satellite is the main disadvantage of damage detection through spaceborne based remote sensing data, as this cannot be influenced or decreased. In the meantime, usable optical or SAR data from other satellite missions may be used or UAVs and airplanes with remote sensing systems can be operated. The data latency on ESA's side will be decreased significantly once the European Data Relay System is operational. This system, nicknamed the SpaceDataHighway, provides data relay between low orbiting satellites and the European Data Relay System nodes over optical links, with the information sent down to Europe in near-real time. This would save around 1.5 hours on ESA's data latency side. Finally, the data latency due to the post-processing by the Earth Engine is already on average lower than the two days as stated before and said to be decreased significantly. Unfortunately, no statistics are available on this part. Although the Earth Engine developers are very easily accessible and open for feedback, this also illustrates the downside of working in, and hence depending on, the Earth Engine.

5.2. Conclusion

All in all, the Sentinel-1 GRD imagery available in the Earth Engine can be used to assist in damage detection during rapid response situations. It is easy to operate as the only two input parameters are the date and location of the disaster, freely available for non-profit and academic organizations and fast in processing once the GRD imagery is available in the Earth Engine repository. The proposed damage detection algorithm performs well over areas where multiple buildings collapsed within an urban environment, but has more difficulties with detecting individual collapsed buildings within a dense urban area as some collapsed buildings are not detected by the algorithm. Individual damaged structures are well detected in less dense urban environments, assuming the spatial extent of the structures is larger than the spatial resolution of the GRD imagery. The resulting damage detection maps as presented here are informative and useful for rescue operation teams, specifically in the prioritization of operations right after the disaster. Furthermore, if the maps are made available quickly after the disaster they could also be used as an additional information source in the decision making process of the USAR team. Other users for these damage detection maps in rapid disaster response situations may be insurance companies that need to make an estimate of the amount of damage in the area. And to put the resulting damage detection system in an even broader perspective, it can be applied to any situation where there is a need for change detection when only one post-event acquisition is available and the co-event pixel change is expected to be larger than any pre-event change observed for that same pixel.

It is important for rescue teams using the maps to understand that the detected pixels in an urban environment indicate a change in the backscattering intensity which is assumed to be related to building damage (correctly classified), but might be caused by natural variations in the intensity (false positively classified). Also, some damaged building might remain undetected by the algorithm (false negatively classified) making it more reliable if the prioritization of an area is based on the density of detected pixels and scan that sector as a whole instead of only visiting the locations identified in the damage detection map. Keeping this in mind, the proposed approach can definitely be of use in rapid disaster response situations and be operated as an additional damage detection system next to the already existing and operational organizations.

5.3. Recommendations

As the dependence on the Google Earth Engine developers showed some negative aspects, it might in that sense be better to build an individual database with Sentinel-1 SAR and Landsat or Sentinel-2 data to perform the same operations on. One could then also decide to use the SLC format with full resolution instead of the GRD format, as then the phase and intensity can both be evaluated and possibly used for multi-temporal damage detection approaches. Moreover, ancillary data sources such as the type of buildings and the population density as introduced in section 1.3 might be useful contextual information for search and rescue teams. The resulting damage detection map could then also be incorporated in the Common Operational Picture, a software tool to visualize real-time search and rescue operations and additional datasets that improve wide-situational awareness, such as the damage detection map presented here, that is being developed by INACHUS. In that way, rescue workers can always access the map and access the locations of potentially damaged buildings to check whether this really is the case and if help is needed. More generally, the entire approach may be offered to the International Charter Space and Disasters so that it could be incorporated in their data stream. Note that setting up such a system is very time consuming and needs to be done professionally if search and rescue teams would really want to depend on this system in their activities.

Recommendations for this approach in particular are to fully automate the algorithm by linking it to the USGS seismic alert and automatically start the algorithm when an earthquake that exceeds a certain magnitude occurs. From here on, the algorithm could continuously check for a new available post-disaster acquisition and continue from there on. Additionally, concerning the post-disaster date calculation, the data latency due to the processing from raw data to GRD imagery by ESA and ingesting the data in the Google Earth Engine repository should be accurately estimated and incorporated in the calculation in order to give a proper estimation of when the next acquisition is also available for processing. Improvements in accurate damage detection can be made by either processing the data on a building-block scale which decreases the spatial resolution and hence the possibility to detect individual buildings but would possibly improve on false positive and false negative classifications, or applying different algorithms on a multi-temporal timeseries such as the correlation coefficient as discussed in section 2.3.3. Finally, the algorithm could be offered to the Google Earth Engine developers for incorporation in their standard set of algorithms they host in their archive.

5.4. Outlook

Several insights that might significantly alter the area of rapid disaster response using SAR data will be shortly presented here. First, machine learning is a technique that is rapidly growing and being applied to various areas of research. It would be interesting to see whether it could also be of use for more accurate damage detection through change detection algorithms. Nowadays, a change detection approach is applied to every pixel without making a distinction between all the pixels. By evaluating the timeseries of each pixel individually or as groups in a fast way through machine learning, pixels might be treated separately and various change detection algorithms are applied on various pixels based on their behavior. This would make the change detection algorithm more dynamic and might improve the accuracy of the damage detection.

More on the data latency part on EE's side, improvements could be made by directly linking the processing servers of ESA to the data repository of the Earth Engine for even faster data availability. This, however, is most likely hard due to conflicting interests. An alternative would therefore be to explore the Thematic Exploration Platform hosted by ESA. Regarding geohazards the platform already offers multiple remote sensing datasets such as Sentinel-1 and Landsat imagery for geohazard monitoring and disaster prevention. The damage detection system presented in this research could be incorporated in the Thematic Exploration Platform as well. Because the Sentinel-1 mission and the platform are both hosted by ESA it may be assumed that the ingestion of the newly acquired Sentinel-1 acquisitions in the platform archive is done more rapidly compared to the ingestion from the acquisitions in the EE right now.

Finally, the launch of the NASA-ISRO Synthetic Aperture Radar mission which is planned for 2021 might result in additional outcomes to the area of spaceborne based damage detection. This satellite mission will be equipped with an L- and S-band SAR instrument. The measured backscattering signal by these instruments might react differently to the same type and severity of building damage, which can then be compared with the results from the C-band instrument on the Sentinel-1 mission. This could lead to new insights or relations between building damage and the backscattering signal. Most importantly, the satellite system will also aim for a revisit time of 12 days and provide data through an open-data policy. This might offer the choice between either the NISAR satellite or the Sentinel-1 mission to apply a change detection algorithm on when one or the other already has a post-disaster acquisition and the other does not.

Bibliography

- [1] Ajadi, O. A., Meyer, F. J., and Webley, P. W. Change detection in synthetic aperture radar images using a multiscale-driven approach. *Remote Sensing*, 8(6):482, 2016.
- [2] Ali, I., Cao, S., Naeimi, V., Paulik, C., and Wagner, W. Methods to remove the border noise from sentinel-1 synthetic aperture radar data: Implications and importance for time-series analysis. *IEEE Journal of Selected Topics in Applied Earth Observations and Remote Sensing*, 2018.
- [3] American Red Cross. Drones for disaster response and relief operations. Technical report, Apr 2015. URL www.issuelab.org/resources/21683/21683.pdf.
- [4] Arciniegas, G. A., Bijker, W., Kerle, N., and Tolpekin, V. A. Coherence-and amplitude-based analysis of seismicogenic damage in bam, iran, using envisat asar data. *IEEE Transactions on Geoscience and Remote Sensing*, 45(6):1571–1581, 2007.
- [5] Argenti, F., Lapini, A., Bianchi, T., and Alparone, L. A tutorial on speckle reduction in synthetic aperture radar images. *IEEE Geoscience and remote sensing magazine*, 1(3):6–35, 2013.
- [6] Balz, T. and Liao, M. Building-damage detection using post-seismic high-resolution sar satellite data. *International Journal of Remote Sensing*, 31(13):3369–3391, 2010.
- [7] Bamler, R. and Hartl, P. Synthetic aperture radar interferometry. *Inverse problems*, 14(4):R1, 1998.
- [8] Bartels, S. A. and VanRooyen, M. J. Medical complications associated with earthquakes. *The Lancet*, 379(9817):748–757, 2012.
- [9] Boulogne, M. private communication, May 9 2018.
- [10] Bourbigot, M. Sentinel-1 product specification. Technical report, Oct 14 2016. URL https://sentinel.esa.int/documents/247904/349449/Sentinel-1_Product_Specification.
- [11] Brackman, A. Raboso earthquake response - september 2017, Oct 18 2017. URL <https://aria.jpl.nasa.gov/node/62>.
- [12] Bürgmann, R., Rosen, P. A., and Fielding, E. J. Synthetic aperture radar interferometry to measure earth's surface topography and its deformation. *Annual review of earth and planetary sciences*, 28(1):169–209, 2000.
- [13] Câmara, D. Cavalry to the rescue: Drones fleet to help rescuers operations over disasters scenarios. In *Antenna Measurements & Applications (CAMA), 2014 IEEE Conference on*, pages 1–4. IEEE, 2014.
- [14] Castro, J. How long can a person survive under earthquake debris?, 2011. URL <https://www.livescience.com/16747-earthquake-rubble-survival.html>.
- [15] Chouet, B. A. Long-period volcano seismicity: its source and use in eruption forecasting. *Nature*, 380(6572):309, 1996.
- [16] Coburn, A., Pomonis, A., and Spence, R. Reducing human casualties in building collapse methods of optimising disaster plans to reduce injury levels. *Project Final Report, SERC*, 1992.
- [17] Collecte Localisation Satellites. Masking “no-value” pixels on GRD products generated by the Sentinel-1 ESA IPF. *Collecte Localisation Satellites, Tech. Rep. 3, CLS-2015*, 2016.
- [18] Corbane, C., Saito, K., Dell’Oro, L., Bjorgo, E., Gill, S. P., Emmanuel Piard, B., Huyck, C. K., Kemper, T., Lemoine, G., Spence, R. J., et al. A comprehensive analysis of building damage in the 12 january 2010 mw7 haiti earthquake using high-resolution satellite and aerial imagery. *Photogrammetric Engineering & Remote Sensing*, 77(10):997–1009, 2011.

- [19] Dana, R. A. and Knepp, D. L. The impact of strong scintillation on space based radar design ii: Noncoherent detection. *IEEE transactions on aerospace and electronic systems*, (1):34–46, 1986.
- [20] Davenport, W. and Root Jr, W. An introduction to the theory of random signals and noise. *IEEE Press, New York*, 1987.
- [21] De Zan, F. and Guarnieri, A. M. Topsar: Terrain observation by progressive scans. *IEEE Transactions on Geoscience and Remote Sensing*, 44(9):2352–2360, 2006.
- [22] Delignon, Y., Garello, R., and Hillion, A. Statistical modelling of ocean sar images. *IEE Proceedings-Radar, Sonar and Navigation*, 144(6):348–354, 1997.
- [23] DeVore, M. D., Lanterman, A. D., and O’Sullivan, J. A. Atr performance of a rician model for sar images. In *Automatic Target Recognition X*, volume 4050, pages 34–46. International Society for Optics and Photonics, 2000.
- [24] Dong, L. and Shan, J. A comprehensive review of earthquake-induced building damage detection with remote sensing techniques. *ISPRS Journal of Photogrammetry and Remote Sensing*, 84:85–99, 2013.
- [25] Doswell III, C. A., Brooks, H. E., and Maddox, R. A. Flash flood forecasting: An ingredients-based methodology. *Weather and Forecasting*, 11(4):560–581, 1996.
- [26] Erdelj, M. and Natalizio, E. Uav-assisted disaster management: Applications and open issues. In *Computing, Networking and Communications (ICNC), 2016 International Conference on*, pages 1–5. IEEE, 2016.
- [27] Erdelj, M., Natalizio, E., Chowdhury, K. R., and Akyildiz, I. F. Help from the sky: Leveraging uavs for disaster management. *IEEE Pervasive Computing*, 16(1):24–32, 2017.
- [28] ESA. Sentinel-1 technical guide, 2016. URL <https://earth.esa.int/web/sentinel/technical-guides/sentinel-1-sar>.
- [29] ESA. Sentinel-2 cloud mask, 2017. URL <https://sentinel.esa.int/web/sentinel/technical-guides/sentinel-2-msi/level-1c/cloud-masks>.
- [30] ESA/ATG. Sentinel-1 radar vision, 2014. URL https://www.esa.int/spaceinimages/Images/2014/01/Sentinel-1_radar_vision.
- [31] Fielding, E. J., Talebian, M., Rosen, P. A., Nazari, H., Jackson, J. A., Ghorashi, M., and Walker, R. Surface ruptures and building damage of the 2003 bam, iran, earthquake mapped by satellite synthetic aperture radar interferometric correlation. *Journal of Geophysical Research: Solid Earth*, 110(B3), 2005.
- [32] Foga, S., Scaramuzza, P. L., Guo, S., Zhu, Z., Dille, R. D., Beckmann, T., Schmidt, G. L., Dwyer, J. L., Hughes, M. J., and Laue, B. Cloud detection algorithm comparison and validation for operational land-sat data products. *Remote sensing of environment*, 194:379–390, 2017.
- [33] Fowler, C. *The Solid Earth*. Cambridge University Press, 1990.
- [34] Gamba, P., Dell’Acqua, F., and Trianni, G. Rapid damage detection in the bam area using multitemporal sar and exploiting ancillary data. *IEEE Transactions on Geoscience and Remote Sensing*, 45(6):1582–1589, 2007.
- [35] Gao, G. Statistical modeling of sar images: A survey. *Sensors*, 10(1):775–795, 2010.
- [36] Gatelli, F., Guarnieri, A. M., Parizzi, F., Pasquali, P., Prati, C., and Rocca, F. The wavenumber shift in sar interferometry. *IEEE Transactions on Geoscience and Remote Sensing*, 32(4):855–865, 1994.
- [37] George, S. F. The detection of nonfluctuating targets in log-normal clutter. Technical report, NAVAL RESEARCH LAB WASHINGTON DC, 1968.
- [38] Goodman, J. W. Statistical properties of laser speckle patterns. In *Laser speckle and related phenomena*, pages 9–75. Springer, 1975.

- [39] Google. Sentinel-1 preprocessing article, 2016. URL <https://developers.google.com/earth-engine/sentinel1>.
- [40] Google. Sentinel-2 multispectral instrument, 2016. URL <https://explorer.earthengine.google.com/#detail/COPERNICUS%2FS2>.
- [41] Google. Developer's guide google earth engine, 2017. URL <https://developers.google.com/earth-engine/>.
- [42] Google. Usgs landsat 8 surface reflectance in the gee, 2017. URL https://explorer.earthengine.google.com/#detail/LANDSAT%2FLC08%2FC01%2FT1_SR.
- [43] Gorelick, N., Hancher, M., Dixon, M., Ilyushchenko, S., Thau, D., and Moore, R. Google earth engine: Planetary-scale geospatial analysis for everyone. *Remote Sensing of Environment*, 202:18–27, 2017.
- [44] Grunthal, G., Musson, R., Schwarz, J., and Stucchi, M. *European Macroseismic Scale 1998*, 1998.
- [45] Guarnieri, A. M. *Introduction to RADAR*, Mar 2013.
- [46] Hanssen, R. F. *Radar interferometry: data interpretation and error analysis*, volume 2. Springer Science & Business Media, 2001.
- [47] Hoen, E. W. and Zebker, H. A. Penetration depths inferred from interferometric volume decorrelation observed over the greenland ice sheet. *IEEE Transactions on Geoscience and Remote Sensing*, 38(6): 2571–2583, 2000.
- [48] Hoffmann, J. Mapping damage during the bam (iran) earthquake using interferometric coherence. *International Journal of Remote Sensing*, 28(6):1199–1216, 2007.
- [49] Huang, Q. and Xiao, Y. Geographic situational awareness: mining tweets for disaster preparedness, emergency response, impact, and recovery. *ISPRS International Journal of Geo-Information*, 4(3):1549–1568, 2015.
- [50] Huyck, C. K., Adams, B. J., Cho, S., Chung, H.-C., and Eguchi, R. T. Towards rapid citywide damage mapping using neighborhood edge dissimilarities in very high-resolution optical satellite imagery—application to the 2003 bam, iran, earthquake. *Earthquake Spectra*, 21(S1):255–266, 2005.
- [51] Ilyushchenko, S. V. private communication, May 15 2018.
- [52] INSARAG. Insarag guidelines volume iii: Operational field guide. Technical report, February 11 2015. URL <file:///C:/Users/Gebruiker/Downloads/INSARAG%20Guidelines%20V3%252C%20Operational%20Field%20Guide.pdf>.
- [53] Joyce, K. E., Belliss, S. E., Samsonov, S. V., McNeill, S. J., and Glassey, P. J. A review of the status of satellite remote sensing and image processing techniques for mapping natural hazards and disasters. *Progress in Physical Geography*, 33(2):183–207, 2009.
- [54] Ke, Y., Im, J., Lee, J., Gong, H., and Ryu, Y. Characteristics of landsat 8 oli-derived ndvi by comparison with multiple satellite sensors and in-situ observations. *Remote Sensing of Environment*, 164:298–313, 2015.
- [55] Kuruoglu, E. E. and Zerubia, J. Modeling sar images with a generalization of the rayleigh distribution. *IEEE Transactions on Image Processing*, 13(4):527–533, 2004.
- [56] Kuttikkad, S. and Chellappa, R. Non-gaussian cfar techniques for target detection in high resolution sar images. In *Image Processing, 1994. Proceedings. ICIP-94., IEEE International Conference*, volume 1, pages 910–914. IEEE, 1994.
- [57] Laur, H. *Analyse d'images radar en télédétection: discriminateurs radiométriques et texturaux*. PhD thesis, Toulouse 3, 1989.
- [58] Li, F. K. and Goldstein, R. M. Studies of multibaseline spaceborne interferometric synthetic aperture radars. *IEEE Transactions on Geoscience and Remote Sensing*, 28(1):88–97, 1990.

- [59] Li, X., Yang, W., Ao, T., Li, H., and Chen, W. An improved approach of information extraction for earthquake-damaged buildings using high-resolution imagery. *Journal of Earthquake and Tsunami*, 5(04):389–399, 2011.
- [60] Liu, J.-h., Shan, X.-j., and Yin, J.-y. Automatic recognition of damaged town buildings caused by earthquake using remote sensing information: Taking the 2001 bhuj, india, earthquake and the 1976 tangshan, china, earthquake as examples. *Acta seismologica sinica*, 17(6):686–696, 2004.
- [61] Madsen, S. N. *Speckle theory: Modelling, analysis, and applications related to synthetic aperture radar data*. PhD thesis, 1986.
- [62] Massonnet, D. and Souyris, J.-C. *Imaging with synthetic aperture radar*. EPFL press, 2008.
- [63] Matsuoka, M. and Estrada, M. Development of earthquake-induced building damage estimation model based on alos/palsar observing the 2007 peru earthquake. *Journal of Japan Association for Earthquake Engineering*, 12(6):36–49, 2012.
- [64] Matsuoka, M. and Yamazaki, F. Use of interferometric satellite sar for earthquake damage detection. *Sat*, 2:z1, 2000.
- [65] Matsuoka, M. and Yamazaki, F. Interferometric characterization of areas damaged by the 1995 kobe earthquake using satellite sar images. In *Proceedings of the 12th World Conference on Earthquake Engineering*, volume 2, 2000.
- [66] Matsuoka, M. and Yamazaki, F. Use of satellite sar intensity imagery for detecting building areas damaged due to earthquakes. *Earthquake Spectra*, 20(3):975–994, 2004.
- [67] McFeeters, S. K. The use of the normalized difference water index (ndwi) in the delineation of open water features. *International journal of remote sensing*, 17(7):1425–1432, 1996.
- [68] Moreira, A., Prats-Iraola, P., Younis, M., Krieger, G., Hajnsek, I., and Papathanassiou, K. P. A tutorial on synthetic aperture radar. *IEEE Geoscience and remote sensing magazine*, 1(1):6–43, 2013.
- [69] Moser, G., Zerubia, J., and Serpico, S. B. Sar amplitude probability density function estimation based on a generalized gaussian model. *IEEE Transactions on Image Processing*, 15(6):1429–1442, 2006.
- [70] Murakami, H. Chances of occupant survival and sar operation in the buildings collapsed by the 1995 great hanshin earthquake, japan. In *Proc. 11th World Conf. on Earthq. Engr., Paper*, number 852, 1996.
- [71] NASA. LANDSAT 8 data users handbook. Technical report, Mar 29 2016. URL <https://landsat.usgs.gov/sites/default/files/documents/Landsat8DataUsersHandbook.pdf>.
- [72] NASA. Landsat 8 surface reflectance code (lasrc) product. Technical report, 2017. URL https://landsat.usgs.gov/sites/default/files/documents/lasrc_product_guide.pdf.
- [73] Navarro-Sanchez, V. D. and Lopez-Sanchez, J. M. Improvement of persistent-scatterer interferometry performance by means of a polarimetric optimization. *IEEE Geoscience and Remote Sensing Letters*, 9(4):609–613, 2012.
- [74] Nicolas, J.-M. and Anfinson, S. N. Introduction to second kind statistics: Application of log-moments and log-cumulants to the analysis of radar image distributions. *Trait. Signal*, 19(3):139–167, 2002.
- [75] Papoulis, A. *Systems and transforms with applications in optics*. McGraw-Hill Series in System Science, Malabar: Krieger, 1968, 1968.
- [76] Parizzi, A., Gonzalez, F. R., and Eineder, M. Study of the impact of polarization for distributed targets interferometry. In *EUSAR 2016: 11th European Conference on Synthetic Aperture Radar, Proceedings of*, pages 1–3. VDE, 2016.
- [77] Perissin, D. and Ferretti, A. Urban-target recognition by means of repeated spaceborne sar images. *IEEE Transactions on Geoscience and Remote Sensing*, 45(12):4043–4058, 2007.

- [78] Pesaresi, M., Gerhardinger, A., and Haag, F. Rapid damage assessment of built-up structures using vhr satellite data in tsunami-affected areas. *International Journal of Remote Sensing*, 28(13-14):3013–3036, 2007.
- [79] Piantanida, R., Franceschi, N., Meadows, P., and Miranda, N. Thermal denoising of products generated by the s-1 ipf, Nov 11 2017. URL <https://earth.esa.int/documents/247904/2142675/Thermal-Denoising-of-Products-Generated-by-Sentinel-1-IPF>.
- [80] Pipia, L., Fabregas, X., Aguasca, A., Lopez-Martinez, C., Duque, S., Mallorqui, J. J., and Marturia, J. Polarimetric differential sar interferometry: First results with ground-based measurements. *IEEE Geoscience and Remote Sensing Letters*, 6(1):167–171, 2009.
- [81] Plank, S. Rapid damage assessment by means of multi-temporal sar—a comprehensive review and outlook to sentinel-1. *Remote Sensing*, 6(6):4870–4906, 2014.
- [82] Polli, D., Dell’Acqua, F., Gamba, P., and Lisini, G. Earthquake damage assessment from post-event only radar satellite data. In *Proceedings of the Eighth International Workshop on Remote Sensing for Disaster Response, Tokyo, Japan*, volume 30, 2010.
- [83] Raney, R. K. Radar fundamentals: technical perspective. *Principals and Applications of Imaging Radar, Manual of Remote Sensing*, 2:9–130, 1998.
- [84] Rodriguez, E. and Martin, J. Theory and design of interferometric synthetic aperture radars. In *IEE Proceedings F (Radar and Signal Processing)*, volume 139, pages 147–159. IET, 1992.
- [85] Rosen, P. A., Hensley, S., Zebker, H. A., Webb, F. H., and Fielding, E. J. Surface deformation and coherence measurements of kilauea volcano, hawaii, from sir-c radar interferometry. *Journal of Geophysical Research: Planets*, 101(E10):23109–23125, 1996.
- [86] Rosen, P. A., Hensley, S., Joughin, I. R., Li, F. K., Madsen, S. N., Rodriguez, E., and Goldstein, R. M. Synthetic aperture radar interferometry. *Proceedings of the IEEE*, 88(3):333–382, 2000.
- [87] Roser, M. and Ritchie, H. Natural Catastrophes published online at ourworldindata.org, 2018. URL <https://ourworldindata.org/natural-catastrophes/>.
- [88] Sarti, F. Reminder about sar, rosa/esa/dlr course, 2009. URL http://earth.esa.int/download/eoedu/Earthnet-website-material/to-access-from-Earthnet/2009_ROSA-ESA-DLR-Radar-Remote-Sensing-Course/SAR%20theory%20and%20apps%20-%20Reminder.pdf.
- [89] Statheropoulos, M., Agapiou, A., Pallis, G., Mikedi, K., Karma, S., Vamvakari, P. J., Dandoulaki, M., Andritsos, F., and Thomas, C. Factors that affect rescue time in urban search and rescue (usar) operations. 75, 01 2015.
- [90] Stocks, B. J., Lynham, T., Lawson, B., Alexander, M., Wagner, C. V., McAlpine, R., and Dube, D. Canadian forest fire danger rating system: an overview. *The Forestry Chronicle*, 65(4):258–265, 1989.
- [91] Stramondo, S., Bignami, C., Chini, M., Pierdicca, N., and Tertulliani, A. Satellite radar and optical remote sensing for earthquake damage detection: results from different case studies. *International Journal of Remote Sensing*, 27(20):4433–4447, 2006.
- [92] Suhet. Sentinel-1 user handbook, 2013. URL <https://sentinel.esa.int/web/sentinel/user-guides/sentinel-1-sar>.
- [93] Suhet. Sentinel-2 user handbook, Jul 27 2015. URL https://sentinel.esa.int/documents/247904/685211/Sentinel-2_User_Handbook.
- [94] Szajnowski, W. Estimators of log-normal distribution parameters. *IEEE Transactions on Aerospace and Electronic Systems*, (5):533–536, 1977.

- [95] Tapete, D. and Cigna, F. Urban remote sensing in areas of conflict: Terrasar-x and sentinel-1 change detection in the middle east. In *Fourth International Conference on Remote Sensing and Geoinformation of the Environment (RSCy2016)*, volume 9688, page 968821. International Society for Optics and Photonics, 2016.
- [96] Taskin Kaya, G., Musaoglu, N., and Ersoy, O. K. Damage assessment of 2010 haiti earthquake with post-earthquake satellite image by support vector selection and adaptation. *Photogrammetric Engineering & Remote Sensing*, 77(10):1025–1035, 2011.
- [97] Tison, C., Nicolas, J., and Tupin, F. Accuracy of fisher distributions and log-moment estimation to describe amplitude distributions of high resolution sar images over urban areas. In *Geoscience and Remote Sensing Symposium, 2003. IGARSS'03. Proceedings. 2003 IEEE International*, volume 3, pages 1999–2001. IEEE, 2003.
- [98] Tison, C., Nicolas, J.-M., Tupin, F., and Maître, H. A new statistical model for markovian classification of urban areas in high-resolution sar images. *IEEE transactions on geoscience and remote sensing*, 42(10): 2046–2057, 2004.
- [99] Torres, R., Snoeij, P., Geudtner, D., Bibby, D., Davidson, M., Attema, E., Potin, P., Rommen, B., Floury, N., Brown, M., et al. Gmes sentinel-1 mission. *Remote Sensing of Environment*, 120:9–24, 2012.
- [100] Usai, S. The use of man-made features for long time scale insar. In *Geoscience and Remote Sensing, 1997. IGARSS'97. Remote Sensing-A Scientific Vision for Sustainable Development., 1997 IEEE International*, volume 4, pages 1542–1544. IEEE, 1997.
- [101] Usai, S. and Hanssen, R. Long time scale insar by means of high coherence features. *European Space Agency-Publications-Esa Sp*, 414:225–228, 1997.
- [102] USAR. Yearly meeting of the urban search and rescue team of the netherlands. private communication, Dec 2015.
- [103] Van Leijen, F. J. *Persistent scatterer interferometry based on geodetic estimation theory*. PhD thesis, 2014.
- [104] Voigt, S., Schneiderhan, T., Twele, A., Gähler, M., Stein, E., and Mehl, H. Rapid damage assessment and situation mapping: learning from the 2010 haiti earthquake. *Photogrammetric Engineering and Remote Sensing (PE&RS)*, 77(9):923–931, 2011.
- [105] Vu, T. T., Matsuoka, M., and Yamazaki, F. Detection and animation of damage using very high-resolution satellite data following the 2003 bam, iran, earthquake. *Earthquake Spectra*, 21(S1):319–327, 2005.
- [106] Xia, Z.-G. and Henderson, F. M. Understanding the relationships between radar response patterns and the bio-and geophysical parameters of urban areas. *IEEE Transactions on Geoscience and Remote Sensing*, 35(1):93–101, 1997.
- [107] Yagüe-Martínez, N., Prats-Iraola, P., González, F. R., Brcic, R., Shau, R., Geudtner, D., Eineder, M., and Bamler, R. Interferometric processing of sentinel-1 tops data. *IEEE Transactions on Geoscience and Remote Sensing*, 54(4):2220–2234, 2016.
- [108] Yun, S.-H., Hudnut, K., Owen, S., Webb, F., Simons, M., Sacco, P., Gurrola, E., Manipon, G., Liang, C., Fielding, E., et al. Rapid damage mapping for the 2015 mw 7.8 gorkha earthquake using synthetic aperture radar data from cosmo-skymed and alos-2 satellites. *Seismological Research Letters*, 86(6): 1549–1556, 2015.
- [109] Zebker, H. A. and Villasenor, J. Decorrelation in interferometric radar echoes. *IEEE Transactions on geoscience and remote sensing*, 30(5):950–959, 1992.

A

Damage Detection Maps

A.1. Case Study 1: Amatrice, M6.2 2016 Central Italy Earthquake

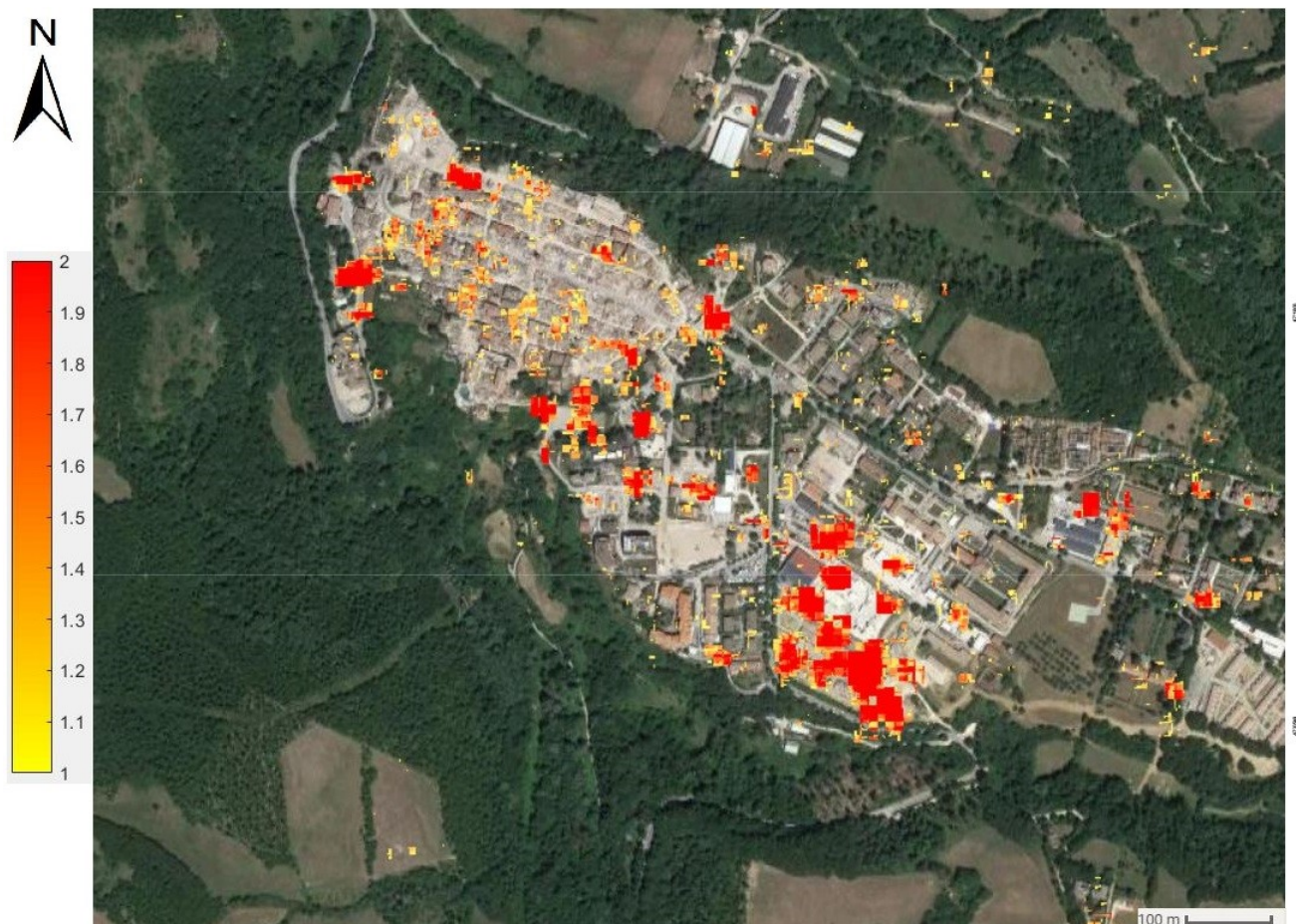


Figure A.1: Results of the gradient approach damage detection algorithm for the city of Amatrice after the M6.2 2016 Central-Italy earthquake. Pixels that qualify as non-vegetated (yearly maximum NDVI lower than 0.8) and non-water (yearly median NDWI lower than 0.5) have been colored in the range yellow to red when the ratio between the observed co-disaster change in σ_0 and highest observed change in σ_0 is in the range of 1.0 to 2.0.

A.2. Case Study 2: Mexico City, M7.8 2017 Central-Mexico Earthquake

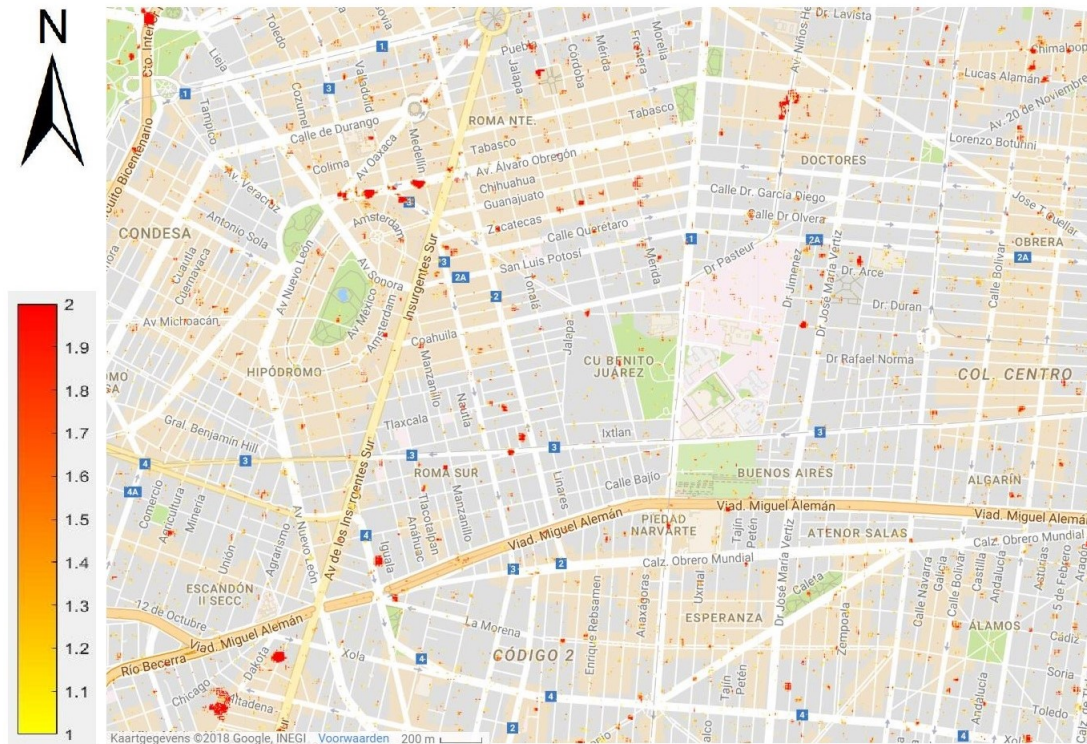


Figure A.3: Results of the gradient approach damage detection algorithm for Mexico-City after the M7.1 Central-Mexico earthquake (2017). Pixels that qualify as non-vegetated (yearly maximum NDVI lower than 0.8) and non-water (yearly median NDWI lower than 0.5) have been colored in the range yellow to red when the ratio between the observed co-disaster change in σ_0 and highest observed change in σ_0 is in the range of 1.0 to 2.0.

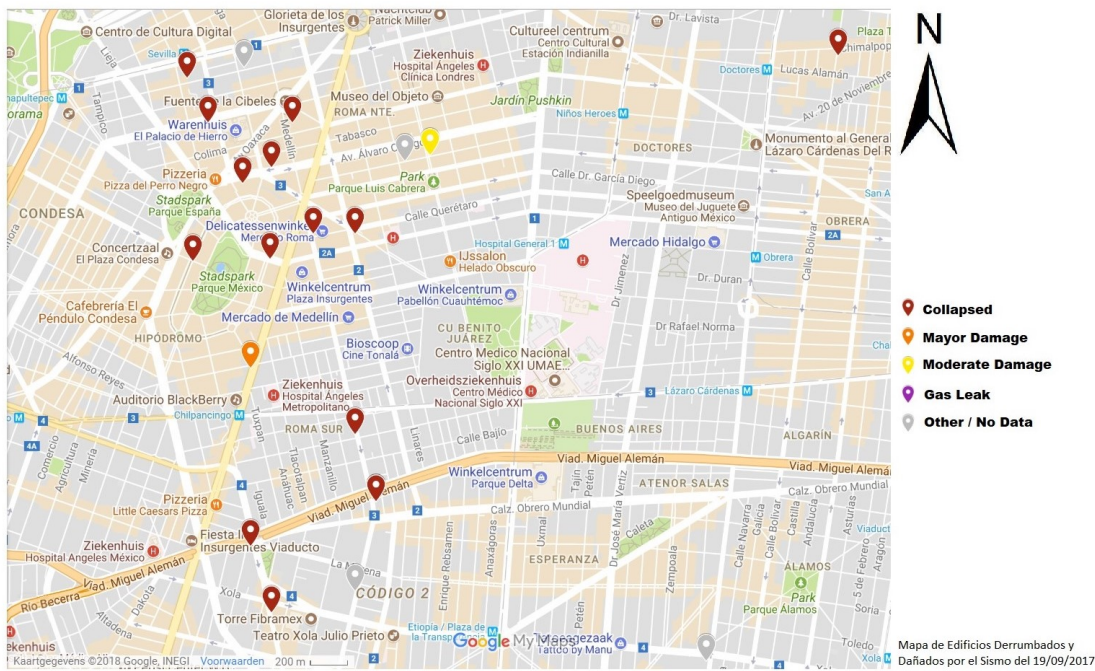


Figure A.4: A crowd-sourced Google map indicating collapsed and damaged buildings which has been used as validation. The crowd-sourced map is obtained from https://www.google.com/maps/d/u/0/viewer?mid=1_-V971bdgLFPx-CtqhLW1JAnYY&ll=19.415634726751634%2C-99.16466053928525&z=15.

A.3. Case Study 3: Damascus and Homs, Syria Military Strikes

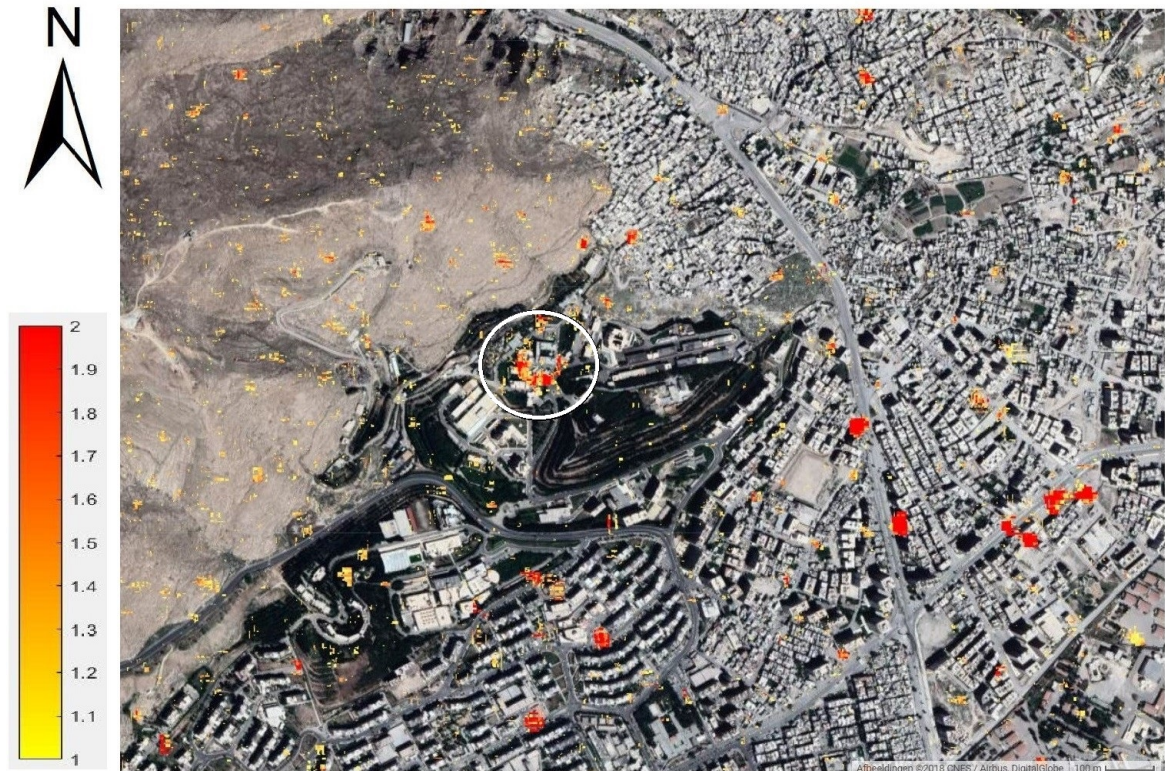


Figure A.5: Results of the gradient approach damage detection algorithm for the military strike of the Barzah Research and Development Center in Damascus, indicated by the white circle. Pixels that qualify as non-vegetated (yearly maximum NDVI lower than 0.8) and non-water (yearly median NDWI lower than 0.5) have been colored in the range yellow to red when the ratio between the observed co-disaster change in σ_0 and highest observed change in σ_0 is in the range of 1.0 to 2.0.

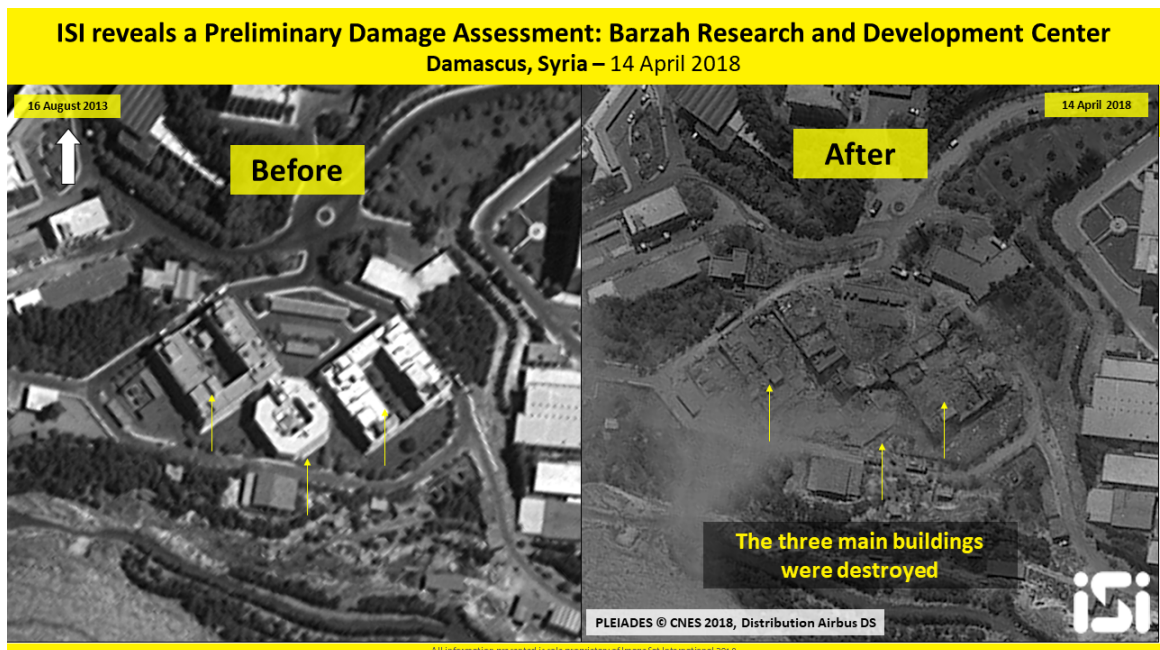


Figure A.6: Image Sat International optical data of the bombed Damascus Scientific Research Center, acquired by the Pleiades satellite.

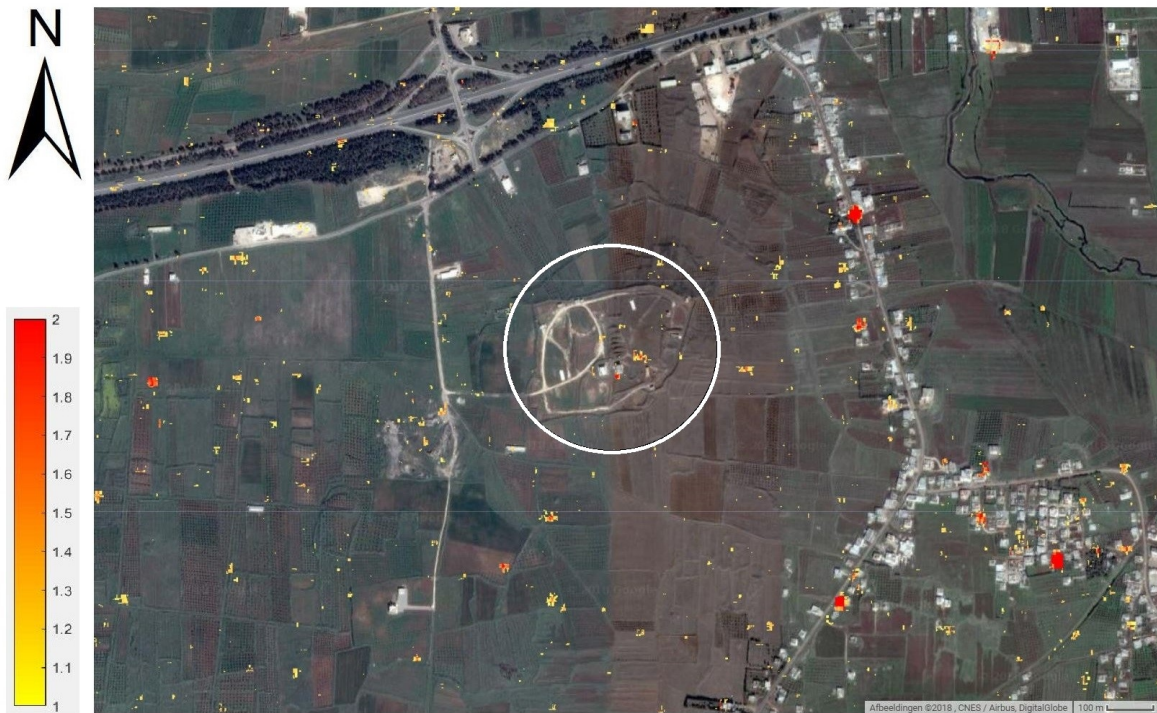


Figure A.7: Results of the gradient approach damage detection algorithm for the military strike of the Him Shinshar Chemical Weapons Storage Facility near Homs, indicated by the white circle. Pixels that qualify as non-vegetated (yearly maximum NDVI lower than 0.8) and non-water (yearly median NDWI lower than 0.5) have been colored in the range yellow to red when the ratio between the observed co-disaster change in σ_0 and highest observed change in σ_0 is in the range of 1.0 to 2.0.



Figure A.8: U.S. Department of Defence imagery showing the effects of the military strike on the Him Shinshar Chemical Weapons Storage Facility near Homs, which has been used as validation of the damage detection algorithm.



Figure A.9: Results of the gradient approach damage detection algorithm for the military strike of the Him Shinshar Chemical Weapons Bunker near Homs, indicated by the white circle. Pixels that qualify as non-vegetated (yearly maximum NDVI lower than 0.8) and non-water (yearly median NDWI lower than 0.5) have been colored in the range yellow to red when the ratio between the observed co-disaster change in σ_0 and highest observed change in σ_0 is in the range of 1.0 to 2.0.

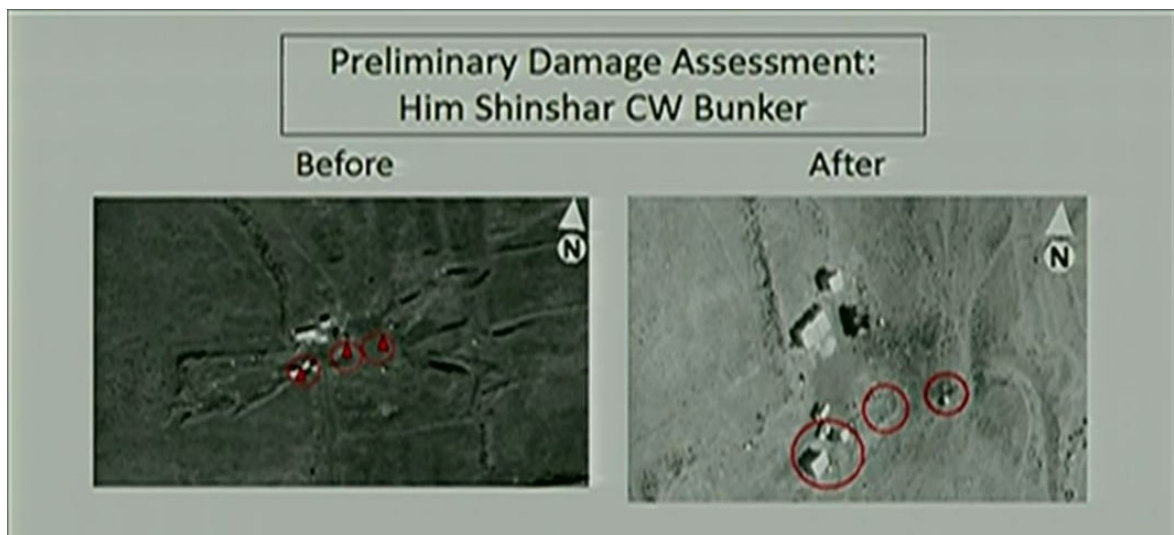


Figure A.10: U.S. Department of Defence imagery showing the effects of the military strike on the Him Shinshar Chemical Weapons Bunker near Homs, which has been used as validation of the damage detection algorithm.

B

User Manual

This section will present a manual in case a disaster would happen and the search and rescue teams would like to use the damage detection algorithm presented in this research. This manual will discuss how to operate the algorithm, how the result can be used, what data latency can be expected and what to do if no post-disaster acquisition is available. For simplicity, the disaster will be represented by an earthquake and the operability will be explained related to the procedures of the USAR team of The Netherlands (Boulogne [2018]). An overview of the steps is presented in figure B.1 and the steps are explained in more detail in this section.

Preparation

In the case a large earthquake strikes anywhere on Earth, the USGS sends out a warning containing the magnitude and epicentre of the earthquake. This information is manually checked by the USAR team and from there onwards they have to wait for a request from the struck country and approval by the steering group of the ministries of Internal Affairs, External Affairs and Defence to start offer help. In the meantime the 62 members of the USAR team are alerted and prepared for action. Once permission has been given by the steering group the team leaves the country and arrives at the region of the disaster within 24 to 72 hours after the earthquake hit. The first task of any search and rescue group in a disaster area is the Assessment, Search and Rescue Level 1 where the size of the disaster is estimated and the area is divided in sectors to maintain overview, identify possible hazards and prioritize tasks for a plan of action. Within this first level, the damage detection algorithm proposed in this research can be immediately put to use once the location and date are known. With this information, one should visit https://code.earthengine.google.com/?accept_repo=users/jeroenvheyningen/Open which accesses the Google Earth Engine Code Editor (figure 3.1). In the `Damage_General` script, the input parameters can be inserted and processed by the algorithm once Run is pressed.

Google Earth Engine

The Google Earth Engine is used in this research to develop and operate the damage detection algorithm using the Sentinel-1 GRD imagecollection that is present on the GEE database. Additionally, other datasets have been explored and put to use in order to improve the algorithm. Imagery and data from other tools may be imported into the Earth Engine for analysis and any analysis performed in the EE can be downloaded for use by other tools. Also, requests may be made so that additional datasets can be added. Lastly, one may upload their own raster data (for example GeoTIFF files) to the EE for analysis. Vector data may be loaded into Google Fusion Tables and accessed in the Earth Engine. EE also provides tools for communication and improvement as you may join the Developers list where Earth Engine staff and other Earth Engine users answer questions about eachother's scripts. Approximately once a year, generally in early December, Google opens up EE Research Awards for proposals. Additionally they frequently give EE trainings, which are typically announced on the Developer's list. These include the annual EE User Summit and the Geo for Good conference, typically held at the Googleplex in Mountain View, CA. Obviously, sharing results and analysis scripts will benefit the community, which can be done directly with other EE users through EE tools, or may be downloaded and shared like any other data.

Operating

Pressing the Run button in the Google Earth Engine initiates the algorithm to gather the available VV polarized, High resolution Sentinel-1 GRD imagery in IW mode from the very first image to the most recent image acquired over the area of interest. In case no post-disaster acquisition is available yet for both ascending and descending orbits, a notification is generated that shows an approximation of the date for the next acquisitions in ascending and descending orbits after which the algorithm is terminated. If for either one of the orbits a new acquisition is available, the script continues while giving a notification that the damage detection results may be less accurate when using acquisitions from only one of the orbits due to geometrical complications between the incoming signal and the building orientation as depicted in figure 3.4. The date of the next acquisition is not the date of the acquisition available for processing as the data latency can be caused by either the processing of the GRD imagery by ESA or the downloading from SciHub and post-processing of the data by the GEE. The processing of the raw SAR data to Level-1 GRD imagery by the ESA is always done within 24 hours after acquisition. However, on an operational basis this is generally reduced to only a few hours with an average of 5.5 hours. Last, there is the data latency caused by the downloading of the GRD imagery from SciHub and the post-processing by the GEE before it can be inserted in their own data archive. The GEE aims at performing this within 48 hours after it being made available on SciHub, but this is generally also done faster. Unfortunately, no statistics on this part are available according to Ilyushchenko [2018]. This would lead to a cumulative maximum data latency of 72 hours after the acquisition has been made, which is within the maximal time it would take for the USAR team to arrive in the affected country.

The algorithm can be repeatedly operated until a post-disaster image is available. If this is the case, based on the point given as input the most recent imagery that has a proper coverage of the AOI (for both directions) is selected and the relative orbit numbers are extracted. From here on, the ascending and descending imagecollections can be filtered on their specific relative orbit numbers so that the latest acquired image can be compared with pre-disaster imagery that has been observed under similar conditions. What results is a pre-disaster imagecollection and a post-disaster image for each orbital direction. As an intermediate step, Landsat 8 imagery is imported and filtered for the AOI and data range of January 1 2015 to the most recently acquired imagery. From this dataset a mask is generated that detects vegetated areas, which will be used later on in the processing to focus the damage detection results on urban areas for easier interpretation.

After this, the change detection algorithm is applied. For the pre-disaster timeseries the change in σ_0 is calculated for each image pair, as well as for the co-disaster image pair. Then, depending on whether the $\Delta\sigma_0$ of the co-disaster image pair has increased or decreased, the ratio is calculated between the $\Delta\sigma_0$ of the co-disaster pair and the highest positive or lowest negative $\Delta\sigma_0$ of the pre-disaster image pairs. Once this ratio exceeds the value of 1.0, the pixel is indicated as "changed" and is coloured a range of yellow to red scaled to the value of the ratio from 1.0 to 2.0, respectively. The results from the ascending and descending orbits are then combined to one final damage detection map, where the vegetation is masked through the vegetation mask from Landsat data which are then displayed on the Map in the Google Earth Engine. Here, the point that is given as input is displayed as a blue cross and one could scroll through the map to search for urban areas and check the damage detection results. The map can optionally be exported as a KML file through the Tasks tab by pressing Run. As an indication: the processing of the algorithm for Syria took around 14 seconds, the loading of the resulting damage detection map around 1 minute and 5 seconds and the exporting of the map to the Google Drive 40 seconds. These time indications are for a case where 152 ascending and 149 descending Sentinel-1 GRD images and 806 Landsat 8 images have been processed.

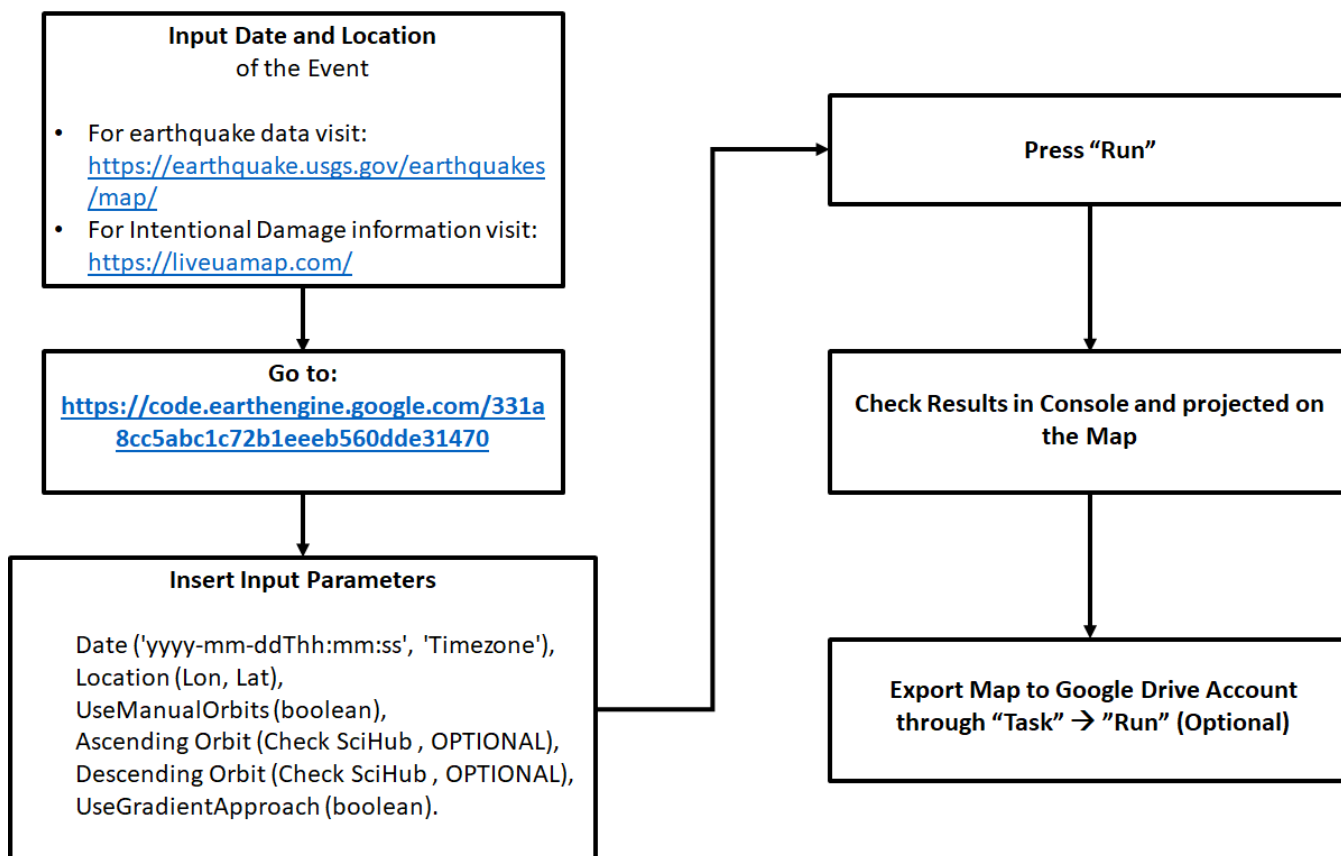


Figure B.1: Overview of the steps the user needs to take to successfully run the damage detection algorithm in case of a disaster.

Interpretation

The damage detection map should be interpreted as a change detection map that indicates locations of possible damaged or collapsed buildings in urban areas after a disaster. The heavier the building is damaged, the higher the backscattering signal is expected to be affected and, assuming that this effect is more severe than what the backscattering signal of this pixel has experienced in the pre-disaster timeseries, the more reddish the colour of the detected pixel will be. Note that due to the viewing geometry of the satellite system with respect to the geometry of the building that is observed, the change in the backscattering intensity might be more or less heavily affected due to changes in the reflecting properties as a result of building damage. Also, false positives may arise due to changes in the surface properties not related to the earthquake that affect the backscattering intensity in such a way the pixel also is detected as changed. Keeping this in mind, this damage detection map can then be put to use in the estimation of the size of the disaster, the division of the area in sectors and the prioritization of these sectors in terms of amount of potential damaged buildings and thus potential casualties. In order to quickly determine the significance of detected pixels, one could also create a reference map of the same area using the date of the pre-disaster image, as done in section 3.4.2. The damaged due to the disaster can be visualized by comparing the reference map to the damage detection map.

C

JavaScript Code

This appendix holds the general JavaScript code used for the damage detection algorithm operated through the Google Earth Engine.

C.1. Damage_General

```
1 var Foo = require('users/jeroenvheyningen/default:Damage/Damage_Function');
2
3 // Entries: Date ('yyyy-mm-ddThh:mm:ss', 'Timezone'),
4 //           Location (Lon, Lat),
5 //           UseManualOrbits (boolean), Ascending Orbit (Check SciHub),
6 //           Descending Orbit (Check SciHub).
7
8 var Date = ee.Date('2018-09-28T10:02:43', 'UTC');
9 var Point = ee.Geometry.Point(117.30, -0.2);
10 var UseManualOrbits = false;
11 var AscendingOrbit = '';
12 var DescendingOrbit = '';
13
14 // Insert Parameters
15 Foo.function(Date,
16             Point, //Lon Lat
17             UseManualOrbits,
18             AscendingOrbit,
19             DescendingOrbit)
```

C.2. Damage_Function

```
1 exports.function = function(EQ, Point, UseManualOrbitNum, orbitnumAsc, orbitnumDsc) {
2
3   //// SET OF PARAMETERS AND FUNCTIONS ////
4   // Import Datasets
5   var Sentinel1 = ee.ImageCollection("COPERNICUS/S1_GRD_FLOAT");
6   var Landsatnew = ee.ImageCollection("LANDSAT/LC08/C01/T1_SR");
7
8   // Center the map on the image and display.
9   Map.centerObject(Point, 15);
10
11  // Standard date variables
12  var Start = ee.Date('2015-01-01'); // Start of S-1 mission
13  var Now = ee.Date('9999', 'UTC'); // Include most recent imagery
14  //var Now = ee.Date('2016-11-01'); // Shorten timeseries in casestudy
15
16  // Create AOI
17  var Polygon = Point.buffer(150000).bounds();
18  print('Polygon: ', Polygon);
19  Map.addLayer(ee.FeatureCollection(Point).style("blue", 5, 'x'), {}, 'Point');
20  Map.addLayer(Polygon, {palette: ['00FFFF']}, 'Polygon', false);
21}
```

```

22 // Add date property to each image
23 var addWantedBands = function(image) {
24   var date = ee.Date(image.get('system:time_end'))
25   var dateString = date.format('yyyy-MM-dd')
26   return image.set('date',dateString)
27 };
28
29 // define function to convert from dB to power and vice versa
30 function toPow(image) {
31   var pow = ee.Image(10.0).pow(image.select(0).divide(10.0))
32   return image.addBands(pow.select(0))}
33 function todB(image) {
34   var dB = ee.Image(image.select(0)).log10().multiply(10.0)
35   return image.addBands(dB.select(0))}
36 function toAmp(image) {
37   var amp = image.select(0).sqrt()
38   return image.addBands(amp.select(0))}
39 function Rename(image) {return image.rename('Int', 'dB', 'Amp')}}
40
41 // Mask out SHADOW, SNOW, and CLOUD classes (from GEE summit)
42 function applyMask(image) {
43   return image.updateMask(image.select('pixel_qa').lt(4))}
44 // a function to calculate NDVI and set a new 'date' property
45 function add_ndvi(image) {
46   var ndvi = image.normalizedDifference(['B5', 'B4']).rename('NDVI');
47   return ndvi.clip(Polygon)
48 }
49 function add_ndwi(image) {
50   var ndwi = image.normalizedDifference(['B3', 'B5']).rename('NDWI');
51   return ndwi.clip(Polygon)
52 }
53
54 // This function mosaics images by time.
55 // According to: https://code.earthengine.google.com/81eceec12b65648aaa28177a6bc177ff
56 function mosaicByTime(images) {
57   var newImages = images.map(function(img){
58     var date_field = ee.Date(img.get('system:time_start')).format("YYYYMMdd");
59     return img.set({'date_field':date_field});
60   });
61   var distinct = ee.ImageCollection(newImages.distinct(['date_field']))
62   var filter = ee.Filter.equals({leftField: 'date_field', rightField: 'date_field'});
63   var join = ee.Join.saveAll('to_mosaic')
64   var results = ee.ImageCollection(join.apply(distinct, newImages, filter))
65   // mosaic
66   var results = results.map(function(i) {
67     var mosaic = ee.ImageCollection.fromImages(i.get('to_mosaic')).sort('system:index')
68       .mosaic()
69     return mosaic.copyProperties(i,['system:time_start', 'orbitNumber_start', '
70       orbitProperties_pass', 'relativeOrbitNumber_start', '
71       transmitterReceiverPolarisation']);
72   })
73   return ee.ImageCollection(results)
74 }
75
76 // LANDSAT8 PROCESSING
77 var ic = Landsatnew
78   .filterDate(Start, Now)
79   .filterBounds(Polygon)
80   .sort('system:time_start', false);
81   //.map(applyMask);
82
83 // Define visualization parameters in an object literal.
84 var VizPar_LS = {bands: ['B4', 'B3', 'B2'], min: -17, max: 1005};
85 print('Landsat collection: ', ic);
86 //Map.addLayer(bands.features(0), vizParams, 'Landsat 8 false color');
87 var Final_LS = ee.Image(ic.mosaic().clip(Polygon));
88 //print('Landsat Final: ', Final_LS); Map.addLayer(Final_LS, VizPar_LS, 'LANDSAT RYB',
89   false);
90 // Calculate NDVI

```

```

89 var ndvi = ic.map(add_ndvi).max();
90 //print('NDVI: ', ndvi);
91 Map.addLayer(ndvi, {min: -1, max: 1}, 'NDVI', false);
92 var NonVegetated = ndvi.lt(0.9);
93 Map.addLayer(NonVegetated, {}, 'NonVegetated', false);
94 // Calculate NDWI
95 var ndwi = ic.map(add_ndwi).median();
96 //print('NDWI: ', ndwi);
97 Map.addLayer(ndwi, {min: -1, max: 1}, 'NDWI', false);
98 var NoWater = ndwi.lt(0.5);
99 Map.addLayer(NoWater, {}, 'NoWater', false);
100
101 //// SENTINEL1 PROCESSING ////
102 // Filter by metadata properties.
103 var vv = Sentinel1
104 // Filter to get images with VV and VH dual polarization.
105 .filter(ee.Filter.listContains('transmitterReceiverPolarisation', 'VV'))
106 .select('VV')
107 // Filter to get images collected in interferometric wide swath mode.
108 .filter(ee.Filter.eq('instrumentMode', 'IW'))
109 // Select only high quality images
110 .filter(ee.Filter.eq('resolution', 'H'))
111 // Filter to extract the correct area
112 .filterBounds(Polygon)
113 // Filter to extract the correct period
114 .filterDate(Start, Now)
115 // Filter to extract the correct period
116 .sort('system:time_start');
117 print("Complete S-1 timeseries :", vv);
118
119 var tempAsc = vv.filterBounds(Point).filterMetadata('orbitProperties_pass', 'equals', '
ASCENDING').sort('system:time_start', false);
120 var tempDsc = vv.filterBounds(Point).filterMetadata('orbitProperties_pass', 'equals', '
DESCENDING').sort('system:time_start', false);
121 print("Temporary Ascending timeseries: ", tempAsc); print("Temporary Descending
timeseries: ", tempDsc)
122
123 if (ee.Algorithms.IsEqual(ee.Number(tempAsc.size()), ee.Number(0)).getInfo() === false)
124 {
125   if (ee.Algorithms.IsEqual(ee.Number(tempAsc.filterDate(EQ, Now).size()), ee.Number(0)).
getInfo() ) {
126     var tempOrbList = ee.List([]);
127     var tempDateList = ee.List([Now]);
128     var nextOrbAsc;
129     var NoAsc = true;
130     while (nextOrbAsc === undefined) {
131       tempAsc = tempAsc.filterDate(Start, (tempDateList.get(-1)))
132       var tempDate = ee.Date(ee.Image(tempAsc.first()).get('system:time_start')).
advance(-5, 'minute');
133       var tempOrb = ee.Image(tempAsc.first()).get('relativeOrbitNumber_start');
134       if (tempOrbList.contains(tempOrb).getInfo() ){
135         nextOrbAsc = tempOrbList.slice(0,2).get(-1);
136         tempAsc = tempAsc.filterMetadata('relativeOrbitNumber_start', 'equals',
nextOrbAsc);
137         var tempDateDiff = ee.Date(tempDateList.slice(1,3).get(-1)).advance(5, 'minute'
).difference(ee.Date(ee.Image(tempAsc.first()).get('system:time_start')), '
second')
138         var nextDateAsc = ee.Date(tempDateList.slice(1,3).get(-1)).advance(5, 'minute')
.advance(tempDateDiff.abs(), 'second')
139       }
140       tempDateList = ee.List(tempDateList.add(tempDate)); tempOrbList = ee.List(
tempOrbList.add(tempOrb));
141     } else { var NoAsc = false }
142 } else { var NoAsc = true }
143
144 if (ee.Algorithms.IsEqual(ee.Number(tempDsc.size()), ee.Number(0)).getInfo() === false)
145 {
146   if (ee.Algorithms.IsEqual(ee.Number(tempDsc.filterDate(EQ, Now).size()), ee.Number(0)).
getInfo() ) {
147     var tempOrbList = ee.List([]);

```

```

147     var tempDateList = ee.List([Now]);
148     var nextOrbDsc;
149     var NoDsc = true;
150     while (nextOrbDsc === undefined) {
151         tempDsc = tempDsc.filterDate(Start, (tempDateList.get(-1)))
152         var tempDate = ee.Date(ee.Image(tempDsc.first()).get('system:time_start')).
            advance(-5, 'minute');
153         var tempOrb = ee.Image(tempDsc.first()).get('relativeOrbitNumber_start');
154         if (tempOrbList.contains(tempOrb).getInfo() ){
155             nextOrbDsc = tempOrbList.slice(0,2).get(-1);
156             tempDsc = tempDsc.filterMetadata('relativeOrbitNumber_start', 'equals',
                nextOrbDsc);
157             var tempDateDiff = ee.Date(tempDateList.slice(1,3).get(-1)).advance(5, 'minute')
                .difference(ee.Date(ee.Image(tempDsc.first()).get('system:time_start')), '
                second')
158             var nextDateDsc = ee.Date(tempDateList.slice(1,3).get(-1)).advance(5, 'minute')
                .advance(tempDateDiff.abs(), 'second')
159         }
160         tempDateList = tempDateList.add(tempDate); tempOrbList = tempOrbList.add(tempOrb)
            ;
161     }
162     } else { var NoDsc = false }
163 } else { var NoDsc = true }
164
165 if (NoAsc && NoDsc) {
166     print('No New Acquisition for both Ascending and Descending Orbits');
167     print('Next Ascending Acquisition over this area: ', nextDateAsc);
168     print("For Ascending Relative Orbit Number: ", nextOrbAsc);
169     print('Next Descending Acquisition over this area: ', nextDateDsc);
170     print("For Descending Relative Orbit Number: ", nextOrbDsc);
171     throw new Error('No Post-Disaster Acquisition');
172 } else if (NoAsc === false && NoDsc) {
173     print('No New Acquisition for Descending Orbits');
174     print('Next Descending Acquisition over this area: ', nextDateDsc);
175     print("For Descending Relative Orbit Number: ", nextOrbDsc);
176     print('Damage Detection algorithm continues...')
177     print('NOTE: RESULTS MAY BE LESS RELIABLE')
178     var onlyAsc = true
179     print("Asc", onlyAsc)
180 } else if (NoAsc && NoDsc === false) {
181     print('No New Acquisition for Ascending Orbits');
182     print('Next Ascending Acquisition over this area: ', nextDateAsc);
183     print("For Ascending Relative Orbit Number: ", nextOrbAsc);
184     print('Damage Detection algorithm continues...')
185     print('NOTE: RESULTS MAY BE LESS RELIABLE')
186     var onlyDsc = true
187     print("Dsc", onlyDsc)
188 } else {
189     var BothOK = true
190     print("Both", BothOK)
191 }
192
193 if (onlyAsc || BothOK) {
194
195     // Process Ascending Images
196     var vvA = vv.filter(ee.Filter.eq('orbitProperties_pass', 'ASCENDING'))
197         .map(todB)
198         .map(toAmp)
199         .map(Rename);
200     // Extract Relative Orbit Number
201     if (UseManualOrbitNum === false) {
202         var orbitnumAsc = ee.Image(vvA.filterBounds(Point).filterDate(EQ, Now).first()).get
            ('relativeOrbitNumber_start');
203     }
204     vvA = mosaicByTime(vvA.filter(ee.Filter.eq('relativeOrbitNumber_start', orbitnumAsc))
        );
205     print("Ascending S-1 timeseries: ", vvA); Map.addLayer(vvA.select("dB"), {min:-30,
        max:5}, 'Ascending', false);
206
207     // Split Timeseries in Pre- and Post-Disaster
208     var beforeA = vvA.filterDate(Start, EQ).map(function(image) {

```

```

209     return image.clip(Polygon).updateMask(NoWater).updateMask(image.select("dB").gt
210       (-24.93)));
211   var preEQA = ee.Image(beforeA.sort('system:time_start', false).first());
212   var afterA = ee.Image(vvA.filterDate(EQ, Now).first()).clip(Polygon).updateMask(
213     NoWater)
214     .updateMask(ee.Image(vvA.filterDate(EQ, Now).first()).select("dB").gt(-24.93));
215   print('pre-disaster timeseries asc:', beforeA); print('pre-disaster image asc:',
216     preEQA);
217   print('post-disaster image asc:', afterA);
218
219   //// Gradient ////
220   var beforeA_list = beforeA.toList(beforeA.size());
221
222   // Threshold radar intensities to identify "damaged" areas.
223   var refA = beforeA_list.slice(0,-1).zip(beforeA_list.slice(1)).map(function(f) {
224     return ee.Image(ee.List(f).get(0)).subtract(ee.Image(ee.List(f).get(1)));
225   });
226   Map.addLayer(ee.ImageCollection.fromImages(refA).select("Int"), {}, 'refA', false);
227   var refA_mean = ee.ImageCollection.fromImages(refA).mean();
228   Map.addLayer(refA_mean.select("Int"), {}, 'refA mean', false);
229   var refA_max = ee.ImageCollection.fromImages(refA).max();
230   Map.addLayer(refA_max.select("Int"), {}, 'refA max', false);
231   var changeA = afterA.subtract(ee.Image(beforeA_list.get(-1)));
232   Map.addLayer(changeA.select("Int"), {}, 'changeA', false);
233
234   // yellow: FFFF66, orange: FF9900, red: FF0000
235   var ratioA_min = changeA.divide(ee.ImageCollection.fromImages(refA).min());
236   Map.addLayer(ratioA_min.select("Int").updateMask(ratioA_min.select("Int").gt(1.0)), {
237     min:1, max:2, palette: ['FFFF66', 'FF0000']}, 'ratioAmin', false);
238   var ratioA_max = changeA.divide(ee.ImageCollection.fromImages(refA).max());
239   Map.addLayer(ratioA_max.select("Int").updateMask(ratioA_max.select("Int").gt(1.0)), {
240     min:1, max:2, palette: ['FFFF66', 'FF0000']}, 'ratioAmax', false);
241   var DamageA_tot = (ratioA_min.select("Int").max(ratioA_max.select("Int"))).
242     updateMask(changeA.select("dB").abs().gt(1.0));
243   Map.addLayer(DamageA_tot.updateMask(DamageA_tot.gt(1.0)), {min:1, max:2, palette: ['
244     FFFF66', 'FF0000']}, 'changeA_tot', false);
245 }
246
247 if (onlyDsc || BothOK) {
248
249   // Process Descending Images
250   var vvD = vv.filter(ee.Filter.eq('orbitProperties_pass', 'DESCENDING'))
251     .map(todB)
252     .map(toAmp)
253     .map(Rename);
254   // Extract Relative Orbit Number
255   if (UseManualOrbitNum === false) {
256     var orbitnumDsc = ee.Image(vvD.filterBounds(Point).filterDate(EQ, Now).first()).get
257       ('relativeOrbitNumber_start');
258   }
259   vvD = mosaicByTime(vvD.filter(ee.Filter.eq('relativeOrbitNumber_start', orbitnumDsc))
260     );
261   print("Descending S-1 timeseries: ", vvD); Map.addLayer(vvD.select("dB"), {min:-30,
262     max:5}, 'Descending', false);
263
264   // Split Timeseries in Pre- and Post-Disaster
265   var beforeD = vvD.filterDate(Start, EQ).map(function(image) {
266     return image.clip(Polygon).updateMask(NoWater).updateMask(image.select("dB").gt
267       (-24.93)));
268   var preEQD = ee.Image(beforeD.sort('system:time_start', false).first());
269   var afterD = ee.Image(vvD.filterDate(EQ, Now).first()).clip(Polygon).updateMask(
270     NoWater)
271     .updateMask(ee.Image(vvD.filterDate(EQ, Now).first()).select("dB").gt(-24.93));
272   print('pre-disaster timeseries dsc:', beforeD); print('pre-disaster image dsc:',
273     preEQD);
274   print('post-disaster image dsc:', afterD);
275
276   //// Gradient ////
277   var beforeD_list = beforeD.toList(beforeD.size());
278
279   // Threshold radar intensities to identify "damaged" areas.
280   var refD = beforeD_list.slice(0,-1).zip(beforeD_list.slice(1)).map(function(f) {

```

```

267     return ee.Image(ee.List(f).get(0)).subtract(ee.Image(ee.List(f).get(1)));
268 Map.addLayer(ee.ImageCollection.fromImages(refD).select("Int"), {}, 'refD', false);
269 var refD_mean = ee.ImageCollection.fromImages(refD).mean();
270 Map.addLayer(refD_mean.select("Int"), {}, 'refD mean', false);
271 var refD_max = ee.ImageCollection.fromImages(refD).max();
272 Map.addLayer(refD_max.select("Int"), {}, 'refD max', false);
273 var changeD = afterD.subtract(ee.Image(beforeD_list.get(-1)));
274 Map.addLayer(changeD.select("Int"), {}, 'changeD', false);
275
276 // yellow: FFFF66, orange: FF9900, red: FF0000
277 var ratioD_min = changeD.divide(ee.ImageCollection.fromImages(refD).min());
278 Map.addLayer(ratioD_min.select("Int").updateMask(ratioD_min.select("Int").gt(1.0)), {
279   min:1, max:2, palette: ['FFF666', 'FF0000']}, 'ratioDmin', false);
280 var ratioD_max = changeD.divide(ee.ImageCollection.fromImages(refD).max());
281 Map.addLayer(ratioD_max.select("Int").updateMask(ratioD_max.select("Int").gt(1.0)), {
282   min:1, max:2, palette: ['FFF666', 'FF0000']}, 'ratioDmax', false);
283 var DamageD_tot = (ratioD_min.select("Int").max(ratioD_max.select("Int"))).
284   updateMask(changeD.select("dB").abs().gt(1.0));
285 Map.addLayer(DamageD_tot.updateMask(DamageD_tot.gt(1.0)), {min:1, max:2, palette: [
286   'FFF666', 'FF0000']}, 'changeDTot', false);
287
288 }
289
290 if (onlyAsc) {
291   var DamageMap = DamageA_tot;
292   print("ASC");
293 }
294 else if (onlyDsc) {
295   var DamageMap = DamageD_tot;
296   print("DSC");
297 }
298 else if (BothOK) {
299   var DamageMap = DamageA_tot.max(DamageD_tot);
300   print("Both");
301 }
302 print('Damage Total: ', DamageMap);
303 Map.addLayer(DamageMap.updateMask(DamageMap.gt(1.0)), {min:1, max:2, palette: ['FFF666',
304   'FF0000']}, 'RatioMax', false);
305 Map.addLayer(DamageMap.updateMask(DamageMap.gt(1.0)).updateMask(NonVegetated),
306   {min:1, max:2, palette: ['FFF666', 'FF0000']}, 'RatioMaxUrban', true);
307 var FinalMap = DamageMap.updateMask(DamageMap.gt(1.0)).updateMask(NonVegetated);
308
309
310 //// FINALIZATION ////
311
312 Export.image.toDrive({
313   image: FinalMap,
314   description: 'DamgedBuildings',
315   folder: 'GEE',
316   scale: 20
317 });
318 };

```